Measurement of the Hadronic Photon Structure Function F_2^{γ} with the L3 Detector at LEP

by

Liza Gyöngyi Baksay

Master of Science
Physics
Kossuth Lajos University
Debrecen, Hungary
1997

A dissertation
submitted to
Florida Institute of Technology
in fulfillment of the requirements
for the degree of

Doctor of Philosophy
in
Physics

Melbourne, Florida
May 2005

We the undersigned committee hereby recommend that the attached document be accepted as fulfilling in part the requirements for the degree of Doctor of Philosophy in Physics.

"Measurement of the Hadronic Photon Structure Function F_2^{γ} with the L3 Detector at LEP,"
a dissertation by Liza Gyöngyi Baksay.

_____

Marcus Hohlmann, Ph.D.
Assistant Professor, Physics and Space Sciences
Dissertation Advisor

_____

Hector Gutierrez, Ph.D.
Assistant Professor, Mechanical and Aerospace Engineering

_____

Joseph Dwyer, Ph.D.
Associate Professor, Physics and Space Sciences

_____

James G. Mantovani, Ph.D.
Assistant Professor, Physics and Space Sciences

_____

Hamid K. Rassoul, Ph.D.
Professor, Physics and Space Sciences

_____

Gabor David, Ph.D.
Senior Scientist, Brookhaven National Laboratory

_____

Laszlo A. Baksay, Ph.D.
Department Head and Professor, Physics and Space Sciences

Abstract

Title: Measurement of the Hadronic Photon Structure Function F_2^{γ} with the L3 Detector at LEP

Author: Liza Gyöngyi Baksay

Advisor: Marcus Hohlmann, Ph.D.

The photon is one of the basic components of our present understanding of elementary particles and their interactions. The theory of Quantum Electrodynamics describes this object as being the mediator of the electromagnetic force between charged particles. Contrary to earlier assumptions the photon turns out to have a "structure" due to quantum fluctuations into fermion anti-fermion pairs that can further interact with other particles. In this case the photon reveals its structure. The structure of the photon can be described by the concept of photon structure functions, which are studied at high energy accelerators like the Large Electron Positron Collider at the European Center for Particle Physics.

With the large amount of data (L=608 pb^{-1}) collected with the L3 detector at center-of-mass energies 189 GeV < $\sqrt{s}$ < 209 GeV and the analysis method used in this dissertation, a measurement of the hadronic structure function $F_2^{\gamma}(x,Q^2)/\alpha$ is

obtained with better precision than previous measurements. The evolution of F_2^{γ}/α as a function of x and Q^2 is studied in the $11\,\mathrm{GeV}^2 < Q^2 < 34\,\mathrm{GeV}^2$ and $0.006 < x < 0.556$ intervals. Due to the precision of this measurement it is possible for the first time to demonstrate that the results of the higher-order GRV parametrization of the structure function are in good agreement with the data and give a correct description of the physical processes involved.

Table of Contents

List of Figures

List of Tables

Acknowledgement

This research was carried out within the framework of the L3 experiment at CERN, European Center for Particle Physics, in close collaboration with the University of Geneva, Switzerland. The data analysis has been performed at Florida Tech and at CERN.

I would like to thank my advisor Professor Marcus Hohlmann at Florida Tech for his continuous support, advice, and friendship. Special thanks for all the mentoring and help from Professor Maria Kienzle from the University of Geneva. She spent lots of time to advise me on all the details of this work. She encouraged me and always helped me no matter on which continent or in which country she or I were. Both of them helped a lot with their supportive guidance, discussions, and verification of my results. I am a very lucky person that I had them working with me. Thanks for all of their efforts.

A big “thank you” to Salvatore Mele (the L3 physics analysis coordinator, CERN), Professor John Field (University of Geneva), and Chih-Hsun Lin (L3 referee, CERN) for all of their precious time spent to work with me. Many thanks to Professor and Physics Nobel Laureate Samuel C. C. Ting (MIT, CERN) and the L3 publication committee members for reading and approving the result of my work.

Special thanks to my husband and mentor Professor László Baksay who was always there to answer my questions and help with any problems that came up during my graduate years. I would also like to thank my colleague, friend, and office mate Ph.D. student Klaus Dehmelt. Our discussions gave me many good hints and ideas, which helped to improve my analysis results.

I would like to thank the Florida Institute of Technology, the University of Debrecen, Hungary, the University of Alabama, the Institute of Nuclear Research of the Hungarian Academy of Sciences (ATOMKI), the European Center for Particle Physics (CERN), the Department of Energy (DOE) and the Hungarian Research Foundation (OTKA) for their support during various phases of my participation in the L3 experiment.

I would also like to mention all my teachers and the dissertation committee members Professors Joe Dwyer, Marcus Hohlmann, Hector Gutierrez, James Mantovani, Hamid Rassoul at Florida Tech and Dr. Gábor Dávid at Brookhaven National Laboratory; my teachers at the Kossuth University, especially Professors István Angeli, István Lovas, and Péter Raics; and my teachers at the Eötvös Lóránd University (Budapest) and University of Oradea (Romania) who advised me all these years and who prepared me to have the proper physics background. With this knowledge I was able to study and understand arising research problems from a broader physics point of view. In this sense they helped me to “grow up” and become a Ph.D. graduate in Physics.

In memory of Academician Professor Dezső Kiss who put me on the path of particle physics.

A very special thanks goes to my parents and my husband. Without their support, patience, understanding, and devoted help and love this dissertation work would not have been possible. Thank you to my children Réka (5 years old) and Csanád (9 years old) who grew up generously sacrificing their “play time” to afford their mother study and research time.

Many thanks to all of you.

Chapter 1

1. INTRODUCTION

1.1. Historical Overview of Photon Related Discoveries

What is light? There were several scientific attempts that tried to give the right answer to this question and we are still not in the position to say that we can put an end to this quest. We already know that light is made of small entities called photons. This overview features some of the historical discoveries regarding this mysterious entity.

The photon is the elementary constituent of light. In Quantum Electrodynamics (QED) it is considered to be the mediator of the electromagnetic force between charged particles. An endless row of similar statements can be made here about the quanta of light but before that we should make a little detour back in time. Even before the beginning of the 19th century there have been a series of attempts to reveal the real nature of light. Several decades passed with empirical and experimental observations based on well-established theory (mechanics, wave theory, theory of light). However, these observations were not very well understood

and new and challenging ideas were necessary to move this field of physics ahead. Some of the most exciting questions that preoccupied those early years quantum scientists are the same also today: What is light? What is it made of? How can we interpret it? Is it a wave or a corpuscle? In order to answer these questions there were several experimental and theoretical attempts to prove the two different aspects of the photon.

Issac Newton's well-established corpuscular theory of light dominated till the 19th century. Newton, assuming that light is made of tiny particles, could explain the reflective and refractive properties of light. However, he could not account for the interference effects, that were known to be a property of waves.

Although Newton's theory was highly accepted, there were others who were in favor of wave theory. Back in 1660 Francesco Grimaldi's experiment showed that light can bend around obstacles (diffraction). He concluded that light is like a fluid that exhibits wave-like motion. A few years later in 1678 Christian Huygens, based on Robert Hook's general idea (1664), deduced the laws of reflection and refraction. He believed that light is caused by the pulsation of a light source. This travels through "ether" with a periodic up and down motion perpendicular to the direction of propagation. Despite these experiments the wave theory of light was abandoned for several years. More than one century passed till in 1801 Thomas Young in his simple interference experiment confirmed again that light acts as a wave. If a screen was placed at the point were two wave fronts

overlapped, darker and lighter areas could be observed showing the phenomenon of interference. James Clerk Maxwell, the father of wave theory, in 1865 showed that the speed of an electromagnetic wave should be the same as the speed of light. Based on this result he concluded that light is a form of electromagnetic wave that travels through space. Between 1808 and 1875 there were several others like Louis Malus, Jean Arago, Jean Fresnel, Leon Foucault, Louis Fizeau, Marie Alfred Cornu who established through many experiments that light is a transverse wave. Several of these scientists including later Michelson and Morley made accurate measurements of the velocity of light in various media. All these experiments described and explained the light as an electromagnetic wave, but could not account for its particle nature.

In 1900 Max Planck determined the black body spectrum for the electromagnetic radiation emitted by a hot object. Classical physics predicted that the intensity of emitted light should increase rapidly and without limit with decreasing wavelength. Plank could "escape" this ultraviolet catastrophe only if he considered that the body consists of vibrating oscillators that could absorb and emit small quantized packets of energy $E= h\nu$ (ν frequency of the radiation, h constant fitted to the data). In 1905 Albert Einstein formulated the theory of light quanta. Based on this theory he could explain the "photoelectric effect", a process where electrons are ejected from a metallic surface due to an incident electromagnetic radiation. Einstein showed that the electron's maximum energy does not depend on

the intensity of the incident beam of light but only on the frequency (or wavelength). This was in total contradiction with the wave theory that considers that the energy of the electron increases with the intensity of the light source. Einstein concluded that light consists of discrete quantized packets of energy that also have a wave nature being characterized by a wavelength. There were also other attempts that tried to show that the photon is not a wave but a particle. In 1916 Robert Millikan found that his measurements were predicted by Einstein's photoelectric equation. Millikan determined with high accuracy that the maximum kinetic energy of the ejected electrons obeys Einstein's equation. He determined Planck's constant with a remarkable precision proving the correctness of the photon concept.

In 1922 Arthur Holly Compton seemed to finally settle this debate about the nature of light. In his experiment he showed that when light interacts with electrons it behaves as if composed of particles with energy $h\nu$ (h Planck's constant, ν frequency of radiation) and momentum $h\nu/c=h/\lambda$ (c speed of light, λ wavelength). He found that the wavelength of the scattered photon λ is slightly shifted compared to the incident photon's wavelength λ_0. He concluded that the wavelength of x-rays scattered on free electrons at a given angle does not depend on the intensity of the radiation and length of exposure, but only on the scattering angle θ:

$$\lambda - \lambda_0 = \frac{h}{m_e c}(1 - \cos\theta), \qquad (1.1)$$

where m_e is the mass of the recoiling electron and $h/m_e c$ is the "Compton wavelength".

This long row of innovative experiments finally lead to the conclusion that light is simultaneously "wave" and "particle". This dual nature of the photon is successfully described by Quantum Electrodynamics. In this theory both "particle" and "wave" properties of the photon are inevitable and complementary.

1.2. Description of Basic Photon Interactions

1.2.1. QED Interactions

Particle interactions are described in the context of Quantum Field Theory. In this theory particle physics is formulated in terms of the Lagrangian $\mathcal{L}$. The potential energy terms, also called interaction Lagrangian, specify the forces, while the kinetic energy terms are general and depend only on the spins of the particles.

The laws of physics are universal. They have to be the same everywhere. Making the Lagrangian invariant under Lorentz transformations provides a Lorentz invariant theory. Local gauge invariance of the theory means that we can chose any phase of the field at each space-time point without affecting the theory.

Local gauge invariance U(1) of the theory for electrically charged particles (Dirac fermions) requires that there must be a field quantum, an integer-spin gauge boson, which is the mediator of the electromagnetic interaction. The associated fields are called gauge fields and the gauge theory is called Quantum Electrodynamics.

In QED the photon is the mediator particle and can couple only to charged fermions that can be quarks or leptons. The property "charge" is attributed to a particle if it couples to the photon. Conventionally, there are two types of electric charges: positive and negative. The value of the charge is proportional to the strength of the coupling between the interacting particles. The force is attractive if the charges are of the same type and repulsive if they are of different type.

In QED the free photon is considered a structureless and zero rest mass entity. Particles that take part in a virtual processes are said to be "off mass-shell", receiving a non-physical mass. It means that the relation $E^2 = p^2c^2 + m_0^2c^4$ does not hold for them. Due the Heisenberg Uncertainty Principle a virtual photon can be emitted for a very short time $\Delta t \leq (\hbar / \Delta E)$ and will be reabsorbed. The continuous release and absorption of virtual photons by fermions leads to the formation of so-called virtual photon clouds around them (Figure 1.1). In case of fermion pair production the virtual photon can violate conservation of energy by an amount of energy ΔE (can borrow this energy from the emitting charged particle) for a very short period of time Δt, can fluctuate into a charged fermion anti-fermion pair

$\gamma^* \rightarrow f\bar{f}$ and then go back again into a photon $f\bar{f} \rightarrow \gamma$. This is called vacuum polarization (Figure 1.2). Virtual photons can also create virtual fermion pairs (Figure 1.3) or the virtual photon can interact with another photon (Figure 1.4). The last process is studied in the framework of two-photon physics and is the subject of this dissertation.

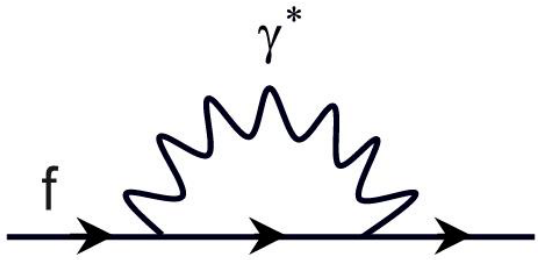

Figure 1.1 Charged fermion emitting and reabsorbing a virtual photon.

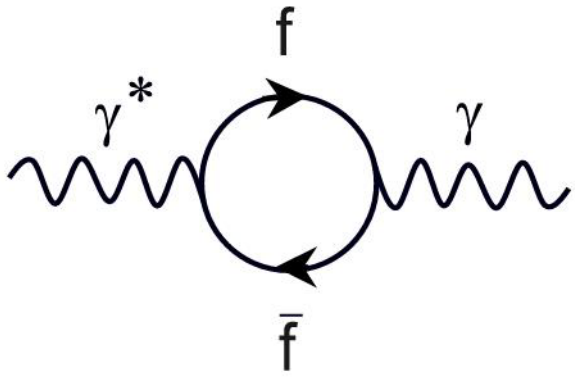

Figure 1.2 Virtual photon fluctuating into an $f\bar{f}$ pair and back into a photon.

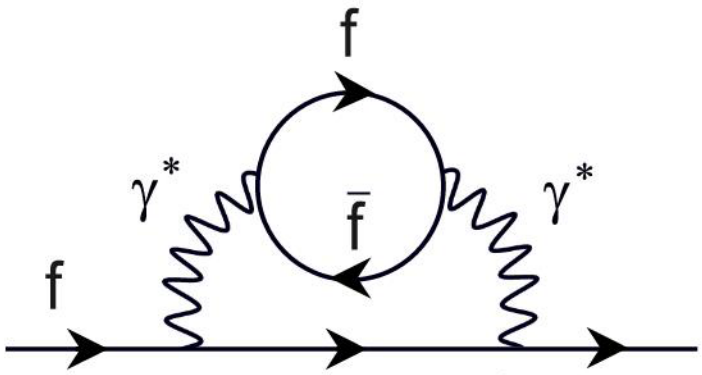

Figure 1.3 Creation of a virtual $f\bar{f}$ pair.

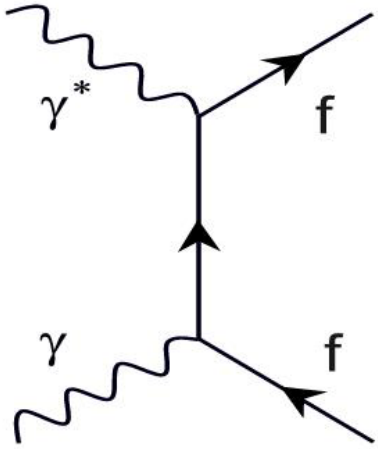

Figure 1.4 Simplest two-photon interaction.

In reality these processes are interconnected (Figure 1.5). Due to the virtual particle emissions and absorptions a cloud of charges will surround the negative test charge as shown in (Figure 1.6). After getting closer to the negative charge, a probing charge penetrates the cloud of virtual e^+e^- pairs leading to an increase in

the effective interaction between them. The negative charge will appear “less screened” and a larger charge will be measured. Consequently, the described effect is called charge screening.

The electromagnetic coupling constant α is a measure of the strength of the electromagnetic interaction. Contrary to its name, its value is not a constant. This can increase with the energy of the interaction. In the low energy limit (Figure 1.7), when we have a low energy probe, it becomes the familiar fine structure constant with the value $\alpha \cong 1/137$. For experimentally accessible energies α is weak enough to permit perturbative QED calculations.

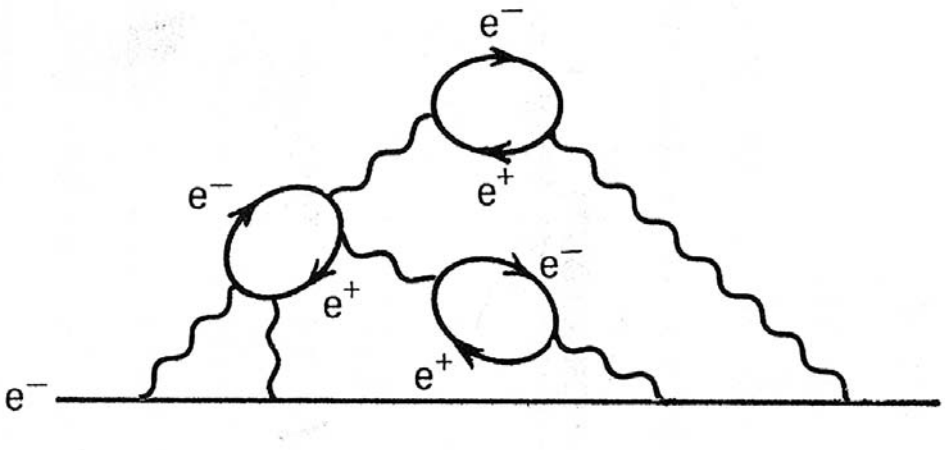

Figure 1.5 A QED interaction [1].

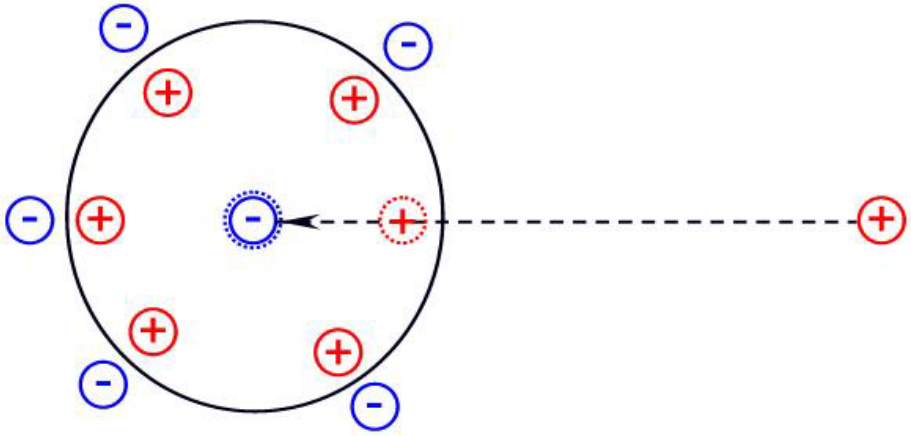

Figure 1.6 Screening of the electric charge.

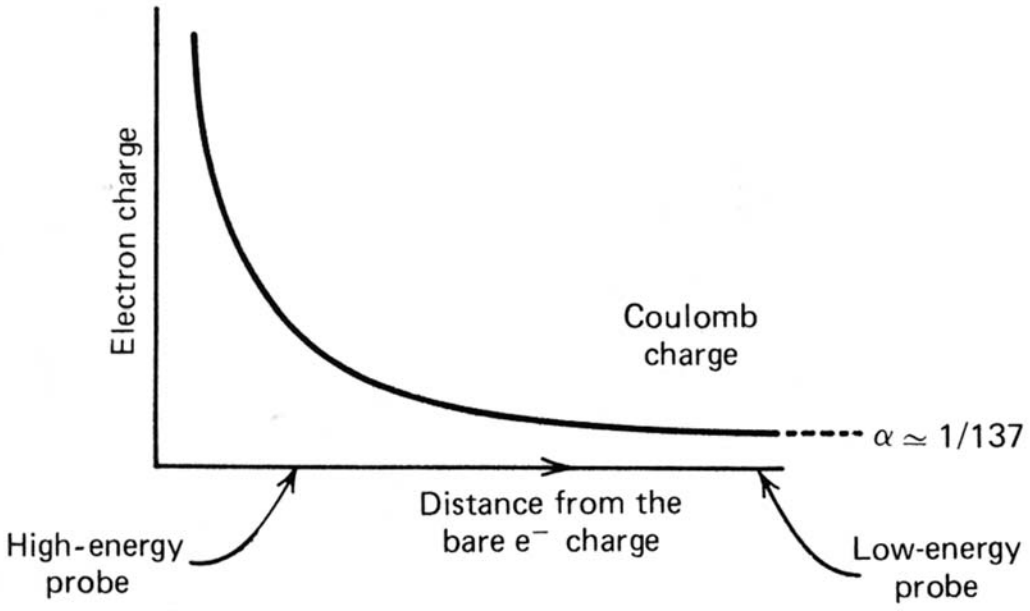

Figure 1.7 Evolution of the electromagnetic coupling constant α [1].

For scattering of an electron by a static charge one can write the physically measured charge as

$$e^2(Q^2) = e_0^2\left(\frac{1}{1+I(q^2)}\right), \tag{1.2}$$

where e_0^2 is the real charge, also called "bare charge", of the target particle. $I(q^2)$ is the perturbatively calculable photon propagator that has contributions from logarithmically divergent and finite terms. The charge that experimentalists measure depends on the particular value of the virtual photon's momentum q, specifically on the momentum squared, q^2, which is negative for virtual particles. It is conventional to use $-q^2 = Q^2$, which is called the "virtuality" of the virtual photon. In the large Q^2 limit

$$I(q^2) = \frac{\alpha}{3\pi}\log\left(\frac{M^2}{-q^2}\right), \tag{1.3}$$

where M^2 has been introduced as a cut-off for the infinite part of $I(q^2)$ that appears when $M^2 \to \infty$. From here on units are used according to the Appendix. Therefore, M and q are both parameters with dimension of momentum expressed in GeV. The "running coupling constant" is given as

$$\alpha(Q^2) \equiv e^2(Q^2)/4\pi\,. \tag{1.4}$$

Replacing $I(q^2)$ in equation (1.2) and $e^2(q^2)$ in (1.4) $\alpha(Q^2)$ becomes

$$\alpha(Q^2) = \frac{\alpha_0}{1 - \frac{\alpha_0}{3\pi}\log\left(\frac{Q^2}{M^2}\right)}. \tag{1.5}$$

To have only finite and physically measurable quantities, the arbitrary cut-off value has to vanish from equation (1.5). One can choose a renormalization or reference momentum μ. After subtracting $\alpha(\mu^2)$ from $\alpha(Q^2)$ we find

$$\alpha(Q^2) = \frac{\alpha(\mu^2)}{1 - \frac{\alpha(\mu^2)}{3\pi}\log\left(\frac{Q^2}{\mu^2}\right)}. \tag{1.6}$$

This result shows that with increasing Q^2 the photon sees more and more charge. α increases slowly from the value of 1/137 until it becomes infinite at a very large finite value of Q^2.

1.2.2. QCD Interactions

Quarks can also interact by photon exchange. However, this interaction is not strong enough to bind quarks into hadrons. A much stronger force is needed, mediated by a gauge boson. This force is called the fundamental strong force.

Again we can formulate a theory of "strong" interactions in the context of quantum field theory. Local gauge invariance SU(3) of the theory for "color charged" particles (quarks) requires that there must be a field quantum (integer spin gauge boson) that is the mediator of the strong interaction. The associated fields are called gauge fields and the gauge theory is called Quantum Chromodynamics (QCD).

In QCD the gluon is the mediator particle and "carrier of color" that couples to colored fermions. Gluons are massless integer-spin bosons like the photon. The property color is attributed to each particle that has interaction with gluons. Quarks are known to have six different flavors: u (up), d (down), c (charm), s (strange), t (top), b (bottom) and three primary colors: red, green and blue (RGB). Since all observed particles are colorless or "white", the anti-quarks are assigned the complementary colors: cyan, magenta, yellow ($\overline{R}, \overline{G}, \overline{B}$). There can be many combinations of quarks, and among these are several not yet seen in experiments, like the heavier and less stable combinations of s, c, and b quarks. The top quark has a very short lifetime, so it does not form hadrons before decaying. The most conventional quark combinations are baryons, composed of one red, one green and

one blue quark, and mesons that include a quark and an anti-quark of the corresponding anti-color. All of these combinations must possess an integral amount of electrical charge. We can never detect a single quark or a quark-quark bound state. The existence of these particles is forbidden by the rule of color conservation.

We can formulate an analogy between QCD and QED processes. Instead of photons write gluons and consider that fermions are colored quarks. This way we find that any colored quark can emit and reabsorb a colored gluon (Figure 1.8). A virtual gluon can fluctuate into a virtual quark anti-quark pair trough a vacuum polarization process and then go back into a gluon (Figure 1.9). Since gluons carry "color charge" they can self-interact with each other (Figure 1.10). This is completely opposite to the situation of the electromagnetic field quanta. The photon does not have a charge so it cannot self-couple.

Again, in reality these processes are interconnected (Figure 1.11). A similar effect of charge screening can be observed also in QCD. However, this will be called now color screening and instead of charged electron pairs we will have color charged quark and gluon pairs, as described above. At very small distances quarks behave as free non-interacting particles. As we try to separate quarks of the same color the force that binds them together becomes stronger. The quark confinement is explained since the strength of the strong coupling increases with the distance between the colors. At high enough energy, the creation of a new quark anti-quark

pair out of the vacuum becomes energetically more favorable than to allow the quarks to separate further. What we see in the detector are color-neutral particles (mesons and baryons), clustered together in so-called “jets”. The described process is called hadronization or fragmentation: conversion of energy into matter until all quarks are confined into hadrons.

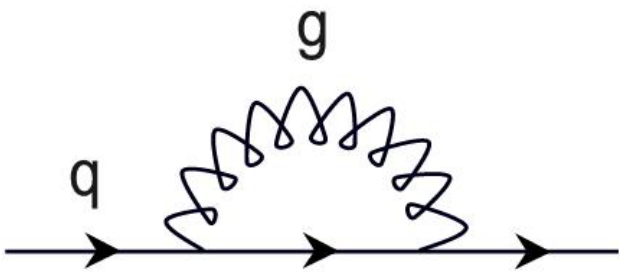

Figure 1.8 Quark emitting and reabsorbing a gluon.

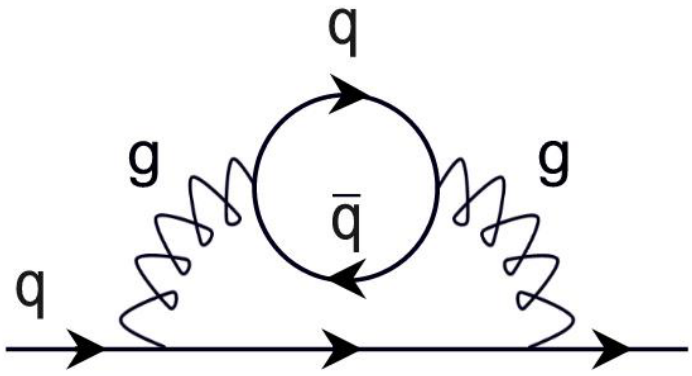

Figure 1.9 Creation of a virtual quark pair from a gluon.

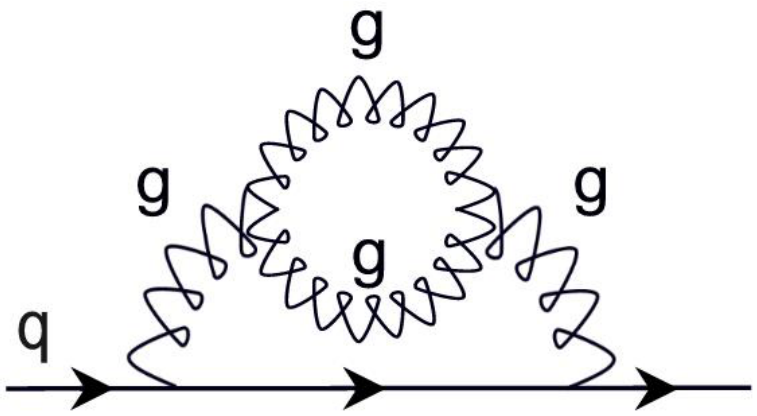

Figure 1.10 Self-coupling of gluons.

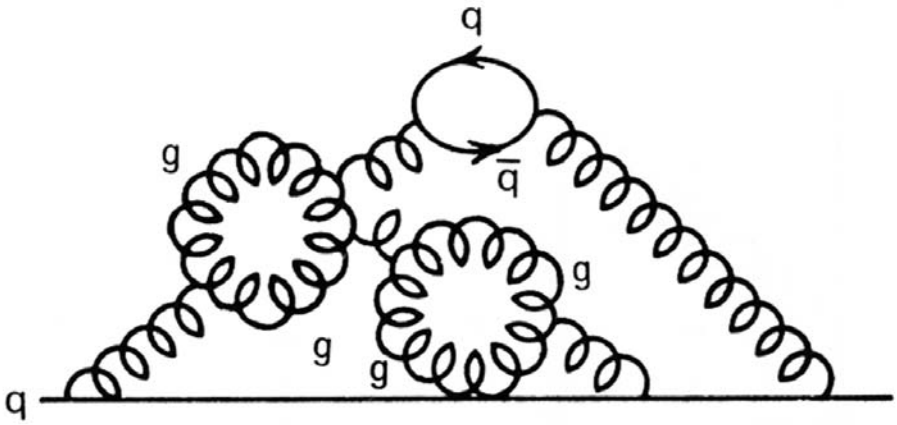

Figure 1.11 A QCD interaction [1].

The QCD behavior of the strong coupling α_s is very different from that of the QED coupling α. It can be shown that the different QCD interaction terms yield [1]

$$\alpha_s(Q^2) = \frac{\alpha_s(\mu^2)}{1 - \frac{\alpha_s(\mu^2)}{12\pi}(33 - 2n_f)\log\left(\frac{Q^2}{\mu^2}\right)}. \tag{1.7}$$

Only for more than 16 quark flavors is the sign of the coefficient in front of $\log(Q^2/\mu^2)$ in equation (1.7) the same as in QED (1.5). Currently we reach energies that prove only the existence of the u, d, c, s, b, and t quarks. From equation (1.7) we can immediately see that $\alpha_s(Q^2)$ decreases with increasing Q^2. For short distance interactions the strong coupling becomes small until quarks behave as free particles (Figure 1.12). For low Q^2 values the strong coupling becomes large. The Q^2 scale where this happens is

$$\Lambda^2 = \mu^2 \exp\left[\frac{-12\pi}{(33 - 2n_f)\alpha_s(\mu^2)}\right]. \tag{1.8}$$

Therefore, the expression (1.7) for α_s becomes:

$$\alpha_s(Q^2) = \frac{12\pi}{(33 - 2n_f)\log\left(\frac{Q^2}{\Lambda^2}\right)}. \tag{1.9}$$

For large Q^2 values ($Q^2 >> \Lambda^2$) the quark masses can be neglected, and they contribute no mass scale Λ to QCD. The effective coupling becomes small and we can use perturbation theory as in QED to describe shortest-distance interactions between quarks and gluons. At $Q^2 \cong \Lambda^2$ the coupling between quarks and gluons becomes strong so they form bound states called hadrons. At this scale, perturbation theory cannot be used anymore. Λ is the value that separates the world of quasi-free quarks and gluons, and their bound hadronic states. The free parameter Λ is not predicted by theory. It has to be determined from experiments.

Using high energy accelerators we can probe the color charge of individual quarks inside different target particles and reach distances where the strong coupling constant is smaller. The aim is to reach energies and distances where α_s is on the order of 0.1 (Figure 1.13) and perturbation theory gives a good approximation. As an example, for the Q^2 range 11-34 GeV^2 of the present analysis, corresponding to an average value of 18.4 GeV^2, the strong coupling is expected to be around the 0.1 value [1].

For center-of-mass energies lower than 2 GeV, α_s becomes too large to permit the use of perturbation theory. In this region perturbative QCD calculations cannot be performed and therefore phenomenological models or simulations are necessary (Section 4.4.3).

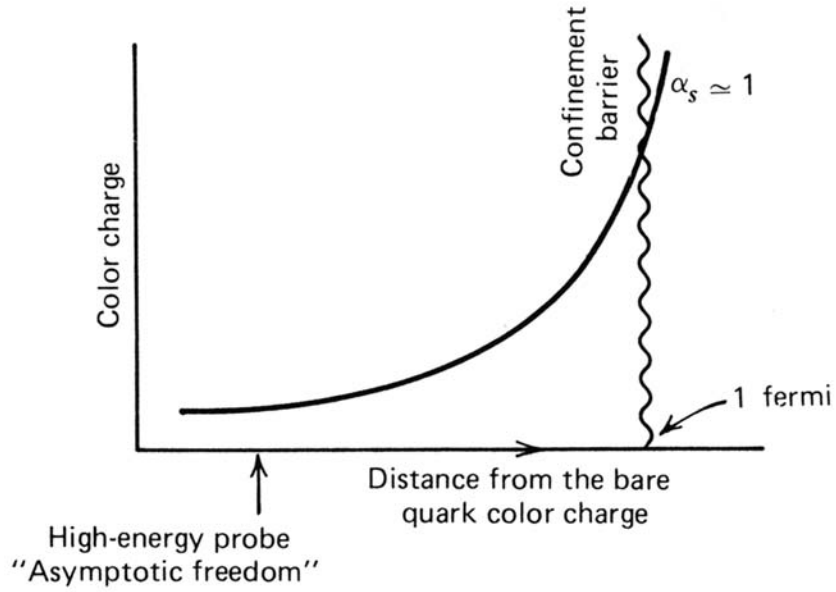

Figure 1.12 Evolution of the strong coupling α_s [1].

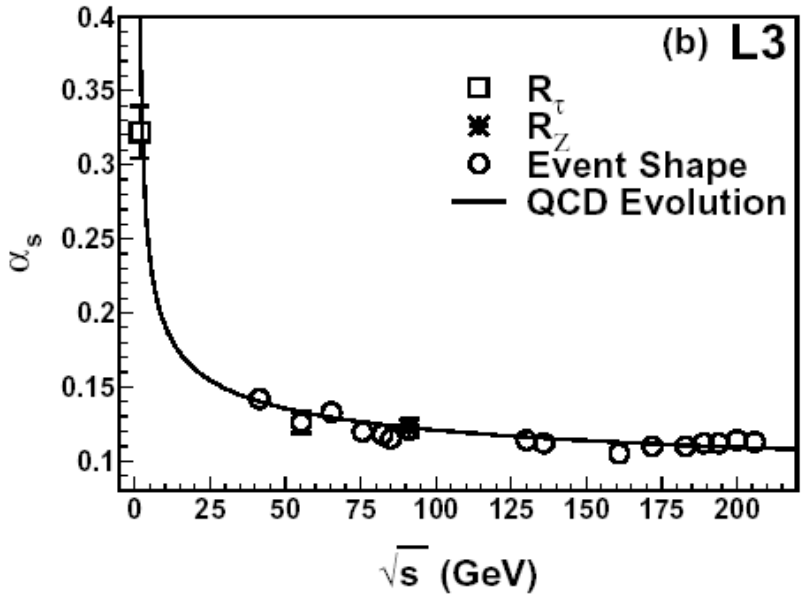

Figure 1.13 Strong coupling constant α_s measured by the L3 experiment [2].

1.3. Classification of two-photon interactions

In the deep inelastic scattering process $e^+e^- \rightarrow e^+e^-\gamma^*\gamma^{(*)} \rightarrow e^+e^-X$ (Figure 1.14) the highly virtual photon γ^*, with high four-momentum transfer q, emitted by the scattered electron is testing the structure of the quasi-real photon $\gamma^{(*)}$. The result of this interaction is in leading order a fermion pair $X=f\bar{f}$, where f can be either lepton or quark. In case of lepton pair production ($\gamma \rightarrow l^+l^-$) the process can be precisely calculated in QED since there are no self-couplings of the photon. However, in case of quark pair production ($\gamma^{(*)} \rightarrow q\bar{q}$ pair), QCD corrections have to be taken into account due to the additional QCD interaction terms.

Depending on what we want to measure, two-photon physics studies can be subdivided as follows:

- The total hadronic cross section can be measured at low photon virtualities.
- Single-tagged hadron production allows study of the photon structure function.
- Double-tagged hadron production allows study of the virtual photon structure.
- Charm and beauty production reveal the heavy flavor content of the photon.
- Jet and single (inclusive) particle production is used for studying QCD processes over a wide transverse momentum p_t range.

- Study of exclusive resonance production gives the opportunity to study the quark content of mesons using the special features of two-photon coupling.

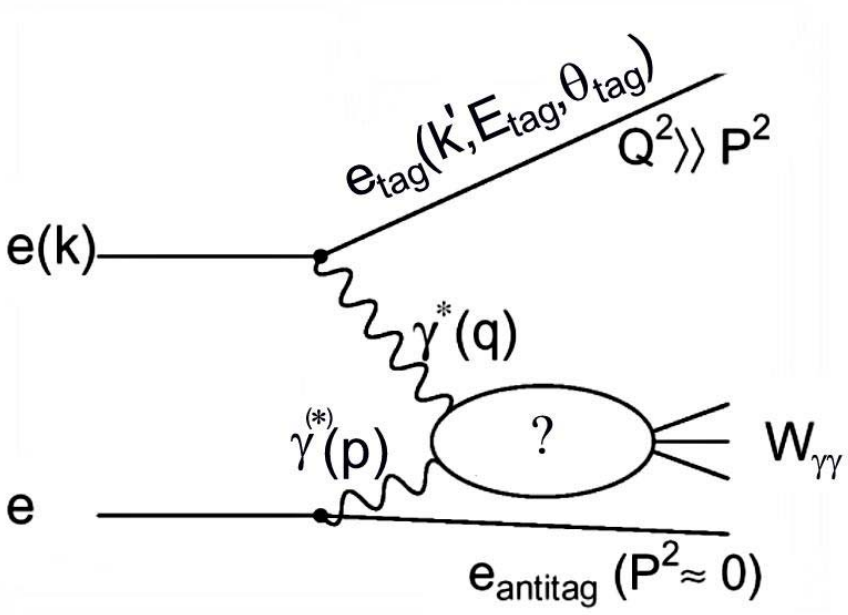

Figure 1.14 A virtual photon γ^* testing the structure of a quasi-real photon $\gamma^{(*)}$.

Chapter 2

2. THE LEP COLLIDER AND THE L3 EXPERIMENT

2.1. The LEP collider

The Large Electron-Positron Collider (LEP) was located at the European Center for Particle Physics near the border between France and Switzerland. In LEP beams of electrons and positrons orbited in opposite directions in a 27 km circumference vacuum pipe, 70 m under the surface. The beams, traveling near the speed of light, were guided by magnets to four collision points, where the four LEP experiments L3, ALEPH, DELPHI, and OPAL were placed.

The LEP collider was designed to perform high precision tests and measurements of the standard model, especially weak interactions and to search for unexpected physics in a new energy range. During its operation between 1989 and 2000, the accelerator reached energies high enough to produce the Z (m = 91 GeV) and pairs of W (m = 80 GeV) particles, carriers of the weak force. The accelerator was shut down in the year 2000 after having reached a highest center-of-mass energy of 209 GeV.

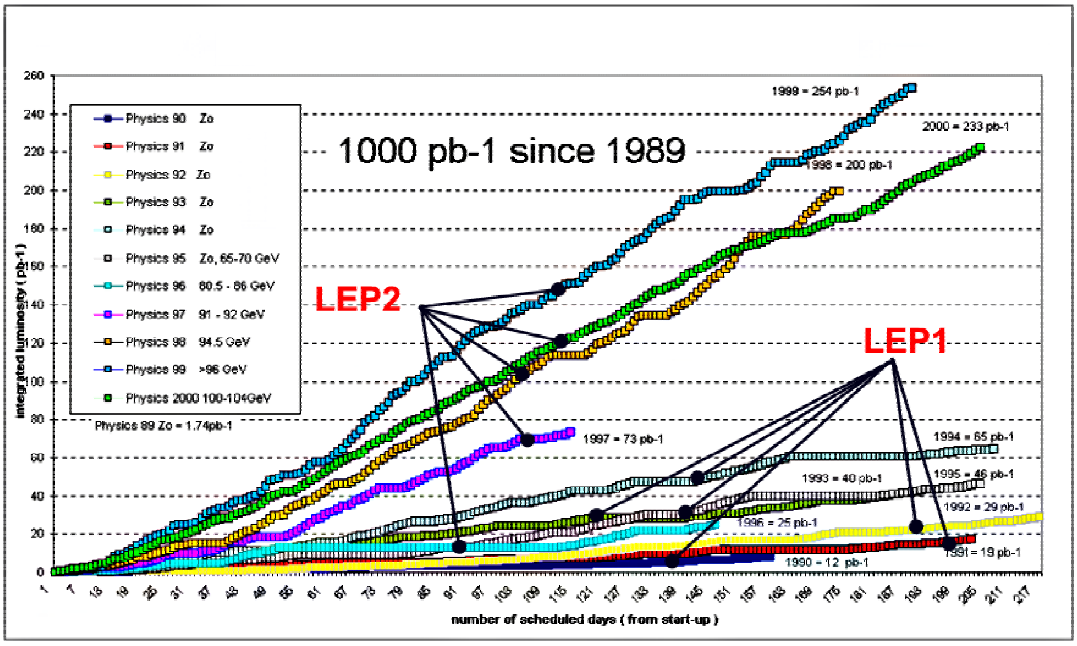

Figure 2.1 Integrated luminosities seen by the four LEP experiments from 1989 to 2000 [3].

Luminosities delivered by LEP at different energies corresponding to the two LEP phases LEP1(1989-1995, $88\,\text{GeV} < \sqrt{s} < 94\,\text{GeV}$) and LEP2(1996-2000, $161\,\text{GeV} < \sqrt{s} < 209\,\text{GeV}$) are shown in Figure 2.1. The luminosity is calculated using the relation

$$L = \frac{I_b^2 N_b f_0}{4\pi\sigma_x\sigma_y}, \tag{2.1}$$

where σ_x and σ_y are the horizontal and vertical beam sizes, I_b is the intensity per bunch, N_b is the number of bunches per beam, and f_0 is the revolution frequency.

The LEP performance was well above the design expectations. During the last year of data taking, a signal consistent with Standard Model Higgs production was observed. After combining the data from all four LEP experiments the significance of the signal was, however, slightly below three standard deviations and the CERN management did not recommend a prolongation of LEP running in 2001. All LEP experiments including L3 have produced exceptionally large samples of data. All four experiments, as well as CERN, recognized the importance to extract the maximum of information from these unique data samples, characterized by clean signals and very small backgrounds.

The most important physics processes investigated at LEP are Z and W boson production, searches for the Higgs boson and supersymmetric particles, as well as for other phenomena beyond the Standard Model, and the rich and extensive field of photon-photon collisions. As Figure 2.2 demonstrates, two-photon reactions with hadronic final states are the dominant process at LEP2 energies. A hadronic final state occurring in a two-photon collision is regarded as revealing the "hadronic component" of the photon, described in more details in Chapter 4.

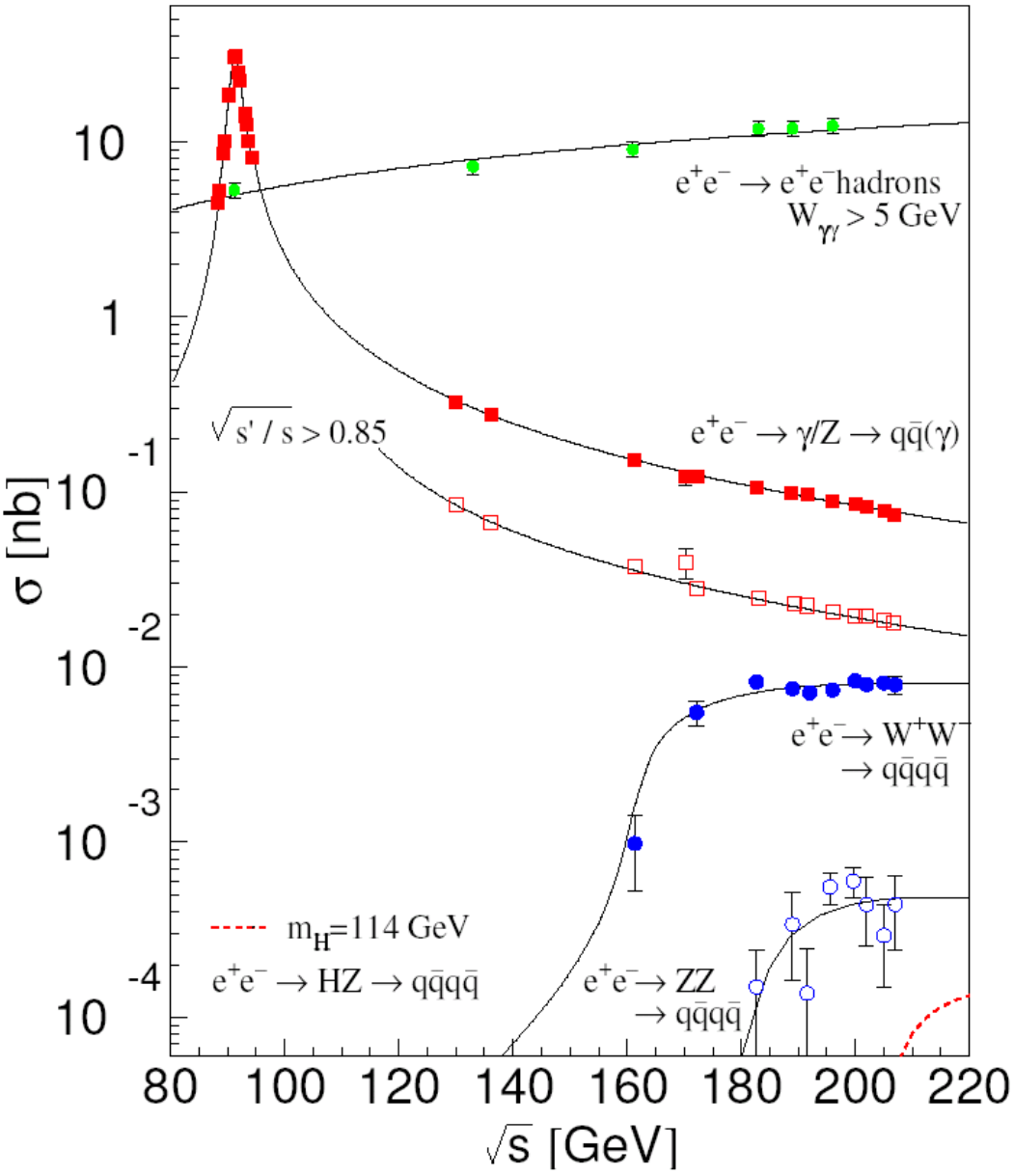

Figure 2.2 Cross sections for several processes at different LEP energies [4].

2.2. About particle detection at e^+e^- colliders

Detectors in high energy physics are very complex and costly devices. A devoted and long-term effort of hundreds of physicists, engineers, and technicians is needed to build and operate them.

The goal of experimental particle physics is the measurement of particle properties and reaction probabilities, "cross sections". After the interaction of the particle beams, bursts of various particles are moving outward in all directions. By determining their type (mass, charge, spin, flavor, etc.), momentum/energy, angle, and how often they occur, we can study these objects and try to have a better understanding of them and their interactions.

Detection is based on the interaction of radiation with matter. In this sense particles can be divided in two main categories. In the first group are the charged particles: heavy charged particles such as μ, π, p, α, light nuclei, and light charged particles such as e^+, e^-. The other group comprises the neutral particles: n, γ-radiation and neutrinos. There are two principle effects during the passage of charged particles trough matter. Due to electromagnetic processes, such as inelastic collisions with shell electrons of the medium and elastic scattering off nuclei, these particles lose energy and change directions. We are mostly interested in the statistical sum of such interactions. However, there are also other processes that can contribute: Bremsstrahlung, emission of Cherenkov radiation, nuclear reactions,

emission of transition radiation. Neutral particle interaction with matter can occur trough energy transfer to charged particles. As an example neutrons interact with heavy charged particles, γ-radiation with electrons, and neutrinos with heavy charged particles and electrons.

Large detectors consist of several subsystems; each designed to perform different tasks. Particles that have a lifetime of about 10^{-11} sec or longer can be detected. Heavy charged particles such as muons go through large amount of materials without slowing down. These are detected by muon chambers situated in the outer shell of the whole detector setup. In order to have precise measurements of charged particle momenta, large magnetic fields are applied that bend the tracks of these particles. Charged particle tracking devices are placed close to the beam pipe and they can be cylindrical wire chambers, silicon detectors, or time-of-flight (TOF) scintillation counters. For detection of those particles that have a very short lifetime, such as τ leptons, b and c quarks, vertex detectors are used. By observing the final-state particles from the collision one can work backwards and deduce which unstable particle was produced. Photons and electrons lose energy by scattering and by radiating other photons and electrons. They create so-called electron showers during their passage. The electromagnetic energy deposited this way can be detected by electromagnetic calorimeters (ECAL). Photons can be distinguished from electrons since the electrons show up in both ECAL and tracking devices while photons show up only in the ECAL. The detection of

hadrons is based also on calorimetery. Hadrons interacting with nuclei lose energy in their collisions and will further interact with other hadrons. They produce hadron showers that are much wider than electron showers; hence they can be easily distinguished. The deposited energy is detected by hadron calorimeters (HCAL). Neutrinos are neutral particles that cannot be measured directly by the detectors. However, we can measure their missing momentum by applying momentum conservation to the other particles. In addition, one has to be sure that the energy of all the particles that participated in this interaction is well measured.

Electron-positron colliding beams are the main devices for exploring two-photon $\gamma\gamma \rightarrow h$ and one-photon $\gamma \rightarrow h$ processes. The only obstacle is to design and build detectors that can fulfill the requirements for both processes. Two-photon events are boosted in the direction of one or both electron-positron beams while for one photon events the laboratory system coincides with the center of mass system. Another difference is that two-photon events occur at lower energies than one-photon events. The advantage of this low energy is that these two processes can be easily separated. The disadvantage is that the low-energy background, such as beam gas events, is hard to separate from two-photon events. This affects detection efficiency and triggering. The trigger threshold has to be increased to reduce this background.

For a highly efficient detection the detectors should cover a 4π solid angle. However, in real life this is not the case. About 10 to 20 % of this angle is not

covered leaving acceptance holes close to the beam pipe. It means that a significant amount of the events is lost in these regions that later when we analyze data has to be recovered using simulation programs (Chapter 5).

2.3. The L3 detector

L3 is a general-purpose detector, designed and built to detect particles that come from the e^+e^- collision (Figure 2.3). It is especially good for the study of electrons, photons, and muons, since it has a very good energy or momentum resolution for these. A more detailed description of the L3 detector is given in [5], [6], [7], [8], [9]. Only such aspects will be emphasized here that are relevant for this analysis.

The L3 detector is unique for the study of two-photon processes because of its excellent resolution for photons and charged hadrons and because of an unbiased track trigger (Section 2.4).

L3 has several subdetectors arranged in a layered structure: central tracker, electromagnetic and hadronic calorimeters, and muon drift chambers. A uniform magnetic field of 0.5 T produced by a large magnet (length 14 m, height 16 m, mass 7500 ton of carbon steel and aluminum) along the beam line allows measurement of the transverse momentum of charged particles. Luminosity of electron positron collisions is measured with the luminosity monitor (LUMI).

The most relevant detectors for this analysis are shown in Figure 2.4. The detector situated closest to the beam pipe is the Silicon Microvertex Detector (SMD). It is designed to provide high precision position measurements near the interaction point. The measurements allow for reconstruction of the tracks to determine the decay point, i.e. the "vertex", of short-lived particles such as the τ lepton. The SMD is a micro-strip semiconductor detector. It consists of two cylindrical layers of double-sided silicon strip detectors. It has a resolution of 7 μm in the transverse plain and 15 μm along the beam pipe.

The next detector surrounding the SMD is the Time Expansion Chamber (TEC), also called L3 Vertex Chamber. The TEC measures the bent tracks of charged particles over a half-meter range from the creation point. This detector is made of two layers of drift chambers, positioned cylindrically around the main z axis.

The Electromagnetic Calorimeter (ECAL), made of 1100 Bismuth Germanium Oxide crystal cells, measures the energies and positions of electrons and photons with energies ranging from 100 MeV to 100 GeV. Their deposited energy is transformed into light that we can measure. The crystals have the role of producing scintillation light and channeling. This light coming from the particles to photodiodes are then connected to readout electronics. This detector has an excellent energy resolution over a wide range, 5% at 100 MeV and 1% above 1 GeV.

The Hadron Calorimeter (HCAL) measures the energy deposited by particles and jets of particles. It can also contribute to the identification of muons and the monitoring of the direction of the energy flow. This device has three main parts: the barrel situated at the center, a muon filter located in the outer shell and two endcaps. The barrel and the endcaps are made of depleted uranium absorber plates (weight of 300 tons) interspersed between 7968 proportional wire chambers.

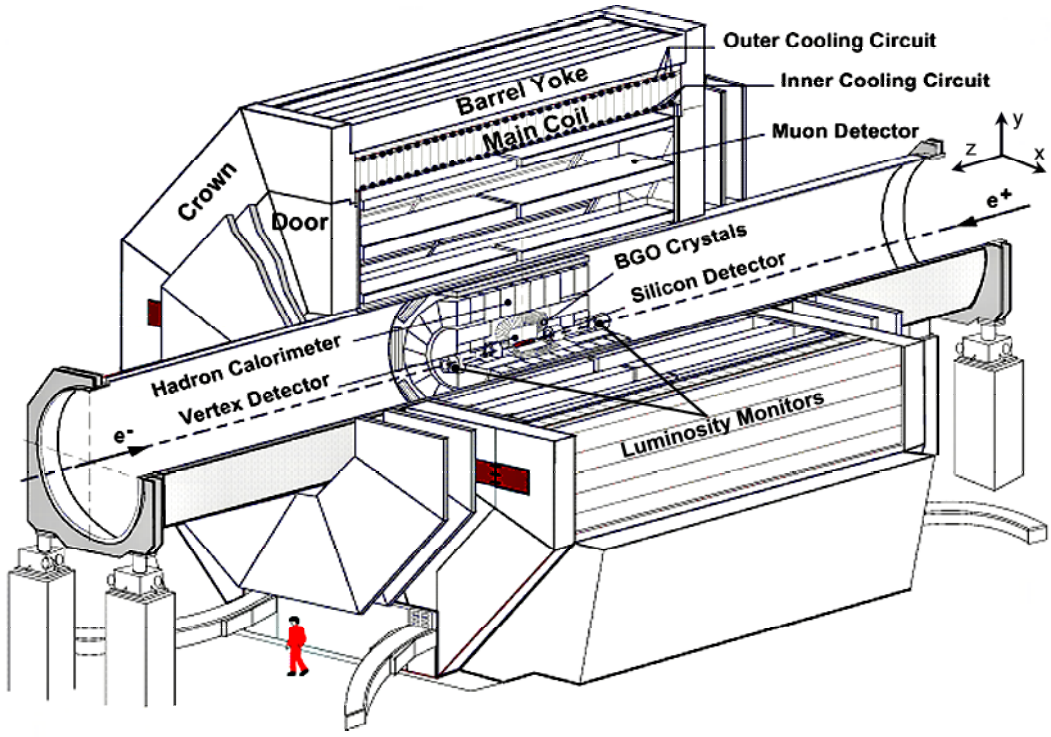

Figure 2.3 Picture of the L3 experiment.

The L3 subdetectors in the forward region that are capable of "tagging" photon events occurring at small scattering angles are the Very Small Angle Tagger (VSAT), the Luminosity Monitor (LUMI), the Active Lead Rings (ALR) and the Electromagnetic Calorimeter (ECAL) endcaps (Figure 2.4). These are all calorimetric detectors similar to the ECAL.

The Luminosity Monitor is designed to measure the rate of collisions of the electrons and positrons, but it also can be used to study the physics of two-photon collisions. The LUMI electromagnetic calorimeters are placed at $z = \pm 2.65$ m with the forward part in the direction of the electron and the backward part in the direction of the positron. The angular coverage is $32.6 \leq \Theta \leq 63.6$ mrad. The calorimeters in Figure 2.5 (a) are made of 304 radiation resistant BGO crystals, arranged in 16 sectors of 19 crystals. The silicon detector shown in Figure 2.5 (b) placed in front of each monitor measures the polar angle θ and the azimuthal angle ϕ with very good accuracy.

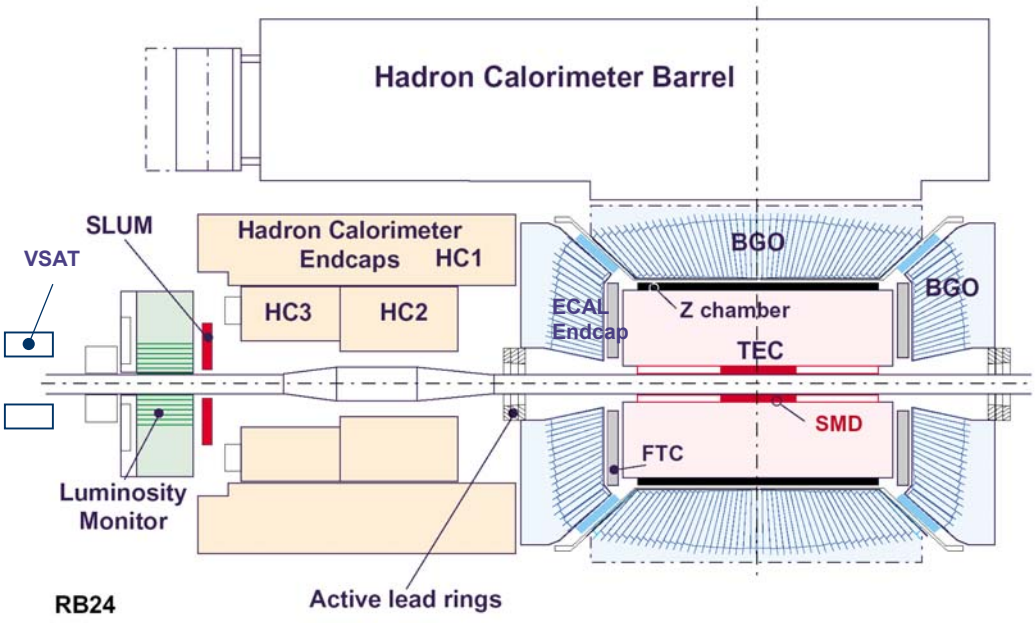

Figure 2.4 Schematic view of the central and forward region of the L3 detector.

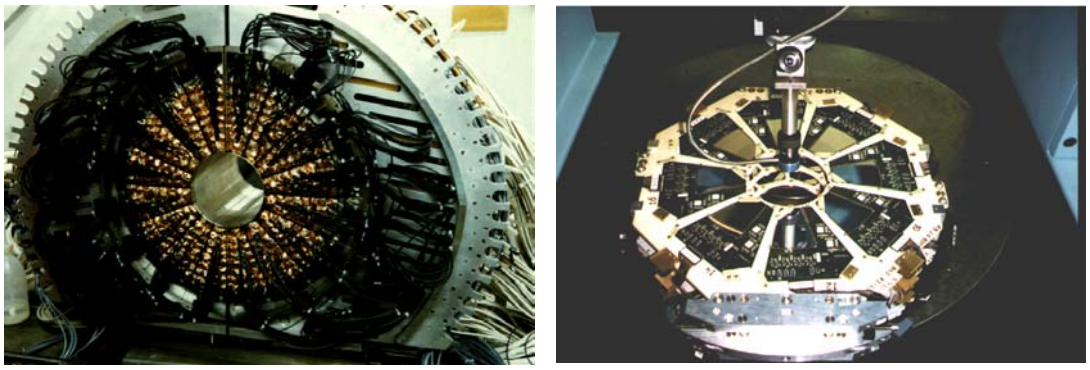

(a) (b)

Figure 2.5 Pictures of the LUMI calorimeter and silicon detector.

2.4. The L3 Trigger System

In general, a trigger system is needed to select events of physics interest and to reject as much background "noise" as possible.

In the L3 experiment events are triggered at three levels [10].

The level-1 consists of five independent hardware triggers:

- TEC trigger based on the TEC chamber,
- Energy trigger based on the calorimeters,
- Luminosity trigger based on the luminosity monitor,
- Scintillator trigger based on the scintillator counters,
- Muon trigger based on the muon chambers.

The level-1 trigger performs a logical OR operation on these individual triggers. They start operation at each beam crossing. To give an example, trigger level-1 has 22 μs in 4 bunch mode to decide if an electron-positron interaction occurred. Typical trigger rate is 10-20 Hz, with 45 kHz beam crossing rate. On a positive decision of any of these triggers the events are digitized and recorded until the next trigger level is available. The TEC trigger selects events with one ore more tracks. The energy trigger requires minimum energy deposition in the electromagnetic or hadronic calorimeter. The luminosity trigger requires energy deposition in the luminosity monitors. The muon trigger requires at least one reconstructed track in the muon spectrometer.

Level 2 trigger makes use of the level-1 trigger data. This level rejects 30-50 % of the events accepted by level-1. Its main purpose is to reject background events. A typical trigger rate for level 2 is about 6 Hz.

The level-3 trigger performs a complete reconstruction of the events from all the subdetectors. The event writing rate at this level is reduced to 2-3 Hz. In Figure 2.6 a sketch of the architecture of the L3 data acquisition system is shown.

Between each bunch crossing, the low precision data is transferred to the level 1 trigger. The accepted events from this level are transferred into subdetector memories from where they are collected by the Subdetector Event Builder. Those events that are accepted by level 2, coming from the different subdetectors, are then combined into one event by a Central Event Builder. The event is then dispatched to one of the level 3 processors. The events accepted by level 3, not bigger than a certain size (34 Kbyte), are transferred to an online computer and are stored on disks.

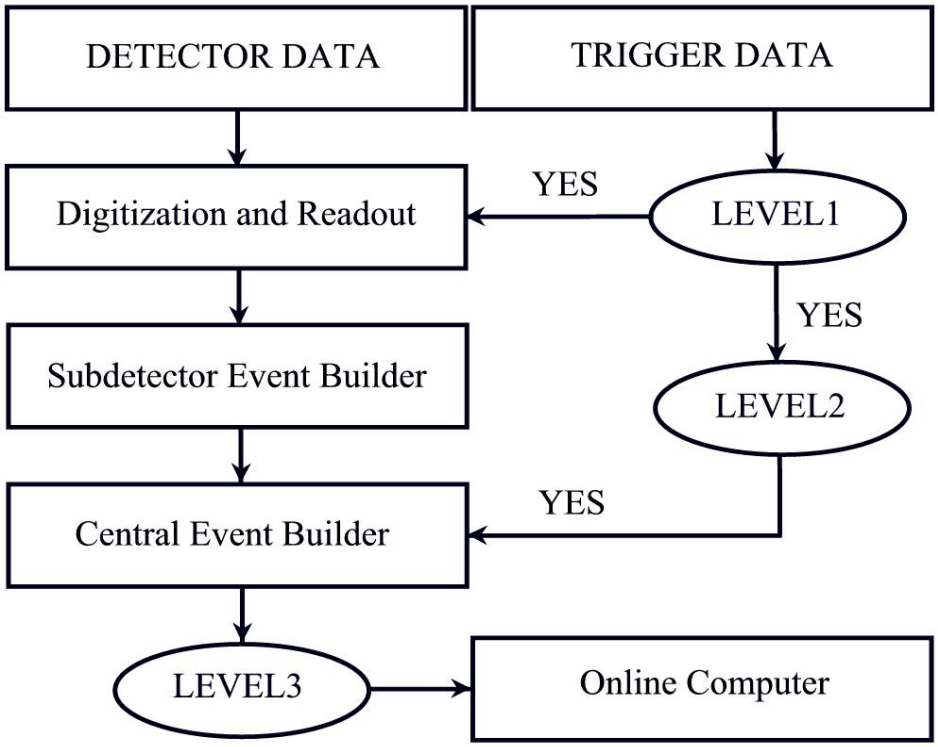

Figure 2.6 Schematic view of the L3 data acquisition system [10].

Chapter 3

3. KINEMATICS

3.1. The two-photon process and basic variables

The schematic representation of the reaction

$$e(k_1)\,e(k_2) \rightarrow e(k_1^{'})\,e(k_2^{'})\,\gamma_1^{(*)}(q)\,\gamma_2^{(*)}(p) \rightarrow e(k_1^{'})\,e(k_2^{'})\,f(p_{f_1})\,\bar{f}(p_{f_2}) \qquad (3.1)$$

where two electrons scatter via the exchange of two virtual photons is shown in Figure 3.1.

- $e(k_i)$, (i=1,2) are the incoming electron beams with four-momenta $k_i = (E_i, \vec{k_i})$, where $E_i = E_{beam}$ is the beam energy, and $\vec{k}_i$ are the momentum vectors.
- $e(k_i^{'})$, (i=1,2) are the scattered electron beams with four-momenta $k_i^{'} = (E_i^{'}, \vec{k_i^{'}})$, where $E_i^{'}$ are the energies of the scattered electrons, and $\vec{k}_i^{'}$ are the momentum vectors.

- $\gamma_1^*(q)$ and $\gamma_2^*(p)$ are the virtual photons emitted by the scattered electrons, with four-momenta $q = (E_{\gamma_1^{(*)}}, \vec{q})$ and $p = (E_{\gamma_2^{(*)}}, \vec{p})$. The symbol (*) indicates that the photons can be either virtual or quasi-real.
- The result of this interaction in leading order is a fermion-antifermion pair $f(p_{f_1})\bar{f}(p_{\bar{f}_2})$ with four-momenta $p_{f_i} = (E_{f_i}, \vec{p}_{f_i})$, where E_{f_i} and $\vec{p}_{f_i}$ are the fermion energies and three-momentum vectors.

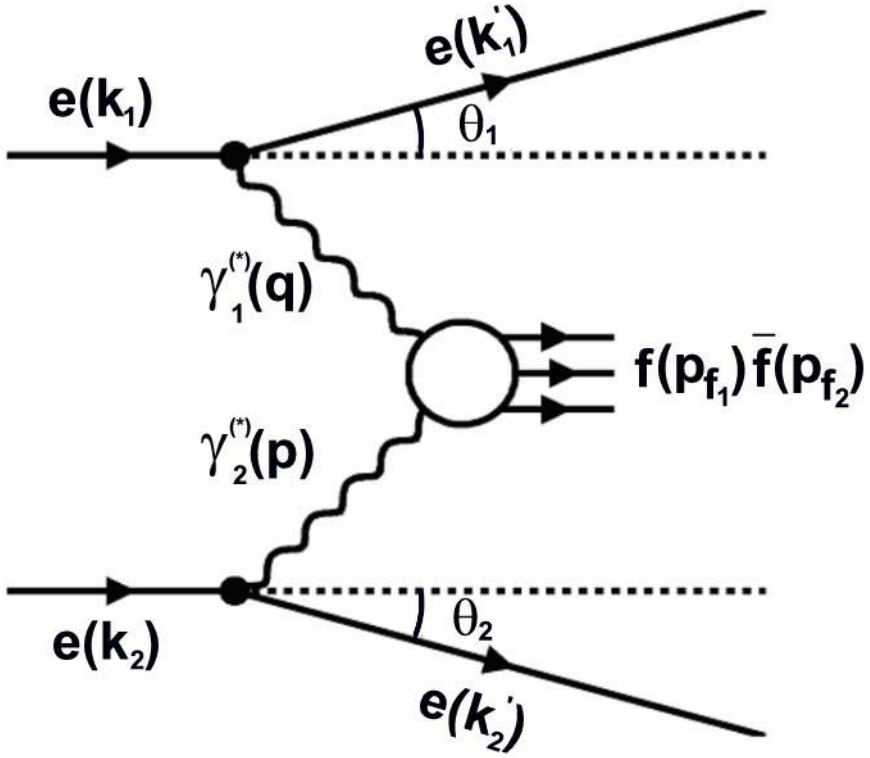

Figure 3.1 Schematic representation of the two-photon reaction.

The "virtuality" of the photon is defined as the negative value of the four-momentum transfer squared

$$Q^2 = -q^2 = \vec{q}^{\,2} - E^2_{\gamma_1^{(*)}} \tag{3.2}$$

and

$$P^2 = -p^2 = \vec{p}^{\,2} - E^2_{\gamma_2^{(*)}}\,. \tag{3.3}$$

The "mass squared" $W_{\gamma\gamma}$ of the two-photon system is

$$W^2_{\gamma\gamma} = (q+p)^2 = Q^2\,\frac{1-x}{x} - P^2\,, \tag{3.4}$$

where the Bjorken scaling variable (Section 4.1) is

$$x = \frac{Q^2}{2p\cdot q} = \frac{Q^2}{W^2_{\gamma\gamma} + Q^2 + P^2}\,. \tag{3.5}$$

For known energies $E_i = E_{beam}$, E_i' and the scattering angles θ_i, considering that the mass of the electron m_e is negligible ($m_e << E_i, E_i'$), Q^2 and P^2 can be determined from

$$Q^2 = -(k_1' - k_1)^2 \cong 2E_1'E_{beam} - 2\overrightarrow{k_1}'\overrightarrow{k_1} \cong 2E_1'E_{beam} - 2E_1'E_{beam}\cos\theta_1\,,$$

$$P^2 = -(k_2^{'} - k_2)^2 \cong 2E_2^{'}E_{beam} - 2\overrightarrow{k_2}^{'}\overrightarrow{k_2} \cong 2E_2^{'}E_{beam} - 2E_2^{'}E_{beam}\cos\theta_2 ,$$

and so

$$Q^2 \cong 2E_1^{'}E_{beam}(1-\cos\theta_1) , \tag{3.6}$$

$$P^2 \cong 2E_2^{'}E_{beam}(1-\cos\theta_2) .$$

3.2. Special kinematical situations

In experiments, in order to identify two-photon events one can tag the interacting photons by detecting the scattered electrons. Three kinematical situations are possible: double, single, and no-tag events.

3.2.1. The double-tag process

In the double-tag process both electrons are detected. This method provides the full information on the $\gamma\gamma$ system. However, there are some restrictions that one has to consider. Tagging at small angles is problematic in most cases because of the relatively high background coming from Bhabha and beam-gas scattering, as discussed in (Section 2.2). Another negative side of this measurement is that in practice the complete kinematical information on the $\gamma\gamma$ system cannot be obtained

at high energies. Therefore, $W_{\gamma\gamma}$ is measured less accurately. This is the reason why in most cases the other two tagging methods are preferred.

3.2.2. The no-tag process

In the "no-tag" process the electrons are scattered at very small angles and they remain undetected. The virtualities of both photons are very low and they are considered quasi-real. Since the electrons are out of the tagging detector range, the polar angles and therefore Q^2 and P^2 cannot be measured. $W_{\gamma\gamma}$ can be determined only from the final state. In this process one takes advantage of the fact that photons are dominantly radiated along the beam axis, and the transverse momentum of the two-photon system with respect to the beam is small. If all particles of the final state are measured, then the reconstructed total transverse momentum distribution has a peak at low values. The distribution is flat at low values if particles from the final state are missing.

3.2.3. The single-tag process

In the "single-tag" case one of the electrons is scattered at a large angle and is detected by one of the low-angle tagging detectors. The photon emitted by the "tagged" electron has high virtuality Q^2. For this reason we can talk about deep-inelastic electron-photon scattering. The other electron is scattered at a very small angle and disappears in the beam pipe, remaining undetected. The quasi-real

photon emitted by the "anti-tagged" electron has a low virtuality P^2. Two-photon interaction results in hadrons. Because the detectors are not covering the full solid angle around the interaction point, not all hadrons are detected and therefore $W_{\gamma\gamma}$ is only partially known.

3.3. Equivalent photon approximation (EPA)

Experimentally, we measure the integrated cross section $\Delta\sigma_{ee}$ for the reaction $e^+e^- \rightarrow e^+e^-\text{hadrons}$ in the kinematical region defined by ΔQ^2, ΔP^2, and ΔW. Instead of writing the differential cross section $d\sigma_{ee}$ in terms of the cross sections corresponding to specific helicity states of the photon one can write it in terms of $d\sigma_{e\gamma^{(*)}}(e\gamma^{(*)} \rightarrow e\,\text{hadrons})$ and the flux of quasi-real target photons $N_{\gamma^{(*)}}(z, \theta_2^{max})$

$$d\sigma_{ee} = d\sigma_{e\gamma^{(*)}} N_{\gamma^{(*)}}(z, \theta_2^{max}) dz . \tag{3.7}$$

The cross section $\sigma_{e\gamma^{(*)}}$ from equation (3.7) can be written as

$$d\sigma_{e\gamma^{(*)}} = \Gamma_T \sigma_{\gamma^*\gamma^{(*)}} dQ^2 dP^2 dW , \tag{3.8}$$

where

$$\Gamma_T = \frac{\alpha E_{tag}}{2\pi^2 Q^2 y}\left[1 + (1-y)^2\right] \tag{3.9}$$

is the flux of the transversely polarized virtual photons and

$$y = 1 - \frac{E_{tag}}{2E_{beam}}(1 + \cos\theta_{tag}) . \tag{3.10}$$

The target photon flux from equation (3.7) is given by the relation [11]

$$N_{\gamma^{(*)}}(z, \theta_2^{max}) = \frac{\alpha}{\pi}\frac{1}{z}\left[(1 + (1-z)^2)\ln\frac{E_{beam}(1-z)\theta_2^{max}}{m_e z} - (1-z)\right], \tag{3.11}$$

where $z = E_{\gamma^{(*)}} / E_{beam}$, $E_{\gamma^{(*)}}$ is the energy of the quasi-real photon, and $\theta < \theta_2^{max}$ is the scattering angle of the electron that remains undetected. The effective cross section is

$$\sigma_{\gamma^*\gamma^{(*)}} = \sigma_{TT} + \varepsilon\sigma_{LT} , \tag{3.12}$$

where σ_{TT} and σ_{LT} are the cross sections that correspond to different helicity states of the photon (T = transverse and L = longitudinal). ε is the ratio of the corresponding photon fluxes written as

$$\varepsilon = \frac{\Gamma_L}{\Gamma_T} = \frac{2(1-y)}{1+(1-y^2)}. \tag{3.13}$$

Therefore, the integrated cross section $\Delta\sigma_{ee}$ becomes

$$\Delta\sigma_{ee} = \int N_{\gamma^{(*)}} (\Gamma_T \sigma_{TT} + \Gamma_L \sigma_{LT})\, dQ^2 dP^2 dW . \tag{3.14}$$

Considering σ_{TT} and σ_{LT} almost constant

$$\Delta\sigma_{ee} = \int N_{\gamma^{(*)}} \Gamma_T \sigma_{\gamma^*\gamma^{(*)}}\, dQ^2 dP^2 dW = \sigma_{\gamma^*\gamma^{(*)}} \int L_{TT} dQ^2 dP^2 dW = \sigma_{\gamma^*\gamma^{(*)}} \Delta L , \tag{3.15}$$

where ΔL is the integrated luminosity function.

All of this can be written in terms of the two structure functions F_T^γ and F_L^γ so the differential cross section is [12], [13], [14]

$$\frac{d\sigma_{ee}}{dx dQ^2 dz dP^2} = \frac{dN_{\gamma^{(*)}}}{dz dP^2} \cdot \frac{d\sigma_{e\gamma}}{dx dQ^2} , \tag{3.16}$$

$$\frac{d\sigma_{ee}}{dxdQ^2dzdP^2} = \frac{dN_{\gamma^{(*)}}}{dzdP^2} \cdot \frac{2\pi\alpha^2}{xQ^4}\left[1+(1-y)^2\right]$$

$$\times\left[2xF_T^{\gamma}(x,Q^2) + \frac{2(1-y)}{1+(1-y)^2}F_L^{\gamma}(x,Q^2)\right]. \qquad (3.17)$$

Defining $F_2^{\gamma} = 2xF_T^{\gamma} + F_L^{\gamma}$, we can obtain the widely used formula

$$\frac{d\sigma_{ee}}{dxdQ^2dzdP^2} = \frac{dN_{\gamma^{(*)}}}{dzdP^2} \cdot \frac{2\pi\alpha^2}{xQ^4}\left[\left(1+(1-y)^2\right)F_2^{\gamma}(x,Q^2) - y^2F_L^{\gamma}(x,Q^2)\right]. \qquad (3.18)$$

The factor

$$\frac{dN_{\gamma^{(*)}}}{dzdP^2} = \frac{\alpha}{2\pi}\left[\frac{1+(1-z)^2}{z}\frac{1}{P^2} - \frac{2m_e^2 z}{P^4}\right] \qquad (3.19)$$

describing the flux of transversely polarized quasi-real photons of finite virtuality is the equivalent photon approximation (EPA), first derived in [15].

Chapter 4

4. THE HADRONIC COMPONENT OF THE PHOTON

4.1. Bjorken Scaling

At low Q^2 the photons are expected to interact like hadrons. The deep inelastic scattering $e^+e^- \rightarrow e^+e^-$ hadrons can be interpreted in analogy to deep inelastic electron-nucleon scattering.

Consider that the proton is made of point-like, spin-1/2 quarks. In deep inelastic scattering, the small wave length, i.e. high Q^2 virtual photon "resolves" the quark content within the proton. For deep inelastic scattering of an electron on a proton target (Figure 4.1) the differential cross section can be written as [1]

$$\frac{d\sigma}{dE'd\Omega} = \frac{4\alpha^2 E'^2}{q^4}\left(W_2(\nu, q^2)\cos^2\frac{\theta}{2} + 2W_1(\nu, q^2)\sin^2\frac{\theta}{2}\right), \qquad (4.1)$$

where W_2 and W_1 are the proton structure functions, $q = k - k'$ is the momentum transfer, $\nu = E - E'$ is the energy transfer, and θ is the scattering angle of the

electron. For the proton initially at rest, $p = (M,0)$, consider $p' = k - k' + p$ and $k^2 = k'^2 \cong 0$. The kinematic reactions are

$$q^2 \cong -2k \cdot k' \cong -2EE'(1-\cos\theta) = -4EE'\sin^2\frac{\theta}{2}. \tag{4.2}$$

Squaring $q + p = p'$, we obtain

$$q^2 = -2p \cdot q = -2\nu M, \tag{4.3}$$

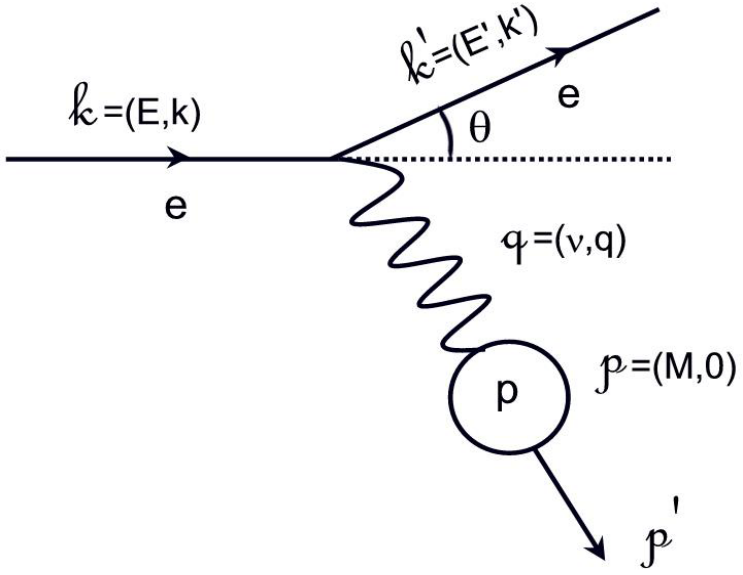

Figure 4.1 The process $ep \to ep$ in the laboratory frame.

$$\nu \equiv E - E' = -\frac{q^2}{2M}. \tag{4.4}$$

For scattering with very small wave length, i.e. large $Q^2 = -q^2$, the proton starts to behave like a free Dirac particle (a quark). The quark inside the proton is considered to be point-like. The differential cross section from equation (4.1) becomes the cross section for a point-like particle. We can consider the cross section for the muon scattering $e^-\mu^- \to e^-\mu^-$ process

$$\left\{\frac{d\sigma}{dE'd\Omega}\right\}_{e\mu\to e\mu} = \frac{4\alpha^2 E'^2}{q^4}\left(\cos^2\frac{\theta}{2} - \frac{q^2}{2m^2}\sin^2\frac{\theta}{2}\right)\delta\left(\nu + \frac{q^2}{2m}\right), \tag{4.5}$$

where m represents the mass of the quark. The structure functions in equation (4.1) are

$$2W_1^{point} = \frac{Q^2}{2m^2}\delta\left(\nu - \frac{Q^2}{2m}\right), \tag{4.6}$$

$$W_2^{point} = \delta\left(\nu - \frac{Q^2}{2m}\right). \tag{4.7}$$

In the high Q^2 limit the inelastic electron-proton scattering can be viewed as elastic scattering of an electron on a "free" quark inside the proton.

For elastic electron-proton scattering the differential cross section is

$$\frac{d\sigma}{dE'd\Omega} = \frac{4\alpha^2 E'^2}{q^4}\left(\frac{G_E + \tau G_M^2}{1+\tau}\cos^2\frac{\theta}{2} + 2\tau G_M^2 \sin^2\frac{\theta}{2}\right)\delta\left(\nu + \frac{q^2}{2M}\right), \qquad (4.8)$$

where $\tau = -q^2/4M^2$ and M is the mass of the proton. The two factors $G_E(q^2)$ and $G_M(q^2)$ are related to the proton charge and magnetic moment distributions

$$G_E \equiv F_1 + \frac{\kappa q^2}{4M^2}F_2 \text{ and } G_M \equiv F_1 + \kappa F_2, \qquad (4.9)$$

where, F_1 and F_2 are the nucleon form factors. In the $q^2 \rightarrow 0$ limit the probe cannot distinguish the constituents in the nucleon. The long wavelength photons will see a particle of charge e and magnetic moment $(1+\kappa)\cdot E/2M$. Here, κ is the anomalous moment of the proton and it is measured to be 1.79 [1]. The anomalous moment for the neutron is κ = -0.91. In this limit, we must choose the nucleon form factors as follows: $F_1(0) = 1$, $F_2(0) = 1$ for the proton and $F_1(0) = 0$, $F_2(0) = 1$ for the neutron.

To obtain the structure function for a point-like particle we use the identity $\delta(x/a) = a\delta(x)$ in equations (4.6), (4.7).The dimensionless structure functions can be written as:

$$2mW_1^{point}(\nu, Q^2) = \frac{Q^2}{2m\nu}\delta\left(1 - \frac{Q^2}{2m\nu}\right), \tag{4.10}$$

$$\nu W_2^{point}(\nu, Q^2) = \delta\left(1 - \frac{Q^2}{2m\nu}\right). \tag{4.11}$$

These "point" structure functions are only functions of $Q^2/2m\nu$. In this case, $\kappa = 0$ and $F_1(q^2) = 1$ for all q^2. Introducing these values into equations (4.9) we obtain that $G_E = G_M = G$. Comparing the cross sections for deep inelastic scattering (4.1) with cross sections for elastic electron-proton scattering (4.8), the structure functions can be written as

$$W_1^{elastic} = \frac{Q^2}{4M^2}G^2(Q^2)\delta\left(\nu - \frac{Q^2}{2M}\right), \tag{4.12}$$

$$W_2^{elastic} = G^2(Q^2)\delta\left(\nu - \frac{Q^2}{2M}\right). \tag{4.13}$$

Comparing this to the point-like structure functions from equations (4.10) and (4.11) these structure functions contain a form factor $G(Q^2)$ called the proton dipole form factor

$$G = \left(1 - \frac{q^2}{0.71}\right)^{-2}. \tag{4.14}$$

With increasing Q^2, above 0.71 GeV^2, the chance to have an elastic scattering becomes less and the proton starts to reveal its structure. At high Q^2 the dependence of the inelastic structure functions on $Q^2 = -q^2$ decreases until it vanishes. These become only function of the "Bjorken variable" $x = \frac{Q^2}{2q \cdot p} = \frac{Q^2}{2M\nu}$. Therefore, for deep inelastic electron-proton scattering

$$\nu W_2(\nu, Q^2) \to F_2(x), \tag{4.15}$$

$$MW_1(\nu, Q^2) \to F_1(x) = \frac{1}{2x} F_2(x), \tag{4.16}$$

where $F_{1,2}$ are the inelastic structure functions. For fixed x, these functions are independent of Q^2. The photon is interacting with point-like particles with no form factors being involved. We say that $F_{1,2}$ "satisfy Bjorken scaling".

Summing $F_{1,2}$ over all partons making up the proton, we can write that

$$F_2(x) = \sum_i e_i^2 x f_i(x) = 2xF_1(x), \qquad (4.17)$$

where i = quarks and gluons, e_i are the various quark charges, and f_i are probability densities of finding a quark or a gluon inside the proton. These partons can each take away a fraction x of the proton's four momentum.

4.2. Theory of two-photon interactions

The photon has two different appearances. To a first approximation, the photon is a point-like particle, also called the "bare photon". However, it can be also considered as a collection of partons: quarks and gluons, like a hadron. While the proton structure is determined from the valence quark distribution inside the proton, the photon structure is determined by fluctuations of the bare photon into partons. In a direct process (Figure 4.2 a) the photon interacts as a whole. It does not reveal a structure. The processes, where the photon fluctuates into a $q\bar{q}$ pair and subsequently one of the quarks takes part in the "hard" interaction, are called resolved processes (Figure 4.2 b, c).

In the equivalent photon approximation the two photons are produced independently. They can both fluctuate into a hadronic state ($q\bar{q}$ pair) with low or high virtuality. Consequently, hadronic interactions are divided into hard and soft

interactions by a transverse momentum cutoff p_t^{cut}. Those interactions that are characterized by transverse momenta greater than this scale can be calculated by lowest order perturbative QCD. Below this cutoff value we enter the domain of non-perturbative QCD physics. Based on these considerations three main categories of photon-photon interactions can be distinguished (Figure 4.2):

- Soft hadron-like interaction described by the Vector Meson Dominance Model. In this process the photon turns into a vector meson before interacting with the other photon or quark pair.
- Point-like, direct interaction described by the Quark Parton Model (QPM). In this process the bare photon interacts with a parton from the other photon.
- Hard "resolved" processes. In this process the photon fluctuates into a $q\bar{q}$ pair and one of these interacts with a parton from the other photon. A more detailed description of these processes are given in the next sections.

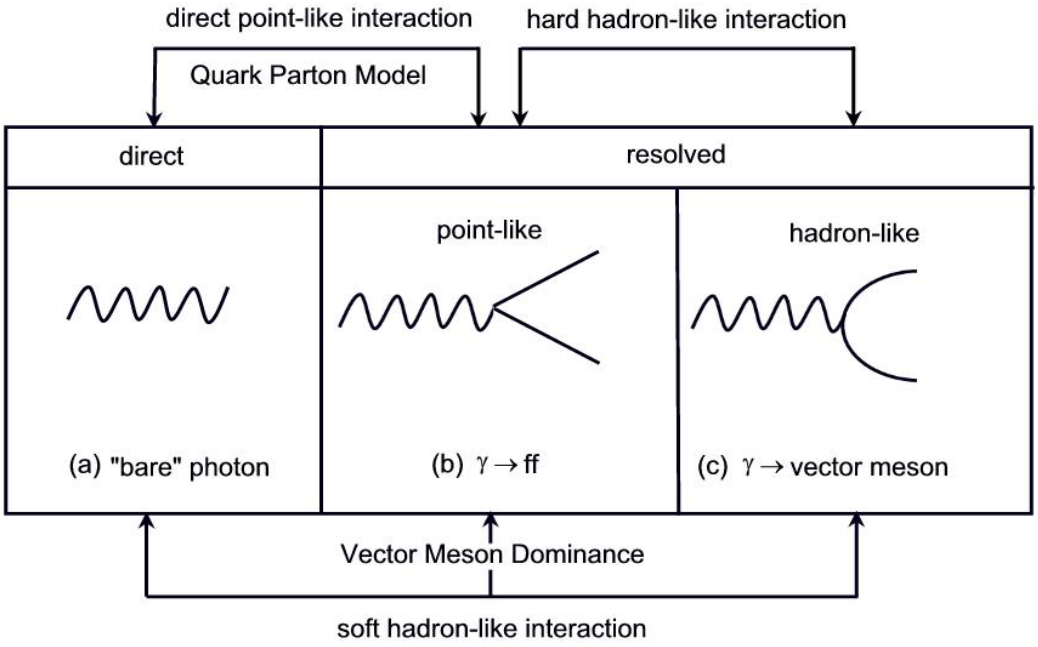

Figure 4.2 The photon as a structureless or resolved entity.

4.2.1. The Vector Meson Dominance Model

When the transverse momenta of the $q\bar{q}$ pair is low, there will be enough time for the system to form a low mass vector meson bound state (ρ, ω or ϕ) before interacting with the other photon or quark pair. This is a "hadron-like" interaction described by the Vector Meson Dominance (VDM) model. The VDM process can be interpreted in analogy with electron-nucleon scattering (Section 4.1). The structure functions are given by (4.17). Ignoring gluon emission, the structure functions show Bjorken scaling, which means that the x distribution is independent of Q^2. This is mainly due to the limited transverse momentum of the partons in the

hadron. With gluon emission and absorption, more momentum goes into radiated gluons as Q^2 increases. In this case, the momentum fraction x shifts to lower values. In the Bjorken limit $Q^2 \to \infty$, for any fixed value of x, the hadronic structure functions $F_{1,2}$ decrease like $1/\ln Q^2$. The leading order diagrams for VDM are shown in Figure 4.3 (a).

4.2.2. The Quark Parton Model

When the transverse momenta of the $q\bar{q}$ pair is large enough, the mass of the pair is large as well and the photon cannot fluctuate anymore into a low mass

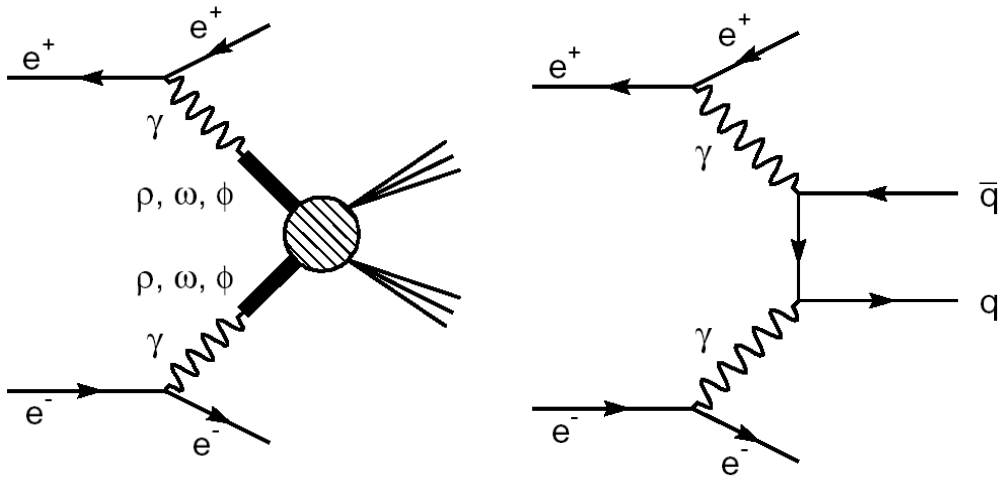

(a) (b)

Figure 4.3 Leading order contributions to the total hadronic two-photon cross section: (a) VDM and (b) QPM.

vector meson state with the same quantum numbers as the photon. In this case, the point-like quarks from the two photons interact "directly" with each other. This is a perturbatively calculable QED process with direct production of a $q\bar{q}$ pair from the two photons, $\gamma\gamma \to q\bar{q}$. This reaction dominates at high virtualities Q^2 and low invariant mass $W_{\gamma\gamma}$ of the produced hadrons. The theory that describes this process is the Quark Parton Model (QPM). The leading order diagram for QPM is shown in Figure 4.3 (b).

4.2.3. QCD

When the scattering is hard enough, the QCD gluon interaction terms become more dominant. The exchanged gluons will be able to distinguish the quark from the antiquark in the photons. These processes are called single-resolved (Figure 4.4 a, b) or double-resolved (Figure 4.4 c). QCD processes can be also divided in resolved processes and corrections to QPM. The latter, includes processes with radiation of gluons at higher order in α_s. They dominate at high virtualities Q^2 and high invariant mass $W_{\gamma\gamma}$ of the produced hadrons. The two diagrams in Figure 4.5 (a), (b) show higher order interaction terms with radiation of gluons in the final state.

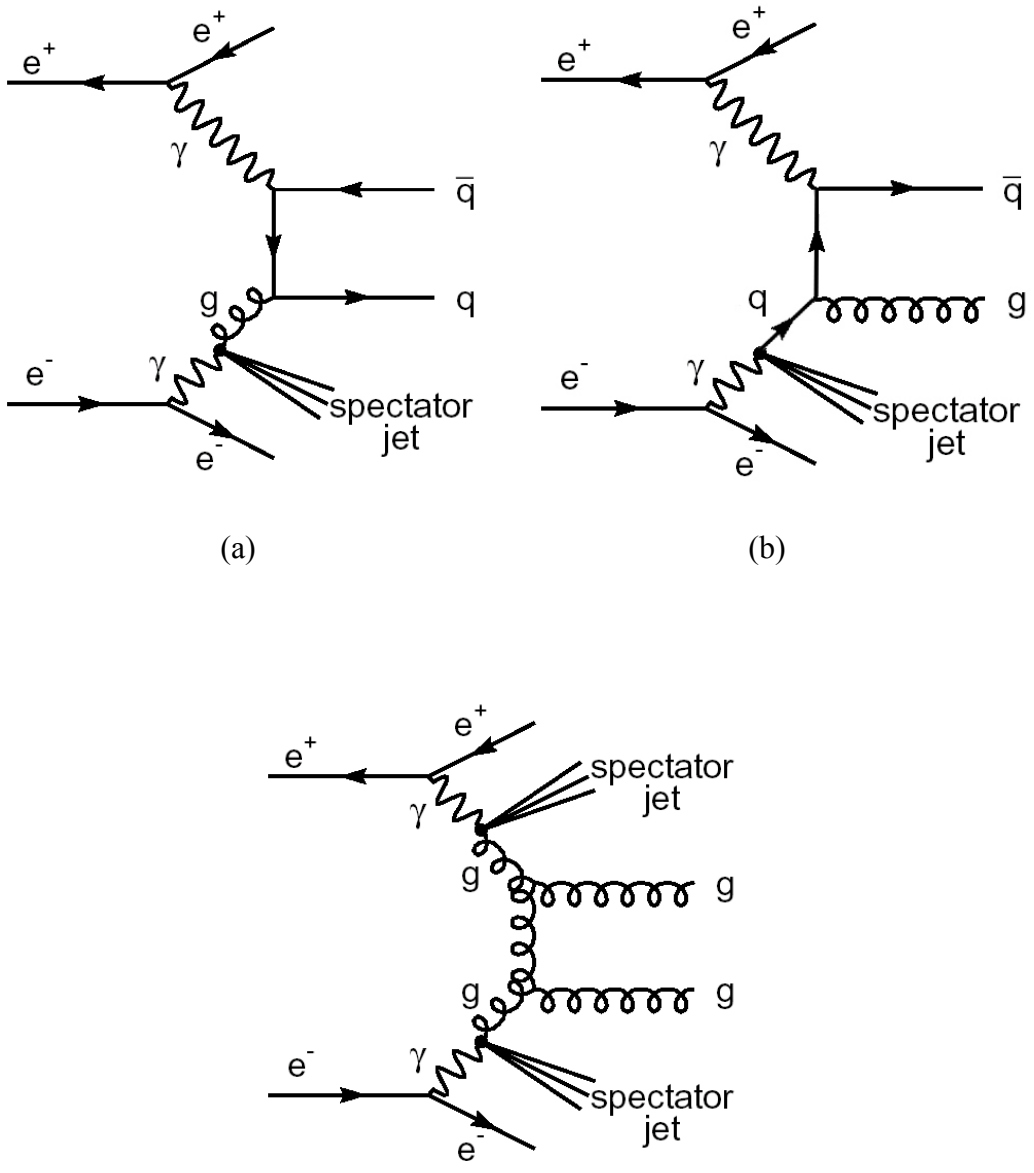

Figure 4.4 QCD contributions to the total hadronic two-photon cross section: single- (a, b) and double resolved processes (c).

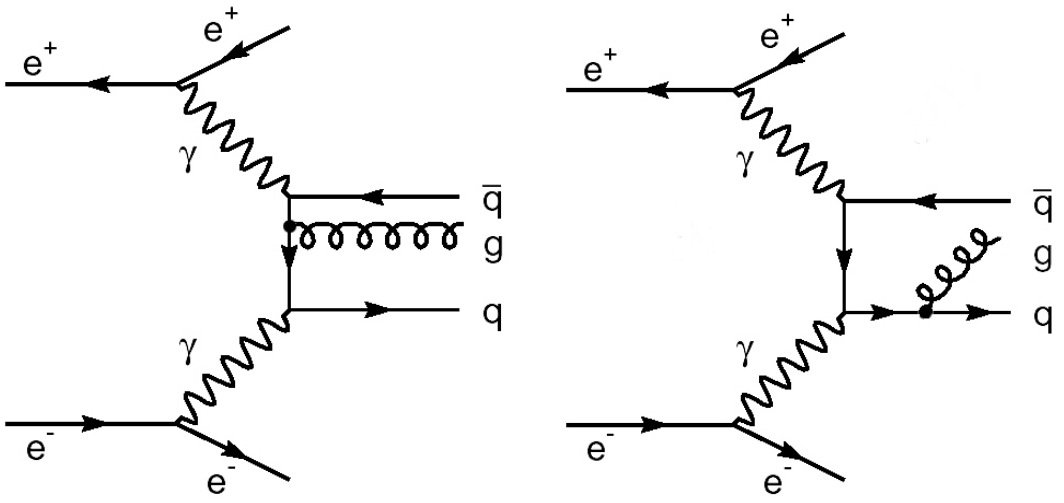

(a) (b)

Figure 4.5 QCD contributions to the total hadronic two-photon cross section: corrections to QPM with radiation of gluons at higher order in α_s .

4.2.4. $\gamma\gamma$ event classes

Since there are two photons, 3 times 3 interactions can be distinguished. From these 9 combinations, 3 cancel out due to the symmetry of the "off-diagonal" combinations. Hence, we can define only 6 different interactions:

1. VMD – VMD: both photons turn into hadrons,
2. VMD – direct: the bare photon interacts with the partons inside the photon, that turned into a vector meson,

3. VMD – resolved: the photon with high virtuality and high mass splits into a $q\bar{q}$ pair, and one of these quarks further interacts with a parton from the other photon turned into a vector meson,
4. direct – direct: is the direct production of a $q\bar{q}$ pair from the two photons, $\gamma\gamma \to q\bar{q}$ (lepton pair production is also possible, but it will not be considered in the present discussion),
5. direct – resolved: the anomalous photons turn into a $q\bar{q}$ pair and one of the quarks interacts directly with the other photon,
6. resolved – resolved: both photons turn into a $q\bar{q}$ pair and one quark from each side will undergo a hard interaction.

4.2.5. Processes dominating in single-tag events

High Q^2 single-tag events favor perturbative QED and QCD diagrams such as $\gamma\gamma \to q\bar{q}$ (Figure 4.3 b), $\gamma g \to q\bar{q}$ (Figure 4.4 a), and $\gamma q \to g\bar{q}$ (Figure 4.4 b). The resolved processes $\gamma g \to q\bar{q}$ and $\gamma q \to g\bar{q}$ are described using parton density functions extracted from the photon structure functions measured in previous experiments at PEP, PETRA, and TRISTAN. Reviews of the existing parametrizations may be found in [16] and [17]. Recently, a new parametrization was obtained adding published LEP data [18].

4.3. Study of the single-tag two-photon reaction at L3

The single-tag process is described here with emphasis on the basic single-tag variables used in the analysis from here on.

At LEP, in the $e^+e^- \to e^+e^-\gamma^*\gamma^{(*)} \to e^+e^-$hadrons (Figure 1.14) reaction, two virtual photons are produced by the incoming electrons and their interaction yields hadrons. If the scattering angle of one of the electrons, $\theta_1 (= \theta_{tag})$, is sufficiently large, it is observed in the low polar-angle electromagnetic calorimeter [9] of the L3 detector, originally devised to detect low angle Bhabha scattering for measuring the LEP luminosity. The four-momentum, k', of this "tagged" electron is measured. For singly-tagged events the second electron is undetected, its polar angle is small and the virtual photon radiated from this electron is quasi-real. Recall that the differential cross section $d\sigma_{e\gamma}/dxdQ^2$ (3.16), (3.17) is given by

$$\frac{d\sigma_{e\gamma\to eX}(x,Q^2)}{dxdQ^2} = \frac{2\pi\alpha^2}{xQ^4}\left[(1+(1-y)^2)\cdot F_2^{\gamma}(x,Q^2) - y^2 F_L^{\gamma}(x,Q^2)\right] \qquad (4.18)$$

with

$$y = (q\cdot p)/(k\cdot p) = 1 - \frac{E_{tag}}{2E_{beam}}(1+\cos\theta_{tag})\,. \qquad (4.19)$$

The variable x given by equation (3.5) depends on the two-photon center-of-mass energy, $W_{\gamma\gamma}$, equal to the effective mass of the produced hadrons. The inelasticity y is small ($y < 0.3$) in the kinematic region of this study and consequently only $F_2^{\gamma}(x, Q^2)$ contributes appreciably to the cross section. Therefore, equation (4.18) becomes

$$\frac{d\sigma_{e\gamma\to eX}(x, Q^2)}{dxdQ^2} = \frac{2\pi\alpha^2}{xQ^4}\left[1 + (1-y)^2\right] \cdot F_2^{\gamma}(x, Q^2). \qquad (4.20)$$

By convention, F_2^{γ}/α is measured, where α is the fine structure constant. Using this approach, the photon structure function has been extensively studied at previous e^+e^- colliders [12] and at LEP [12], [19], [20], [21], [22], [23], [24], [25].

4.4. Theoretical Predictions of the Total $\sigma_{\gamma\gamma}$ Cross Section

The total photoproduction cross section $\sigma_{\gamma^*\gamma^{(*)}}$ can be written as the sum of three contributions

$$\sigma_{\gamma^*\gamma^{(*)}} = \sigma_{VMD} + \sigma_{QPM} + \sigma_{QCD}. \qquad (4.21)$$

Using equation (3.8) we obtain the following relation between the effective two-photon cross section and the structure function $F_2^{\gamma}(x,Q^2)$

$$\sigma_{\gamma^*\gamma^{(*)}}(x,Q^2) = \frac{4\pi\alpha^2}{Q^2} F_2^{\gamma}(x,Q^2)\,. \tag{4.22}$$

4.4.1. The QPM Cross Section

The QPM cross section is given by the sum of the contributions of all active quarks

$$\sigma_{QPM} = \sigma_d + \sigma_u + \sigma_s + \sigma_c\,. \tag{4.23}$$

The contribution from the b quark is very small and it can be neglected. This is due to the high mass (m_b=4.7 GeV/c^2) and fractional charge (-1/3). The general expression for σ_{QPM} (Bethe-Heitler cross section) from QED calculations is

$$\sigma_{QPM} = N_c \sum_{k=1}^{n_c} \frac{4\pi\alpha^2}{Q^2} e_{q_k}^4 \, x\left[(x^2 + (1-x)^2) \ln\frac{W_{\gamma\gamma}^2}{m_{q_k}^2} - 1 + 8x(1-x) \right], \tag{4.24}$$

where N_c=3 is the number of colors, m_{q_k} are the masses of the quarks, e_q are the fractional charges, and the sum runs over all active flavors n_f. α is the fine structure

constant and $W_{\gamma\gamma} = Q \cdot \sqrt{(1-x)/x}$. For the three light quarks d, u, and s we can use the following approximation [26]:

$$\sigma_{QPM} = N_c \sum_{k=1}^{n_f} \frac{4\pi\alpha^2}{Q^2} e_{q_k}^4 \, x \left[x^2 + (1-x)^2\right] \log Q^2 \, . \tag{4.25}$$

In this equation, σ_{QPM} depends on the virtuality of the photon as $(1/Q^2)\log Q^2$. Therefore, the quark parton model already predicts a logarithmic Q^2 dependence of the cross section in QED. Parton densities do not scale as described in Section 4.1 but evolve with Q^2. This cross section is dominant in the high x region.

The QPM structure function is given by the sum of the different quark density contributions

$$F_2^{\gamma} = x \sum_{i=1}^{n_f} e_i^2 [q_i(x, Q^2) + \overline{q_i}(x, Q^2)]. \tag{4.26}$$

More explicitly this can be written as [12], [27], [28]

$$F_{2,QPM}^{\gamma} = N_c \sum_{k=1}^{n_f} \frac{e_{q_k}^4 \, \alpha^2}{\pi} x \left\{ \left[x^2 + (1-x)^2\right] \ln \frac{W_{\gamma\gamma}^2}{m_{q_k}^2} - 1 + 8x(1-x) \right\}. \tag{4.27}$$

4.4.2. The VMD Cross Section

The total cross section $\sigma(\gamma\gamma \to \text{hadrons})$ [29] can be parametrized according to the Generalized Vector Meson Dominance Model [30]

$$\sigma^{\text{GVDM}}_{\gamma\gamma\to\text{hadrons}} = \sum_{VV'} \frac{4\pi\alpha}{f_v^2}\frac{4\pi\alpha}{f_{v'}^2}\sigma^{\text{VMD}}_{VV'}(W_{\gamma\gamma}), \tag{4.28}$$

where $4\pi\alpha/f_V^2$ and $4\pi\alpha/f_{V'}^2$ are form factors giving the probability for a photon to couple to a vector meson ($\pi\alpha/f_V^2 \approx 2.80\cdot10^{-3}, 0.30\cdot10^{-3}, 0.36\cdot10^{-3}$ for ρ, ω, and φ, respectively [31]). $\sigma^{\text{GVDM}}_{\gamma\gamma\to\text{hadrons}}$ is related to nucleon-nucleon and γ-nucleon scattering. It has been measured [31], [32] that for the scattering of two quasi-real photons

$$\sigma^{\text{VMD}}_{\gamma\gamma}(W_{\gamma\gamma}) = A + \frac{B}{W_{\gamma\gamma}} = \frac{[\sigma_{\text{TOT}}(\gamma N, S\to\infty)]^2}{\sigma_{\text{TOT}}(NN, S\to\infty)} + \frac{\sigma_1}{W_{\gamma\gamma}} = 240\,\text{nb} + \frac{270\,\text{nb}\cdot\text{GeV}}{W_{\gamma\gamma}}, \tag{4.29}$$

where $S = W_{\gamma\gamma}^2$, and $\sigma_1/W_{\gamma\gamma}$ is the resonance contribution to the cross section.

The cross section factorized in a mass dependent part and two Q^2 dependent parts can be written as

$$\sigma^{\text{GVDM}}_{ab}(W_{\gamma\gamma}, Q_1^2, Q_2^2) = \sigma^{\text{VMD}}_{\gamma\gamma}(W_{\gamma\gamma},0,0)\cdot F_a^{\text{GVDM}}(Q_1^2)F_b^{\text{GVDM}}(Q_2^2), \tag{4.30}$$

where (a, b) = T for transverse and (a, b) = L for longitudinally polarized photons. The GVDM vector meson form factors are

$$F_T^{GVDM}(Q^2) = \sum_{\rho,\omega,\phi} r_V \left(\frac{m_V^2}{Q^2 + m_v^2} \right)^2 + r_C \frac{m_0}{Q^2 + m_0^2} \tag{4.31}$$

and

$$F_L^{GVDM}(Q^2) = \sum_{\rho,\omega,\phi} r_V \left(\frac{m_V^2}{Q^2 + m_v^2} \right)^2 \frac{Q^2}{4m_V^2}, \tag{4.32}$$

where m_0 = 1.4 GeV is the "continuum term", r_ρ=0.65, r_ω=0.08, r_ϕ =0.05 and $r_C = 1 - \sum r_V$. Contributions of higher mass resonances and of the continuum are approximated by $\sim 1/(1 + Q^2 / m_0^2)$.

The total two-photon cross section $\sigma_{\gamma\gamma}$ can be written as (Section 3.3)

$$\sigma_{\gamma\gamma}(W_{\gamma\gamma}, Q_1^2, Q_2^2) = \sigma_{TT}(W_{\gamma\gamma}, Q_1^2, Q_2^2) + \varepsilon\sigma_{LT}(W_{\gamma\gamma}, Q_1^2, Q_2^2). \tag{4.33}$$

Considering equation (4.33) the GVDM cross section becomes [31]

$$\sigma_{\gamma\gamma}^{GVDM}(W_{\gamma\gamma}, Q_1^2, Q_2^2) = \sigma_{\gamma\gamma}^{VMD}(W_{\gamma\gamma},0,0) \cdot F_{GVDM}(Q^2), \tag{4.34}$$

where

$$F_{GVDM}(Q^2) = F_T^{GVDM}(Q^2) + F_L^{GVDM}(Q^2) = \sum_{V=\rho,\omega,\phi} r_V \frac{1 + Q^2/4m_V^2}{\left(1 + Q^2/m_V^2\right)^2} + \frac{0.22}{1 + Q^2/m_0^2} \quad (4.35)$$

and $\sigma_{\gamma\gamma}^{VMD}(W_{\gamma\gamma},0,0)$ is the total cross section from equation (4.29).

In the single-tag case $\sigma_{\gamma\gamma}^{GVDM}$ from equation (4.34) becomes

$$\sigma_{\gamma\gamma}^{GVDM}(W_{\gamma\gamma}, Q_1^2, Q_2^2 \approx 0) = \sigma_{\gamma\gamma}^{VMD}(W_{\gamma\gamma},0,0) \cdot F_{GVDM}(Q_1^2). \quad (4.36)$$

The most widely used approximation for the hadron-like component of the structure function is when the photon is assumed to behave like a ρ meson. For a single ρ pole r_ρ=1. The weights for the other vector mesons and the continuum term are set to zero: r_ω=0, r_ϕ =0, r_C=0. Therefore, equations (4.31) and (4.32) become

$$F_T^\rho(Q^2) = \left(\frac{m_\rho^2}{Q^2 + m_\rho^2}\right)^2, \quad (4.37)$$

$$F_L^\rho(Q^2) = \left(\frac{m_\rho^2}{Q^2 + m_\rho^2}\right)^2 \frac{Q^2}{4m_\rho^2}. \quad (4.38)$$

4.4.3. The QCD Cross Section

QCD corrections are introduced via the DGLAP [33], [34], [35], [36] evolution equations. They necessitate the presence of the gluon and quark density in the photon. The dominant leading order QCD contributions for high Q^2 single-tag events are $\gamma q \to g\bar{q}$ and $\gamma g \to q\bar{q}$. Therefore, the QCD cross section can be parametrized as follows

$$\sigma^{QCD} = \int \left(f_g^{\gamma}(x,Q^2)\sigma(\gamma g \to q\bar{q}) + \sum_q f_q^{\gamma}(x,Q^2)\sigma(\gamma q \to qg) \right) dx dQ^2 . \quad (4.39)$$

Here, f_g^{γ} and f_q^{γ} are the gluon and quark density functions, also called parton density functions (pdf's) of the photon. These functions are the probabilities to find gluons and quarks with given momentum fraction x inside the target photon. This contribution is not perturbatively calculable and it has to be determined from experiment.

Large corrections in next-to-leading order leads to conclude that pdf's do not converge. This indicates that pdf's must be measured at a certain value of Q^2 and cannot be derived from calculations alone.

Many parametrizations exist for the pdf's of the photon. Some examples are: Cornet, Jankowski, and Krawczyk (CJK) [18], Drees and Grassi (DG) [33], Levy, Abromowicz, and Charchula (LAC) [37], Hagiwara, Tanaka, and Watanabe

(WHIT) [38], Glück, Reya, and Vogt (GRV) [39], (GS) Aurence, Guillet, and M. Fontannaz (AFG) [40], Gordon and Storrow(GS) [41], Glück, Reya, and Schienbein (GRSc) [42], and Schuler and Sjostrand (SaS) [43].

4.4.4. The Glück Reya Vogt (GRV) parametrization

The parton density functions are calculated in leading order (LO) and higher order (HO). With notations from [39], the photon parton distributions $f^{\gamma}(x,Q^2)$ are considered as the sum of a point-like and a hadronic contribution: $f^{\gamma} = f^{\gamma}_{PL} + f^{\gamma}_{had}$. The point-like contribution is perturbatively calculable. For the hadronic part the approximate similarity of the vector meson and the pion is used. The starting distribution is a hadron-like contribution based on VMD considerations. In order to avoid singularities in the low x region, the leading order (LO) and the higher order (HO) Q^2 evolution start with a valence-like input at $Q^2_{0,LO} = \mu^2_{LO} = 0.25\,GeV^2$ and $Q^2_{0,HO} = \mu^2_{HO} = 0.3\,GeV^2$, respectively. The functional form of the starting distribution, is $f^{\gamma} = q^{\gamma} = \bar{q}^{\gamma} = g^{\gamma} = \kappa \frac{4\pi\alpha}{f_{\rho}^2} f_{\pi}(x,Q_0^2)$, with $f_{\pi}(x,Q_0^2) \sim x^a(1-x)^b$, being the valence-like inputs taken from [44] and $f_{\rho}^2/4\pi \cong 2.2$ [14]. κ remains the only free parameter, which is obtained from the fits to the data [11], [45], [46], [47], [48], [49], [50], [51], [52], [53] on $F_2^{\gamma}(x,Q^2)$ in the Q^2 range $0.71 < Q^2 < 100\,GeV^2$ for $W_{\gamma\gamma} > 2$ to avoid resonance production.

The point-like contribution is chosen to vanish at $Q^2 = Q_0^2$. In this dissertation, due to the best agreement with data, the higher order parametrization HO is considered. The full evolution equations for "massless" quarks u, d, and s are used in the DIS_γ, i.e. "Deep Inelastic Scattering", factorization scheme [39] with Λ=0.248 (Section 1.2.2). The heavy quarks c (m_c=1.5 GeV), b (m_b = 4.5 GeV) are included via the lowest order Bethe-Heitler cross section formula (4.24).

Chapter 5

5. SIMULATION PROGRAMS

5.1. About Monte Carlo simulations in general

Monte Carlo programs are widely used simulation programs. They can provide approximate solutions to a variety of problems by performing statistical sampling calculations. With these programs we can calculate probabilities, but not definite outcomes.

At the generator level, MC's can be used to describe physical events, with exact trajectories, energies, momenta, and particle identification. Monte Carlo programs are also used to simulate detector effects. At the reconstruction level, generated events with information about four-momenta, energy, tracks, and other parameters are passed through the detector simulation. Interaction with the detector, magnetic field, and imperfections of the detection are also taken into account. The outcome is stored in the same format as the data.

Monte Carlo simulations are also helpful when data is insufficient to provide information about some events because of inaccessible kinematical

regions. They can also give an estimation for the background events that are subtracted from the data to be able to find the events that we want to use for our measurement. They play an essential role in determining the efficiency of detection and selection.

5.2. MC Simulation for two-photon processes

The value of the Q^2 variable is accurately determined by measuring the four-momentum of the scattered electron. However, the effective mass of the final state hadrons is only partially reconstructed, as these are often produced at low polar angles where no tracking system can be installed. A Monte Carlo modeling of the final state hadrons is therefore necessary [54] to determine the x variable. Three Monte Carlo generators are used to model the process $e^+e^- \to e^+e^-\text{hadrons}$: PHOJET [55], [56], PYTHIA [57] and TWOGAM [58].

The dominant backgrounds are evaluated with PYTHIA for $e^+e^- \to q\bar{q}(\gamma)$ and DIAG36 [59], [60] for $e^+e^- \to e^+e^-\tau^+\tau^-$. All Monte Carlo samples are generated with an integrated luminosity at least five times greater than the experimental one. All events are passed through a full detector simulation that uses the GEANT [61] and GHEISHA [62] programs and takes into account detector efficiencies and time-dependent effects. Monte Carlo events are then reconstructed in the same way as the data.

5.2.1. PHOJET

PHOJET describes hadron-hadron, photon-hadron and photon-photon collisions. It is based on the Dual Parton Model combined with the QCD-improved parton model [63]. In order to have a continuous transition between hard and soft processes (Section 4.2), the distribution of the transverse momentum, p_t, of the soft partons is matched to the one predicted by QCD. The two-photon luminosity is calculated from the flux of transversely polarized photons; corrections for the longitudinally polarized photons are incorporated into an effective two-photon cross section (Section 3.3). The transition from real-photon to virtual-photon scattering is obtained by a change of the relative weight of all partial cross sections.

5.2.2. PYTHIA

PYTHIA is a general purpose Monte Carlo. For two-photon interactions it incorporates leading order (LO) hard-scattering processes as well as elastic, diffractive, and low p_t events. The classification of the photon interactions into three different components, direct, resolved, and VDM, results in six different classes of events (Section 4.2.4). Events are also classified according to the hard scales involved in the process: photon virtualities (Q_i^2) and parton transverse momenta p_t.

5.2.3. TWOGAM

TWOGAM generates three different processes separately: point-like photon-photon interactions, resolved processes, and non-perturbative soft processes described by the Generalized Vector Dominance Model (Section 4.4.2). The structure of the program is modular and the photon flux is calculated with an exact LO formula. The cross sections of the three different processes are adjusted to fit the x distribution of the data. The adjustment ensures that the x-shape, used in the unfolding is similar to the data (Section 7.1). The cross section of the direct process is fixed to the expected value $\sigma_{QPM} = 41$ pb in the kinematical range $11\,\mathrm{GeV}^2 \le Q^2 \le 34\,\mathrm{GeV}^2$. The QCD and the VDM cross sections are then adjusted to $\sigma_{QCD} = 5$ pb and $\sigma_{VMD} = 28$ pb, respectively. The partial cross sections are calculated using the relation: $\sigma_{MC} = f_{MC} \cdot (N_{gen} / L_{MC})$. Here, f is the normalization factor (f_{QPM}=1, f_{QCD}=0.34, f_{VMD}=0.87) used to adjust the 3 MC contributions to the data. N_{gen} is the raw generated number of events and L_{MC} are the corresponding MC luminosities (Table 5.1). For the three Monte Carlo generators parton showering and hadronization are described by JETSET [64].

Sample	L(pb^{-1})	Generated number of events		
		11-14 GeV^2	14-20 GeV^2	20-34 GeV^2
1998 year				
QCD	2872.9	10913	14804	14941
QPM	996.4	11514	13996	14797
VMD	1619.9	17320	18172	16007
1999 (I) year				
QCD	2352.6	9214	12371	12618
QPM	822.6	9800	11748	12364
VMD	1120.0	12533	13140	11245
1999 (II) year				
QCD	2420.7	9848	13055	13448
QPM	830.9	10048	12087	12779
VMD	1161.6	13042	13830	11762
2000 year				
QCD	2978.0	12389	16946	16779
QPM	1117.0	13557	16641	17382
VMD	1204.0	13687	14520	12532

Table 5.1 Generated number of events and MC luminosities for the three TWOGAM contributions in three Q^2 ranges.

Chapter 6

6. DATA ANALYSIS

6.1. Trigger selection of single-tag events

As it was described in Section 2.4, L3 uses 3 trigger levels in order to extract interesting events for the data analysis. In the single-tag case, a final state electron is detected in the luminosity monitor. At level one, events are accepted by two independent triggers: the single-tag trigger and the central track-trigger. The single-tag trigger requires at least 70% of the beam energy to be deposited in one of the low polar-angle calorimeters, in coincidence with at least one track in the central tracking chamber. The central track-trigger (TEC) requires at least two tracks back-to-back in the transverse plane within $\pm 60^0$, each with $p_t > 150\ \mathrm{MeV}$.

6.2. Trigger efficiency

The combined efficiency of the two triggers is $\varepsilon_{trig} = (1-\overline{\varepsilon_1})\cdot(1-\overline{\varepsilon_2})$ $\cong 1-(\overline{\varepsilon_1}+\overline{\varepsilon_2}) \cong 97\%$, where $\overline{\varepsilon_1}$ and $\overline{\varepsilon_2}$ are the trigger inefficiencies for level 1 and level 2 trigger.

The trigger inefficiency for level 1 is: $\overline{\varepsilon_1} = \overline{\varepsilon_E} \cdot \overline{\varepsilon_{TEC}}$. The energy trigger inefficiency ($\overline{\varepsilon_E}$) for each bin is the ratio of the number of selected events with no energy trigger to the total number of selected events. The TEC trigger inefficiency $\overline{\varepsilon_{TEC}}$ for each bin is the ratio of the number of selected events with no TEC trigger to the total number of selected events.

Trigger level 2: In order to have a quick and efficient selection of the events, level 2 processes only 5 % of the events coming from level 1. If from these events we have N_{good} "good" events and $N_{rejected}$ is the number of events it is supposed to reject, then the total number of rejected events is $N_{rejected}^{tot} = 20 \cdot N_{rejected} = 20 \cdot (N_{selected} - N_{good})$. Therefore the trigger inefficiency for level 2 is $\overline{\varepsilon_2} = N_{rejected}^{tot} / N_{selected}$.

Trig level 3: The same procedure as for level 2 is applied. This time $N_{rejected} = 0$, the efficiency at level 3 is 100%.

6.3. Efficiency of the detection and selection

The efficiency of the detection and selection is the percentage of the events in a given kinematical range that are detected and kept after the selection cuts. It is given by the ratio between the number of reconstructed ("visible") Monte Carlo events after selection and the number of generated MC events in a defined

kinematical range: $\varepsilon = N_{vis}^{MC} / N_{gen}^{MC}$. Its value is sensitive to detector resolution and acceptance.

6.4. Selection cuts

Events are selected by requiring a single scattered electron in the low polar-angle calorimeter and a hadronic final state. A tagged electron candidate is the highest energy cluster with a shape consistent with an electromagnetic shower, $E_{tag}/E_{beam} > 0.7$, as shown in Figure 6.1 (a), and a polar angle in the fiducial region 0.0325 rad $\leq \theta \leq$ 0.0637 rad. To ensure that the virtuality of the target photon is small, the highest-energy cluster in the low polar-angle calorimeter opposite to the tagged electron must have an energy less than 20% of the beam energy, as shown in Figure 6.1 (b). The hadronic event selection requires at least four additional particles to be detected. A particle can be a track (in the chambers) or a photon (in the BGO). A track must have $p_t > 100$ MeV and a distance of closest approach to the interaction vertex in the transverse plane of less than 10 mm. A photon is a cluster in the electromagnetic BGO calorimeters with energy above 100 MeV not associated with a charged track.

The two-photon events are characterized by low energy deposition in the central detectors. To reduce the background from the $e^+e^- \rightarrow Z\gamma \rightarrow e^+e^-q\bar{q}(\gamma)$ process, the total energy deposited in the electromagnetic and hadronic calorimeters

must be less than 40% of the center-of-mass energy, as shown in Figure 6.1 (c). The events with a large value of the total energy are due to the $e^+e^- \to Z\gamma \to e^+e^-q\bar{q}(\gamma)$ process, where the radiative photon is misidentified as the tagged electron.

To avoid the hadronic resonance region, the mass of the hadronic final state, W_{vis}, calculated from all visible tracks and calorimetric clusters, is required to be greater than 4 GeV, as presented in Figure 6.1 (d). All distributions in Figure 6.1 (a), (b), (c), and (d) are presented after all other cuts are applied. The backgrounds from $e^+e^- \to Z\gamma \to e^+e^-q\bar{q}(\gamma)$ and $e^+e^- \to e^+e^-\tau^+\tau^-$ processes are indicated as shaded areas and added to the expectations of the PYTHIA, PHOJET and TWOGAM generators. The arrows indicate the position of the cuts.

For the analysis the data are grouped by $\sqrt{s}$. Figure 6.2 shows the Q^2 distribution for each $\sqrt{s}$ sample. On Figure 6.2 (a), for $\sqrt{s} = 189$ GeV the constraints on the tagging angle $(0.0325\,(\text{rad}) < \theta_{tag} < 0.0637\,(\text{rad}))$ and energy of the tagged electron $(0.7\,E_{beam} < E_{tag} < E_{beam})$ define the lower and upper limit for Q^2, $6\,\text{GeV}^2 < Q^2 < 35\,\text{GeV}^2$. This region was calculated using (3.6). For higher values of the beam energy these limits shift to higher values of Q^2. In order to avoid low efficiency regions, only events with $11\,\text{GeV}^2 \le Q^2 \le 34\,\text{GeV}^2$ are studied.

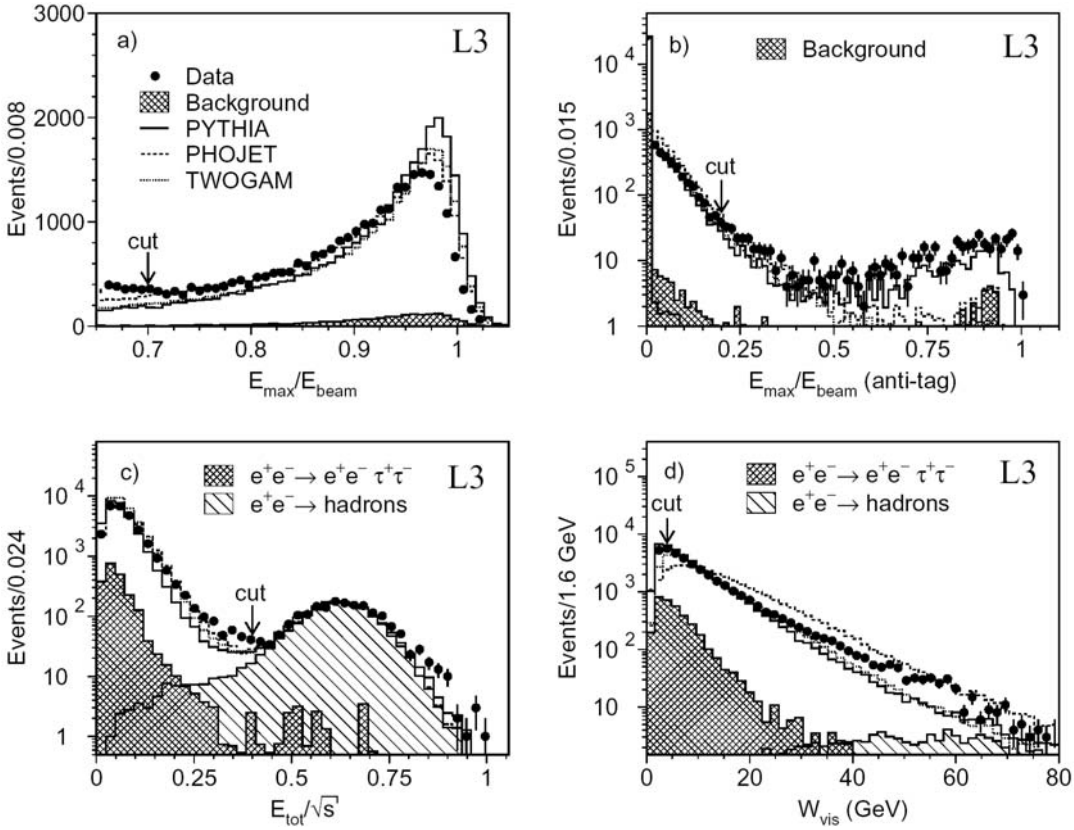

Figure 6.1 Distribution of the highest energy clusters in the forward electromagnetic calorimeters for a) the tagged electron side and b) for the opposite side. c) Total energy in the central calorimeters. d) The visible mass of the hadronic final state.

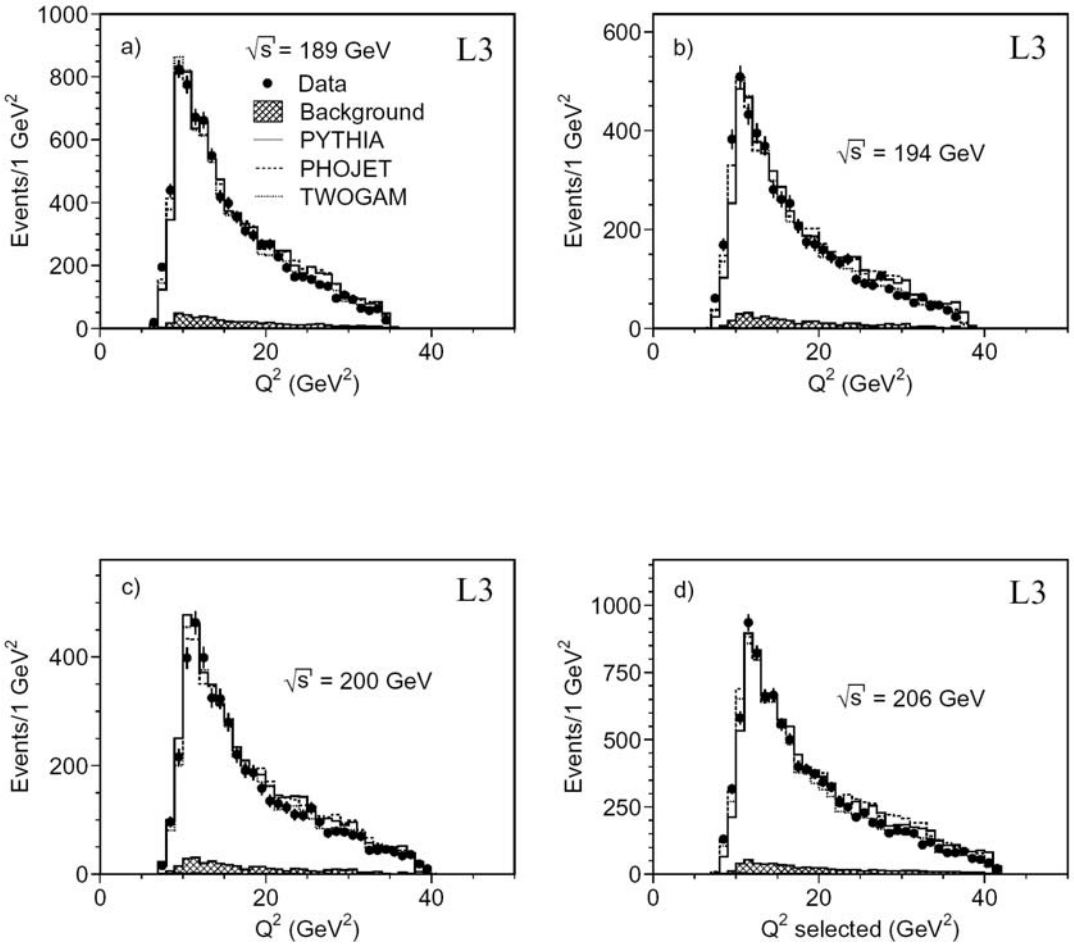

Figure 6.2 Q^2 distribution of the selected events for the four average $\sqrt{s}$ ranges.

The number of selected events and the backgrounds from the $e^+e^- \to e^+e^-\tau^+\tau^-$ and $e^+e^- \to Z\gamma \to e^+e^-q\bar{q}(\gamma)$ processes in the Q^2 intervals $11\,\mathrm{GeV}^2 \le Q^2 \le 14\,\mathrm{GeV}^2$, $14\,\mathrm{GeV}^2 \le Q^2 \le 20\,\mathrm{GeV}^2$ and $20\,\mathrm{GeV}^2 \le Q^2 \le 34\,\mathrm{GeV}^2$ are given in Table 6.1. The average e^+e^- center-of-mass energies, $<\sqrt{s}>$, and the corresponding luminosities for the four data samples together with the signal purity calculated as $(\text{data} - \text{background})/\text{data}$ are also listed. The background is dominated by the $e^+e^- \to e^+e^-\tau^+\tau^-$ production. The contribution from the $e^+e^- \to e^+e^-W^+W^-$ process is negligible. The background from beam-gas and beam-wall events is found to be negligible by inspection of the radial distribution of track intersections. The number of selected events and corresponding luminosities for data and simulated events in the three Q^2 ranges are given in Table 6.2. The visible mass W_{vis} and the $x_{vis} = Q^2/(Q^2 + W_{vis}^2)$ distributions are presented in Figure 6.3 for all selected data. The backgrounds from annihilation and two photon $\tau^+\tau^-$ events are indicated as shaded areas and added to the expectations of the PYTHIA, PHOJET and TWOGAM generators. The PYTHIA and TWOGAM model reproduce the data rather well, except at large values of W_{vis}. PHOJET presents a harder mass spectrum and predicts too many events for $x_{vis} < 0.1$ and is therefore not used in the following analysis steps. The total acceptance (Section 6.3) is calculated for each data sample separately. It takes into account the trigger efficiency, the geometrical acceptance, and the

$\langle\sqrt{s}\rangle$(GeV)	$\mathcal{L}$(pb^{-1})	Events	$e^+e^- \to e^+e^-\tau^+\tau^-$	$e^+e^- \to q\bar{q}(\gamma)$	Purity (%)
$Q^2 = 11 - 14$ GeV^2					
189	171.8	1884	107.6	5.7	94
194	111.4	1197	76.3	3.3	93
200	109.3	1187	74.9	3.7	93
206	215.6	2418	129.6	7.7	94
$Q^2 = 14 - 20$ GeV^2					
189	171.8	2046	128.6	9.7	93
194	111.4	1347	91.2	5.4	93
200	109.3	1359	89.5	4.9	93
206	215.6	2886	177.4	8.7	94
$Q^2 = 20 - 34$ GeV^2					
189	171.8	1922	143.9	8.1	92
194	111.4	1331	103.6	5.8	92
200	109.3	1287	101.6	6.7	92
206	215.6	2859	202.5	12.7	92

Table 6.1 Selected events and the backgrounds from $e^+e^- \to e^+e^-\tau^+\tau^-$ and $e^+e^- \to Z\gamma \to e^+e^-q\bar{q}(\gamma)$ processes.

Sample	L(pb^{-1})	$\langle\sqrt{s}\rangle$(GeV)	Selected number of events		
			11-14 GeV^2	14-20 GeV^2	20-34 GeV^2
1998 year					
Data	171.8	189	1884	2046	1922
TWOGAM	5489.1	189	20667	23791	22403
PHOJET	2807.4	189	13469	15497	16997
PYTHIA	318.2	189	6031	6968	7507
1999 (I) year					
Data	111.4	194	1197	1347	1331
TWOGAM	4264.4	196	16544	19389	18316
PHOJET	1817.4	196	8444	10174	11475
PYTHIA	456.4	197	7770	9251	9898
1999 (II) year					
Data	109.3	200	1187	1359	1287
TWOGAM	4390.4	200	17172	20212	19659
PHOJET	1818.1	200	8468	10624	11730
PYTHIA	456.4	197	7770	9251	9898
2000 year					
Data	215.6	206	2418	2886	2859
TWOGAM	5298.5	204	20429	25239	24618
PHOJET	1754.3	204	8525	10602	12766
PYTHIA	453.3	206	8674	10820	11729

Table 6.2 The number of selected events and the luminosity in the data and simulated samples in the three Q^2 ranges.

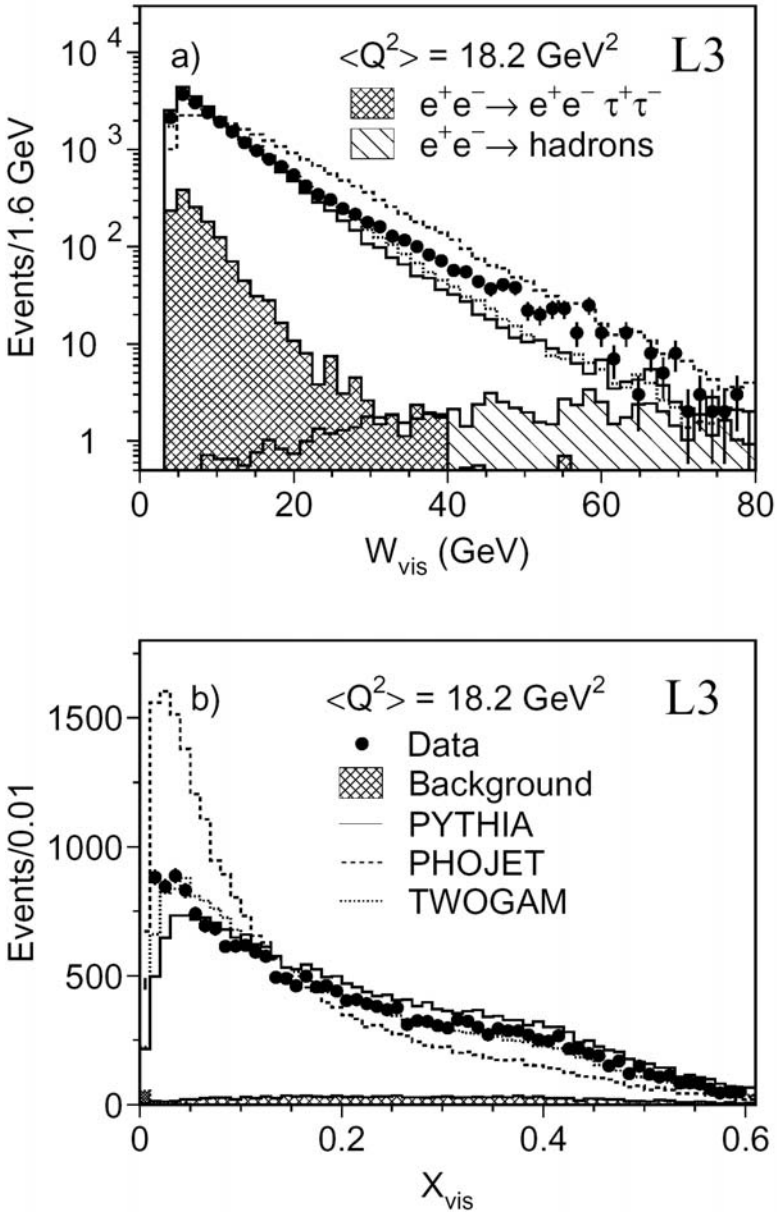

Figure 6.3 Distribution of the visible mass of the two-photon system and of x_{vis} for all selected events compared with Monte Carlo predictions for signal and backgrounds.

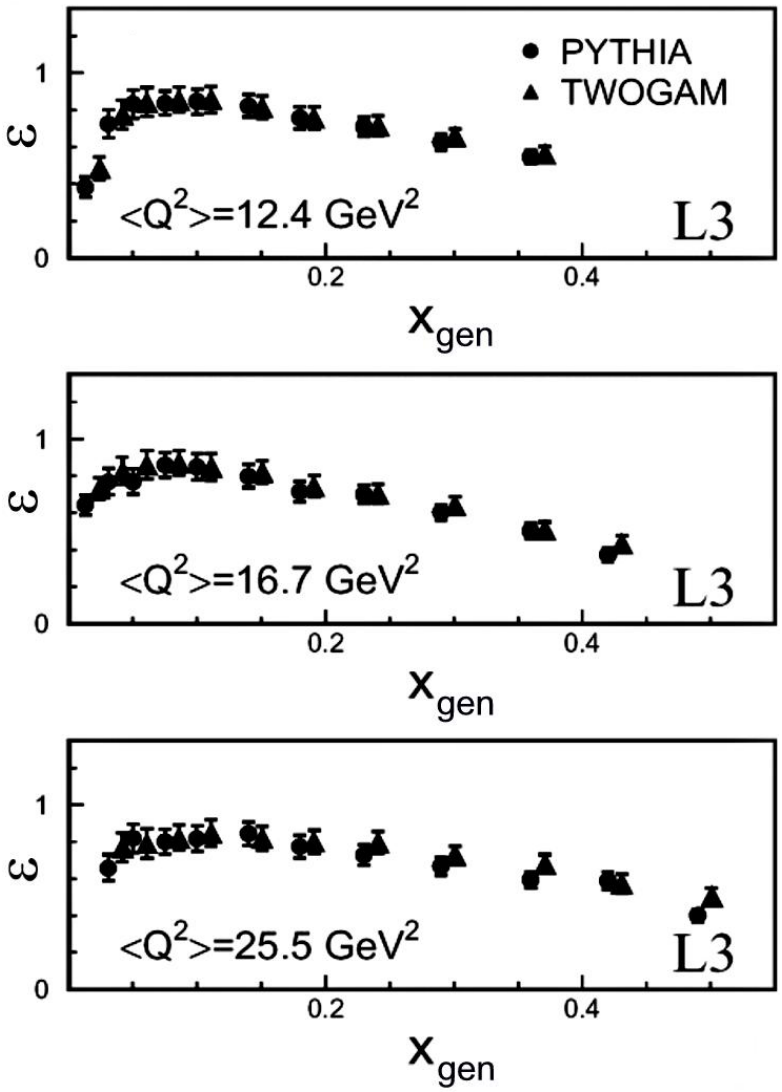

Figure 6.4 The detector acceptance and selection efficiency, ε, obtained by the PYTHIA and TWOGAM generators.

selection cuts. An example is presented in Figure 6.4 for the data at $\sqrt{s} = 189$ GeV. For clarity, the symbols corresponding to the two Monte Carlo generators are slightly offset. The decreasing tendency of ε at low and high Q^2 shows that we are loosing events at bigger and higher angles (3.6).

Chapter 7

7. RESULTS

7.1. Unfolding

In the $e^+e^- \rightarrow e^+e^-\gamma^*\gamma^{(*)} \rightarrow e^+e^-$ hadrons deep inelastic scattering process the energy of the quasi-real target photon is not known. The kinematics cannot be fully determined without measuring the hadronic final state, which is only partially observed in the detector. This leads to a dependence of the F_2^γ measurement on Monte Carlo modeling (Section 5.2) of the hadronic final state. This dependence enters when an unfolding procedure is used to relate the visible distorted $x_{vis} = Q^2/\left(Q^2 + W_{vis}^2\right)$ distribution to the true unfolded x_{unf} distribution. This analysis concentrates on measuring F_2^γ as a function of x and Q^2 variables. Q^2 is entirely determined by the tagged electron's angle and energy, and is precisely measured. The following example shows the limited acceptance of the hadrons in the detectors. In Figure 7.1 x_{vis}^{MC} is the visible distribution from a MC simulation after reconstruction and x_{gen} is the originally generated distribution.

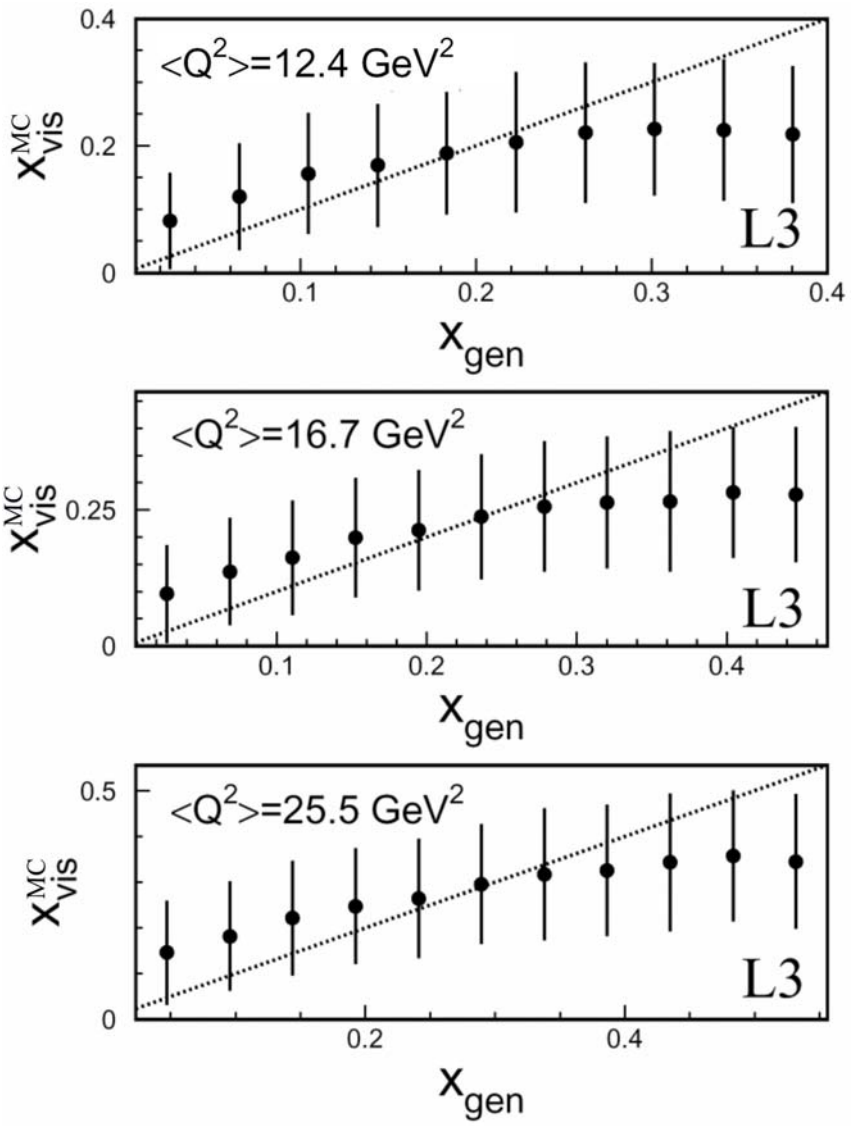

Figure 7.1 Comparison of the measured and generated value of x for the PYTHIA Monte Carlo at $\sqrt{s} = 189\,\mathrm{GeV}$ for different values of Q^2.

The mean observed value and the standard deviation of x_{vis}^{MC} are plotted for events generated in a given x_{gen} bin.

A matrix A can be constructed which relates the reconstructed distribution from the MC simulation x_{vis}^{MC} to the generated distribution x_{gen}

$$N(x_{vis}^{MC} \mid x_{gen}) = A \cdot N(x_{gen}). \tag{7.1}$$

The matrix elements A_{ij} can be calculated using the relation

$$A_{ij} = \left(\frac{N(x_{vis,i}^{MC} \mid x_{gen,j})}{N(x_{gen,j})} \right). \tag{7.2}$$

In this equation $N(x_{gen,j})$ is the total number of events generated, i.e. "causes" ($j = 1,2,\ldots n_c$), in bin j and $N(x_{vis,i}^{MC} \mid x_{gen,j})$ is the number of measured MC events, i.e. "effects" ($i = 1, 2,\ldots n_E$), in bin i and generated in bin j. Usually, the sum of the effects $N(x_{vis,i}^{MC} \mid x_{gen,j})$ caused by $N(x_{gen,j})$ are not equal to the number of generated events $N(x_{gen,j})$:

$$N(x_{vis}^{MC} \mid x_{gen,j}) = \sum_{i=1}^{n_E} N(x_{vis,i}^{MC} \mid x_{gen,j}) \leq N(x_{gen,j}). \tag{7.3}$$

This means that it is not necessary for each cause to produce an effect. The efficiency of detecting the cause $x_{gen,j}$ in any of the possible effects is

$$\varepsilon_j^0 = \sum_{i=1}^{n_E} A_{ij} = \frac{N(x_{vis}^{MC} \mid x_{gen,j})}{N(x_{gen,j})}, \tag{7.4}$$

where $0 < \varepsilon_j^0 \leq 1$. From here on the index zero indicates the use of an MC input. The detector-response matrix A reflects the acceptance and efficiency of the detector. If $\varepsilon_j^0 = 1$, then the response of the experiment will be perfect.

To relate the true unfolded distribution x_{unf} to the experimentally measured distribution seems to be simply

$$N(x_{unf} \mid x_{gen}) = A^{-1} N(x_{vis}). \tag{7.5}$$

However, this inverse matrix A^{-1} can lead to unphysical negative values of the unfolded x_{unf} distribution. The example below shows the elements of a two-dimensional matrix [66], [67]

$$A = \frac{1}{2}\begin{pmatrix} 1+\varepsilon & 1-\varepsilon \\ 1-\varepsilon & 1+\varepsilon \end{pmatrix}, \tag{7.6}$$

where the value ε is a measure of how well these 2 bins are separated.

For $\varepsilon \neq 0$ the inverse matrix becomes

$$A^{-1} = \frac{1}{2\varepsilon}\begin{pmatrix} 1+\varepsilon & -1+\varepsilon \\ -1+\varepsilon & 1+\varepsilon \end{pmatrix}. \tag{7.7}$$

Therefore,

$$N(x_{unf} \mid x_{gen,j}) = \frac{1}{2\varepsilon}\begin{pmatrix} 1+\varepsilon & -1+\varepsilon \\ -1+\varepsilon & 1+\varepsilon \end{pmatrix}\begin{pmatrix} N(x_{vis,1}) \\ N(x_{vis,2}) \end{pmatrix}. \tag{7.8}$$

Equation (7.8) can be rewritten as

$$N(x_{unf} \mid x_{gen,j}) = \frac{N(x_{vis,1}) - N(x_{vis,2})}{2\varepsilon}\begin{pmatrix} 1 \\ -1 \end{pmatrix} + \frac{N(x_{vis,1}) + N(x_{vis,2})}{2}\begin{pmatrix} 1 \\ 1 \end{pmatrix}. \tag{7.9}$$

If the uncertainties in x_{vis} are too large

$$| N(x_{vis,1}) - N(x_{vis,2}) | < \sqrt{(\Delta N(x_{vis,1}))^2 + (\Delta N(x_{vis,2}))^2} \tag{7.10}$$

the first term in equation (7.9) can become a random number, causing also $N(x_{unf} \mid x_{gen,j})$ to become random. If the events are split into bins that cannot be distinguished by the detector (for small value of $\varepsilon \neq 0$), the elements of the matrix will start to oscillate between large negative and large positive numbers causing the result to become unphysical. To solve this problem of oscillating unfolded distributions the Bayesian unfolding procedure [65] is used.

Unfolding of the measured distribution can be obtained as follows

$$N(x_{unf} \mid x_{gen,j}) = \frac{1}{\varepsilon_j} \sum_{i=1}^{n_E} P(x_{gen,j} \mid x_{vis,i}^{MC}) N(x_{vis,i}) = \frac{N(x_{vis} \mid x_{gen,j})}{\varepsilon_j}, \qquad (7.11)$$

where $N(x_{unf} \mid x_{gen,j})$ is the number of unfolded events assignable to each of the causes, $N(x_{vis})$ is the number of experimentally observed events, and $N(x_{vis} \mid x_{gen,j})$ is the expected number of events assigned to each of the causes and only due to the observed events. Here both "unfolded" and "observed" refer to data. If ε_j is zero, then $N(x_{vis} \mid x_{gen,j})$ becomes also zero, which means that the experiment is not sensitive to the causes, i.e. "generated events". $\varepsilon_j = \frac{N(x_{vis} \mid x_{gen,j})}{N(x_{unf} \mid x_{gen,j})}$ can differ from the a-priori efficiency ε_j^0:

$$\varepsilon_j^0 = \frac{N(x_{vis}^{MC} \mid x_{gen,j})}{N(x_{gen,j})}. \tag{7.12}$$

The sum of ε_j^0 can be written as

$$\varepsilon^0 = \sum_{j=1}^{n_c} \varepsilon_j^0 = \frac{\sum_{j=1}^{n_c} \varepsilon_j P^0(x_{gen,j})}{\sum_{j=1}^{n_c} P^0(x_{gen,j})}, \tag{7.13}$$

where $P^0(x_{gen,j})$ is the initial probability of the causes

$$P^0(x_{gen,j}) = \frac{N(x_{gen,j})}{\sum_{j=1}^{n_c} N(x_{gen,j})}. \tag{7.14}$$

The initial probability for any cause to occur must be $\sum_{j=1}^{n_c} P^0(x_{gen,j}) = 1$. The conditional probabilities $P(x_{gen,j} \mid x_{vis,i}^{MC})$, i.e. "smearing matrix" S_{ji}^0, from equation (7.11) can be calculated using the relation

$$S_{ji}^0 = P(x_{gen,j} \mid x_{vis,i}^{MC}) = \frac{P(x_{vis,i}^{MC} \mid x_{gen,j}) P^0(x_{gen,j})}{\sum_{l=1}^{n_c} P(x_{vis,i}^{MC} \mid x_{gen,l}) P^0(x_{gen,l})}, \tag{7.15}$$

where $P(x_{vis,i} \mid x_{gen,j})$ is the likelihood of observing the measured x_{vis} given a generated x_{gen} value. From the above equation it follows that for $\sum_{j=1}^{n_c} S_{ji}^{0} = 1$ each observed event must come from one of the causes.

The total probability distribution $P(x_{gen,j})$ is obtained performing an iterative calculation by replacing $N(x_{gen,j})$ with $N(x_{unf} \mid x_{gen,j})$ in equation (7.14).

The unfolding is performed as follows:

1. Start with $P^0(x_{gen,j})$ from equation (7.14) and $N^0(x_{vis} \mid x_{gen,j}) = P^0(x_{gen,j}) \cdot N(x_{vis} \mid x_{gen,j})$ using the inputs from data $N(x_{vis})$, and from Monte Carlo $N(x_{gen,i})$.
2. Calculate the smearing matrix from equation (7.15).
3. Calculate $N(x_{unf} \mid x_{gen,j})$ from (7.11) and $P(x_{gen,j}) = \frac{N(x_{unf} \mid x_{gen,j})}{\sum_{j=1}^{n_c} N(x_{unf} \mid x_{gen,j})}$.
4. Perform a χ^2 comparison between $N(x_{unf} \mid x_{gen,j})$ and $N^0(x_{vis} \mid x_{gen,j})$.
5. If χ^2 large, then replace $N^0(x_{vis} \mid x_{gen,j})$ with $N(x_{unf} \mid x_{gen,j})$ and $P^0(x_{gen,j})$ with $P(x_{gen,j})$. Otherwise, go to step 2.

Since after each iteration we get closer to the true distribution the agreement between $P^0(x_{gen,j})$ and $P(x_{gen,j})$ becomes better.

After a large number of iterations the unfolded distribution starts oscillating. To avoid this, one has to choose an optimum number of iterations. This procedure is called “regularization”.

In this analysis a “one-step” unfolding program was used. Assuming that the Monte Carlo program gives a valid description of the probability distribution of the data, one can omit the iteration steps. The result will be sensitive to the MC model. The initial probability $P^0=1$ is considered and the smearing matrix is calculated using (7.15). An example of the correlation matrix (7.15) for the simulated measured x_{vis}^{MC} vs. generated x_{gen} is shown in Table 7.1.

After unfolding, the events $N(x_{unf})$ are corrected for detector acceptance and efficiency ε_j^0 using the ratio between the number of measured selected MC events and the generated MC events for each j bin (7.12). This includes geometrical effects and inefficiencies of the detector and the analysis.

7.2. Measured Differential Cross Sections

The measured cross section $\Delta\sigma_{ee}/\Delta x$ as a function of x for the reaction $e^+e^- \to e^+e^-$ hadrons is measured for three Q^2 intervals: $11\,\mathrm{GeV}^2 \le Q^2 \le 14\,\mathrm{GeV}^2$, $14\,\mathrm{GeV}^2 \le Q^2 \le 20\,\mathrm{GeV}^2$, and $20\,\mathrm{GeV}^2 \le Q^2 \le 34\,\mathrm{GeV}^2$. Each data set is subdivided into bins of x_{vis} of similar statistics, as listed in Table 7.2.

	$Q^2 = 11 - 14$ GeV^2									
x range	0.006 – 0.023	0.023 – 0.040	0.040 – 0.060	0.060 – 0.090	0.090 – 0.120	0.120 – 0.160	0.160 – 0.205	0.205 – 0.260	0.260 – 0.330	0.330 – 0.400
0.006 – 0.023	1.00									
0.023 – 0.040	0.92	1.00								
0.040 – 0.060	0.75	0.92	1.00							
0.060 – 0.090	0.55	0.79	0.96	1.00						
0.090 – 0.120	0.45	0.67	0.85	0.94	1.00					
0.120 – 0.160	0.39	0.62	0.78	0.89	0.98	1.00				
0.160 – 0.205	0.28	0.50	0.67	0.80	0.95	0.97	1.00			
0.205 – 0.260	0.25	0.45	0.59	0.69	0.84	0.87	0.94	1.00		
0.260 – 0.330	0.22	0.38	0.49	0.59	0.79	0.82	0.91	0.99	1.00	
0.330 – 0.400	0.17	0.36	0.50	0.60	0.77	0.78	0.86	0.98	0.97	1.00

	$Q^2 = 14 - 20$ GeV^2										
x range	0.006 – 0.023	0.023 – 0.040	0.040 – 0.060	0.060 – 0.090	0.090 – 0.120	0.120 – 0.160	0.160 – 0.205	0.205 – 0.260	0.260 – 0.330	0.330 – 0.400	0.400 – 0.467
0.006 – 0.023	1.00										
0.023 – 0.040	0.87	1.00									
0.040 – 0.060	0.74	0.95	1.00								
0.060 – 0.090	0.55	0.82	0.93	1.00							
0.090 – 0.120	0.54	0.79	0.89	0.98	1.00						
0.120 – 0.160	0.36	0.63	0.73	0.89	0.93	1.00					
0.160 – 0.205	0.31	0.60	0.71	0.85	0.89	0.98	1.00				
0.205 – 0.260	0.24	0.49	0.59	0.75	0.81	0.95	0.95	1.00			
0.260 – 0.330	0.18	0.40	0.50	0.64	0.71	0.87	0.88	0.97	1.00		
0.330 – 0.400	0.21	0.40	0.47	0.56	0.65	0.79	0.79	0.91	0.97	1.00	
0.400 – 0.467	0.11	0.31	0.37	0.47	0.55	0.71	0.71	0.84	0.91	0.96	1.00

	$Q^2 = 20 - 34$ GeV^2										
x range	0.023 – 0.040	0.040 – 0.060	0.060 – 0.090	0.090 – 0.120	0.120 – 0.160	0.160 – 0.205	0.205 – 0.260	0.260 – 0.330	0.330 – 0.400	0.400 – 0.467	0.467 – 0.556
0.023 – 0.040	1.00										
0.040 – 0.060	0.92	1.00									
0.060 – 0.090	0.87	0.96	1.00								
0.090 – 0.120	0.80	0.88	0.97	1.00							
0.120 – 0.160	0.66	0.75	0.89	0.96	1.00						
0.160 – 0.205	0.62	0.71	0.82	0.91	0.97	1.00					
0.205 – 0.260	0.58	0.64	0.76	0.86	0.93	0.98	1.00				
0.260 – 0.330	0.47	0.54	0.66	0.77	0.88	0.95	0.97	1.00			
0.330 – 0.400	0.43	0.49	0.61	0.71	0.81	0.88	0.92	0.97	1.00		
0.400 – 0.467	0.38	0.45	0.55	0.63	0.73	0.78	0.83	0.91	0.98	1.00	
0.467 – 0.556	0.39	0.44	0.54	0.63	0.73	0.78	0.84	0.91	0.98	0.99	1.00

Table 7.1 Correlation matrices of x_{vis} vs. x_{gen} obtained with the PYTHIA Monte Carlo for the data at $\sqrt{s} = 189$ GeV for the three Q^2 intervals.

$\langle\sqrt{s}\rangle$		189 GeV	194 GeV	200 GeV	206 GeV
$Q^2 = 11 - 14$ GeV^2					
Δx range	$\langle x \rangle$	$\Delta\sigma/\Delta x$ (pb)	$\Delta\sigma/\Delta x$ (pb)	$\Delta\sigma/\Delta x$ (pb)	$\Delta\sigma/\Delta x$ (pb)
$0.006 - 0.023$	0.013	$103.6 \pm 8.5 \pm 14.5$	$108.2 \pm 10.8 \pm 15.4$	$106.4 \pm 10.2 \pm 10.4$	$115.3 \pm 7.8 \pm 16.4$
$0.023 - 0.040$	0.031	$63.4 \pm 5.3 \pm 4.3$	$67.0 \pm 6.5 \pm 8.4$	$63.9 \pm 6.3 \pm 5.2$	$69.6 \pm 4.5 \pm 7.7$
$0.040 - 0.060$	0.050	$52.0 \pm 4.0 \pm 2.9$	$55.7 \pm 5.1 \pm 7.8$	$53.4 \pm 5.5 \pm 5.3$	$52.0 \pm 3.6 \pm 5.4$
$0.060 - 0.090$	0.075	$45.0 \pm 3.4 \pm 2.2$	$47.7 \pm 4.4 \pm 6.1$	$44.0 \pm 4.0 \pm 4.4$	$43.8 \pm 2.8 \pm 5.3$
$0.090 - 0.120$	0.100	$40.2 \pm 2.9 \pm 1.8$	$40.8 \pm 3.9 \pm 5.3$	$39.3 \pm 3.6 \pm 4.3$	$39.6 \pm 2.8 \pm 5.1$
$0.120 - 0.160$	0.140	$37.9 \pm 2.8 \pm 2.3$	$37.4 \pm 3.4 \pm 5.3$	$36.9 \pm 3.4 \pm 4.2$	$37.9 \pm 2.5 \pm 4.4$
$0.160 - 0.205$	0.180	$34.8 \pm 2.5 \pm 1.3$	$33.9 \pm 2.9 \pm 4.7$	$33.0 \pm 2.9 \pm 4.3$	$35.8 \pm 2.4 \pm 4.3$
$0.205 - 0.260$	0.230	$33.3 \pm 2.4 \pm 1.3$	$31.9 \pm 3.1 \pm 4.8$	$31.6 \pm 2.8 \pm 4.0$	$32.6 \pm 2.0 \pm 4.4$
$0.260 - 0.330$	0.290	$29.8 \pm 2.1 \pm 1.7$	$29.1 \pm 2.9 \pm 4.0$	$28.3 \pm 2.7 \pm 3.7$	$30.7 \pm 1.9 \pm 4.4$
$0.330 - 0.400$	0.360	$29.9 \pm 2.1 \pm 1.3$	$27.5 \pm 2.7 \pm 4.0$	$25.5 \pm 2.6 \pm 3.8$	$29.5 \pm 1.8 \pm 3.9$
$Q^2 = 14 - 20$ GeV^2					
$0.006 - 0.023$	0.013	$97.0 \pm 8.5 \pm 12.7$	$100.4 \pm 10.2 \pm 9.8$	$102.4 \pm 10.4 \pm 11.1$	$113.0 \pm 7.7 \pm 11.5$
$0.023 - 0.040$	0.031	$59.3 \pm 4.9 \pm 3.6$	$64.0 \pm 6.5 \pm 4.9$	$64.2 \pm 7.1 \pm 6.2$	$72.2 \pm 5.2 \pm 7.8$
$0.040 - 0.060$	0.050	$49.6 \pm 4.3 \pm 5.7$	$50.8 \pm 5.2 \pm 5.0$	$53.4 \pm 5.3 \pm 4.3$	$55.8 \pm 3.6 \pm 2.7$
$0.060 - 0.090$	0.075	$40.8 \pm 2.9 \pm 1.7$	$42.5 \pm 3.9 \pm 1.9$	$44.5 \pm 4.2 \pm 2.6$	$47.8 \pm 2.9 \pm 3.1$
$0.090 - 0.120$	0.100	$36.1 \pm 2.9 \pm 1.9$	$38.0 \pm 3.6 \pm 2.3$	$37.9 \pm 3.6 \pm 3.2$	$41.5 \pm 2.4 \pm 2.0$
$0.120 - 0.160$	0.140	$32.5 \pm 2.2 \pm 1.5$	$35.7 \pm 3.0 \pm 1.6$	$36.7 \pm 3.3 \pm 2.1$	$37.7 \pm 2.3 \pm 1.7$
$0.160 - 0.205$	0.180	$31.8 \pm 2.3 \pm 1.3$	$31.9 \pm 2.7 \pm 1.7$	$33.3 \pm 3.0 \pm 1.7$	$34.7 \pm 2.2 \pm 1.5$
$0.205 - 0.260$	0.230	$30.8 \pm 2.1 \pm 1.0$	$30.6 \pm 2.8 \pm 1.3$	$32.2 \pm 2.8 \pm 1.8$	$34.4 \pm 2.0 \pm 1.5$
$0.260 - 0.330$	0.290	$27.7 \pm 2.0 \pm 1.0$	$27.6 \pm 2.3 \pm 1.2$	$30.0 \pm 2.3 \pm 1.7$	$31.2 \pm 1.9 \pm 1.2$
$0.330 - 0.400$	0.360	$28.1 \pm 2.1 \pm 1.1$	$26.8 \pm 2.4 \pm 1.3$	$29.4 \pm 2.8 \pm 1.3$	$29.0 \pm 1.9 \pm 1.0$
$0.400 - 0.467$	0.430	$26.7 \pm 2.1 \pm 2.1$	$25.2 \pm 2.5 \pm 1.8$	$26.8 \pm 2.7 \pm 1.7$	$27.8 \pm 1.9 \pm 1.1$
$Q^2 = 20 - 34$ GeV^2					
$0.023 - 0.040$	0.031	$48.6 \pm 5.4 \pm 3.6$	$54.3 \pm 6.5 \pm 3.3$	$37.4 \pm 3.6 \pm 2.4$	$39.5 \pm 2.6 \pm 2.0$
$0.040 - 0.060$	0.050	$41.9 \pm 4.1 \pm 4.1$	$36.0 \pm 3.4 \pm 2.4$	$37.4 \pm 3.6 \pm 2.4$	$39.5 \pm 2.6 \pm 2.0$
$0.060 - 0.090$	0.075	$35.8 \pm 2.8 \pm 1.7$	$36.0 \pm 3.4 \pm 2.4$	$37.4 \pm 3.6 \pm 2.4$	$39.5 \pm 2.6 \pm 2.0$
$0.090 - 0.120$	0.100	$32.8 \pm 2.7 \pm 2.2$	$32.1 \pm 3.3 \pm 1.4$	$32.4 \pm 3.3 \pm 1.9$	$36.3 \pm 2.6 \pm 1.3$
$0.120 - 0.160$	0.140	$29.1 \pm 2.5 \pm 1.7$	$30.6 \pm 2.8 \pm 2.4$	$32.1 \pm 3.0 \pm 2.5$	$33.6 \pm 2.2 \pm 1.2$
$0.160 - 0.205$	0.180	$27.7 \pm 2.1 \pm 1.1$	$28.1 \pm 2.6 \pm 1.1$	$28.6 \pm 2.6 \pm 1.7$	$32.2 \pm 2.0 \pm 1.2$
$0.205 - 0.260$	0.230	$25.0 \pm 1.7 \pm 1.0$	$24.2 \pm 2.0 \pm 1.0$	$25.0 \pm 2.2 \pm 1.3$	$27.4 \pm 1.6 \pm 1.2$
$0.260 - 0.330$	0.290	$25.0 \pm 1.7 \pm 1.0$	$24.2 \pm 2.0 \pm 1.0$	$25.0 \pm 2.2 \pm 1.3$	$27.4 \pm 1.6 \pm 1.2$
$0.330 - 0.400$	0.360	$24.5 \pm 1.8 \pm 1.2$	$23.3 \pm 2.2 \pm 1.0$	$24.3 \pm 2.2 \pm 1.4$	$25.6 \pm 1.6 \pm 0.9$
$0.400 - 0.467$	0.430	$23.6 \pm 1.8 \pm 1.5$	$22.4 \pm 2.0 \pm 1.1$	$23.5 \pm 2.4 \pm 1.2$	$24.5 \pm 1.7 \pm 1.0$
$0.467 - 0.556$	0.490	$22.8 \pm 1.6 \pm 2.5$	$22.4 \pm 2.1 \pm 2.9$	$24.0 \pm 2.3 \pm 2.3$	$24.5 \pm 1.5 \pm 1.5$

Table 7.2 Cross sections $\Delta\sigma_{ee} / \Delta x$ as a function of x for the reaction $e^+e^- \rightarrow e^+e^-$ hadrons for the four average values of $\sqrt{s}$, in three Q^2 intervals.

The first uncertainty is statistical, the second systematic. The average values of the cross sections obtained with the PYTHIA and TWOGAM generators are used. The correlation between x_{gen} and x_{vis}^{MC} is similar for the two models. The one obtained with PYTHIA is shown in Figure 7.1. The measured cross sections for each value of $\sqrt{s}$ are given in Table 7.2 with their statistical and systematic uncertainties. $\Delta\sigma_{ee}$ is calculated using the relation: $\Delta\sigma_{ee} = N_{unf} / (\varepsilon_{trig} \cdot \varepsilon \cdot L)$, where N_{unf} is the number of unfolded events, ε_{trig} is the trigger efficiency, ε is the efficiency of the detection and selection, and L is the integrated beam luminosity.

7.3. Systematic Uncertainties

The systematic uncertainties on the cross sections are estimated for each data sample, for each x bin, and for each Q^2 interval. Three main sources of systematic uncertainties are considered: the selection procedure, the trigger efficiency, and the Monte Carlo model. Their effects are listed in Table 7.3. For small variations of the uncertainties in the different x bins an average was calculated, otherwise, a range was given. The examples from this table show also the extreme cases where the uncertainties reach the lowest and highest values in the given kinematical range. The uncertainties from the selection procedure are estimated by varying the selection cuts. The fiducial value of the polar angle in the low polar-angle calorimeter is varied from 0.0325 rad to 0.0360 rad and from

0.0637 rad to 0.060 rad. These changes result in a Q^2-dependent uncertainty, as the highest and lowest values of the Q^2 are affected by the fiducial cut (3.6). Figure 6.2 shows that due to the shift of the Q^2 distribution to higher values the lower Q^2 bins become low efficiency regions. This is especially the case for the 189 GeV data set. This can result in a difference of up to 10 % in the uncertainties from one data set to another. Due to this large difference the uncertainties are given as a range of values. The cut on E_{tag}/E_{beam} is varied from 0.70 to 0.65 and 0.75. The uncertainty on the tagging calorimeter energy cut can have variations of up to 1.4 % from one data set to another. This change is smaller within the different x and Q^2 bins. The anti-tag cut is changed from 0.20 to 0.15 and 0.25 E_{max}/E_{beam}. The uncertainty on this cut changes by about 0.1% from one x bin and Q^2 range to another, and also comparing the different data sets. Therefore, an average was calculated. The numbers of particles is varied from four to three and five. The uncertainty on this cut can change by 2.2 % from one data set to another. The cut on the total energy in the calorimeters relative to $\sqrt{s}$ is varied from 0.40 to 0.35 and 0.45. The change in the uncertainty for this cut can be up to 0.3% from one Q^2 range to another. Negligible changes were observed within the x bins and from one data set to another. A variation by up to 1.4 % of the uncertainty on the trigger efficiency (Section 6.2) was observed from one Q^2 range to another. The change in the uncertainty due Monte Carlo statistics is up to 5.5%. This uncertainty is calculated using the relation $\sqrt{N(x_{gen}) - N(x_{vis}^{MC}) / N(x_{vis}^{MC}) \cdot N(x_{gen})}$, where $N(x_{vis}^{MC})$

		1998 Q^2=11-14 (GeV^2)	**2000** Q^2=11-14 (GeV^2)	**1998** Q^2=20-34 (GeV^2)	**2000** Q^2=20-34 (GeV^2)
	Uncertainty range %	x = 0.006-0.400	x = 0.006-0.400	x = 0.023-0.467	x = 0.023-0.467
		Average uncertainty for the x intervals			
Tagging calorimeter polar angle	0.7-10.2	**0.7**	**10.2**	0.7	0.8
Tagging calorimeter energy	1.8-3.2	2.5	**3.2**	**1.8**	1.5
Anti-tag energy	0.4	0.4	0.3	0.4	0.4
Number of particles	1.4-3.6	**1.4**	**3.6**	2.0	1.9
Total energy in the calorimeters	0.1-0.4	**0.1**	0.1	**0.4**	0.3
		1999(II)	**2000**	**1999(II)**	**2000**
Trigger efficiency	0.8-2.6	1.3	**1.1**	**2.5**	2.2
		Uncertainty range for the x intervals			
		1999(I)	**2000**	**1999(I)**	**2000**
Monte Carlo Statistics	2.1-7.6	3.2-**7.6**	2.3.-5.3	3.2-7.0	**2.1**-4.5
		1998	**2000**	**1998**	**2000**
Model dependence	0.1-12.9	1.1-**12.9**	0.7-10.6	0.4-10.7	**0.1**-5.5

Table 7.3 Systematic uncertainties on the measured cross sections.

is the number of reconstructed Monte Carlo events after selection and $N(x_{gen})$ is the number of generated MC events in a defined kinematical range. The discrepancies of the results obtained with the PYTHIA and TWOGAM generators $|N(x_{unf}^{PYT}) - N(x_{unf}^{TWO})|/2$ are considered as systematic uncertainties related to the Monte Carlo modeling. This difference is due to the calculated acceptance as well as to the unfolding procedure. The uncertainty from the model dependence can vary by up to 7.1 % in the x bins. However, this uncertainty does not change significantly when we compare the three Q^2 intervals and the different data sets.

7.4. Extraction of F_2^γ

In order to obtain the photon structure function F_2^γ/α, the measured cross section $\Delta\sigma_{meas}$ is divided by an analytically calculated cross section (3.7), using the program GALUGA [68]

$$F_2^\gamma(x,Q^2)/\alpha = \frac{\Delta\sigma_{meas}(e^+e^- \to e^+e^-\text{hadrons})}{\Delta\sigma_{Galuga}(e^+e^- \to e^+e^-\text{hadrons})}. \qquad (7.16)$$

In general, GALUGA calculates the integrated cross section, using a parametrization similar to the equation

$$\Delta\sigma_{Galuga}(e^+e^- \to e^+e^-\text{hadrons}) = \int [L_{TT}F_T(Q^2)F_T(P^2)\sigma_{TT} + L_{LT}F_L(Q^2)F_T(P^2)\sigma_{LT}$$

$$+ L_{TL}F_T(Q^2)F_L(P^2)\sigma_{TL} + L_{LL}F_L(Q^2)F_L(P^2)\sigma_{LL}]\, dQ_1^2\, dQ_2^2\, dW, \qquad (7.17)$$

where L_{TT}, L_{LT}, L_{TL}, L_{LL} are the luminosity functions defined as the products of the photon fluxes for transverse (T) or longitudinal (L) photons. F_T and F_L are the form factors that depend only on Q^2 and P^2. In the single-tag case ($P^2 \cong 0$), equation (7.17) reduces to (3.14). Therefore, $\Delta\sigma_{Galuga}$ is the product of the target photon flux

and the cross section of equation (4.18), as given in (3.16). The program calculates the theoretical value $\Delta\sigma_{\text{Galuga}}$ in the given Q^2 and x range, setting $F_2^\gamma = 1$ and F_L^γ to the QPM value [27]. If setting $F_2^\gamma = 1$, the GALUGA output can be used as a reference for the extraction of the measured F_2^γ. In practice the F_L^γ contribution to the cross section is smaller than 1% due to the small value of y (Section 4.3). The running of the fine-structure constant with Q^2 is included. A GVDM form factor (4.35) is used in the calculation for the target photon virtuality whose average value is of the order of 0.07 GeV^2. The low polar-angle calorimeter acceptance for the tagged and the anti-tagged electron and the $W_{\gamma\gamma} > 4$ GeV requirement are taken into account. The uncertainty on $\Delta\sigma_{\text{Galuga}}$, as estimated by comparing the GVDM to a ρ form factor, is 2%.

The contribution of radiative corrections to the cross section is evaluated by using the program RADCOR [69],[70] that includes initial and final state radiation for the reaction $e^+e^- \rightarrow e^+e^-\mu^+\mu^-$.The corrections are mainly due to initial state radiation from the electron scattered at large angle. Final state radiation is detected together with the scattered electron due to the finite granularity of the calorimeter. Initial state radiation from the electron producing the quasi-real target photon is very small. The calculations are performed at the generator level using the Q^2 from the electron variables and $W_{\gamma\gamma}$ from the muon pair. The measured F_2^γ/α is multiplied by the ratio, R, of the non-radiative and the total cross section, shown in

Table 7.4 and Table 7.5 for different values of x and Q^2. The first uncertainty is statistic, the second systematic and the third is due to model dependence. The F_2^γ values are first obtained for each individual $\sqrt{s}$ data set. The results are statistically compatible and, consequently, a weighted average of F_2^γ is calculated for the Q^2 ranges with average values 12.4 GeV^2, 16.7 GeV^2 and 25.5 GeV^2. This procedure is applied to data unfolded separately with PYTHIA and TWOGAM and the two different values are shown in Figure 7.2. Only the statistical uncertainties are shown, which are often of the size of the symbols. For clarity, the symbols corresponding to the two Monte Carlo generators are slightly offset.

Their average value as a function of x for the three Q^2 intervals, with statistical and systematic uncertainties is given in Table 7.4 and in Figure 7.3. The former are indicated by the inner error bars. The final new data are presented together with the previous L3 results at $\sqrt{s}$ = 183 GeV [21], [22], [23]. The predictions of the high-order parton density functions GRV-set1 (i.e. GRV-HO, Section 4.4.4) and CJK are shown. The change in slope of the CJK prediction is due to c-quark threshold. The QPM prediction for $\gamma\gamma \to q\bar{q}$ is also shown.

x range	$\langle x \rangle$	$\mathcal{R}$	F_2^γ/α
$Q^2 = 11 - 14$ GeV^2			
$0.006 - 0.023$	0.013	0.92	0.302 ±0.013 ±0.026 ± 0.029
$0.023 - 0.040$	0.031	0.90	0.245 ±0.011 ±0.021 ± 0.010
$0.040 - 0.060$	0.050	0.88	0.257 ±0.011 ±0.023 ± 0.012
$0.060 - 0.090$	0.075	0.90	0.296 ±0.012 ±0.028 ± 0.009
$0.090 - 0.120$	0.10	0.89	0.315 ±0.013 ±0.032 ± 0.007
$0.120 - 0.160$	0.14	0.90	0.365 ±0.015 ±0.038 ± 0.008
$0.160 - 0.205$	0.18	0.88	0.399 ±0.017 ±0.043 ± 0.007
$0.205 - 0.260$	0.23	0.89	0.441 ±0.018 ±0.049 ± 0.011
$0.260 - 0.330$	0.29	0.88	0.483 ±0.020 ±0.054 ± 0.013
$0.330 - 0.400$	0.36	0.89	0.536 ±0.023 ±0.059 ± 0.025
$Q^2 = 14 - 20$ GeV^2			
$0.006 - 0.023$	0.013	0.93	0.310 ±0.014 ±0.020 ± 0.028
$0.023 - 0.040$	0.031	0.88	0.258 ±0.012 ±0.014 ± 0.018
$0.040 - 0.060$	0.050	0.90	0.275 ±0.012 ±0.014 ± 0.017
$0.060 - 0.090$	0.075	0.90	0.288 ±0.011 ±0.014 ± 0.008
$0.090 - 0.120$	0.10	0.89	0.316 ±0.013 ±0.015 ± 0.014
$0.120 - 0.160$	0.14	0.90	0.337 ±0.013 ±0.016 ± 0.007
$0.160 - 0.205$	0.18	0.89	0.381 ±0.015 ±0.018 ± 0.006
$0.205 - 0.260$	0.23	0.88	0.424 ±0.017 ±0.019 ± 0.008
$0.260 - 0.330$	0.29	0.88	0.471 ±0.018 ±0.020 ± 0.009
$0.330 - 0.400$	0.36	0.87	0.510 ±0.021 ±0.022 ± 0.007
$0.400 - 0.467$	0.42	0.88	0.551 ±0.024 ±0.024 ± 0.026
$Q^2 = 20 - 34$ GeV^2			
$0.023 - 0.040$	0.031	0.89	0.317 ±0.017 ± 0.016 ±0.017
$0.040 - 0.060$	0.050	0.89	0.293 ±0.015 ± 0.014 ±0.010
$0.060 - 0.090$	0.075	0.89	0.314 ±0.013 ± 0.015 ±0.012
$0.090 - 0.120$	0.10	0.88	0.338 ±0.016 ± 0.016 ±0.018
$0.120 - 0.160$	0.14	0.88	0.384 ±0.017 ± 0.018 ±0.017
$0.160 - 0.205$	0.18	0.88	0.404 ±0.017 ± 0.018 ±0.004
$0.205 - 0.260$	0.23	0.88	0.446 ±0.018 ± 0.020 ±0.009
$0.260 - 0.330$	0.29	0.87	0.488 ±0.019 ± 0.022 ±0.006
$0.330 - 0.400$	0.36	0.87	0.557 ±0.023 ± 0.025 ±0.010
$0.400 - 0.467$	0.42	0.87	0.611 ±0.027 ± 0.029 ±0.015
$0.467 - 0.556$	0.49	0.87	0.683 ±0.028 ± 0.030 ±0.062

Table 7.4 Measured values of F_2^γ/α and the applied radiative correction factors, R, in bins of x for the three Q^2 ranges.

Q^2 range	$\langle Q^2 \rangle$	$\mathcal{R}$	F_2^γ/α
$x = 0.01 - 0.1$			
$11 - 14$	12.4	0.89	$0.278 \pm 0.006 \pm 0.028 \pm 0.013$
$14 - 20$	16.7	0.89	$0.287 \pm 0.006 \pm 0.015 \pm 0.015$
$20 - 34$	25.5	0.88	$0.316 \pm 0.008 \pm 0.016 \pm 0.013$
$x = 0.1 - 0.2$			
$11 - 14$	12.4	0.88	$0.377 \pm 0.010 \pm 0.039 \pm 0.008$
$14 - 20$	16.7	0.88	$0.355 \pm 0.009 \pm 0.017 \pm 0.005$
$20 - 34$	25.5	0.88	$0.399 \pm 0.011 \pm 0.019 \pm 0.010$
$x = 0.2 - 0.3$			
$11 - 14$	12.4	0.88	$0.464 \pm 0.015 \pm 0.051 \pm 0.009$
$14 - 20$	16.7	0.88	$0.442 \pm 0.013 \pm 0.020 \pm 0.003$
$20 - 34$	25.5	0.87	$0.477 \pm 0.015 \pm 0.023 \pm 0.013$
$x = 0.3 - 0.5$			
11-14	12.4	0.89	$0.544 \pm 0.017 \pm 0.061 \pm 0.019$
14-20	16.7	0.87	$0.545 \pm 0.014 \pm 0.024 \pm 0.012$
20-34	25.5	0.87	$0.594 \pm 0.015 \pm 0.029 \pm 0.022$

Table 7.5 The values of F_2^γ/α in bins of Q^2 for four x ranges together with the radiative correction factor.

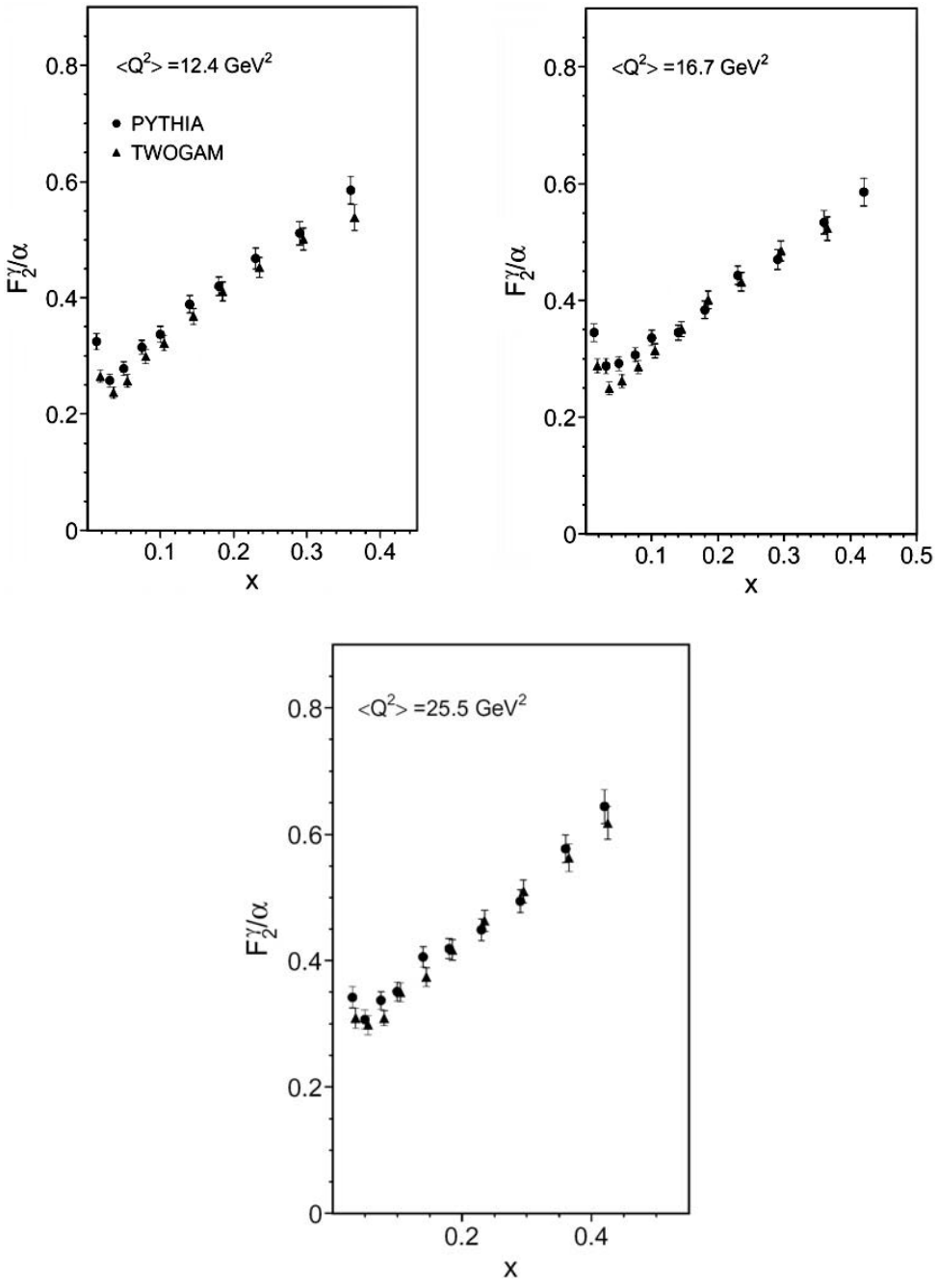

Figure 7.2 The photon structure function F_2^γ/α as a function of x for the three Q^2 ranges obtained with PYTHIA and TWOGAM.

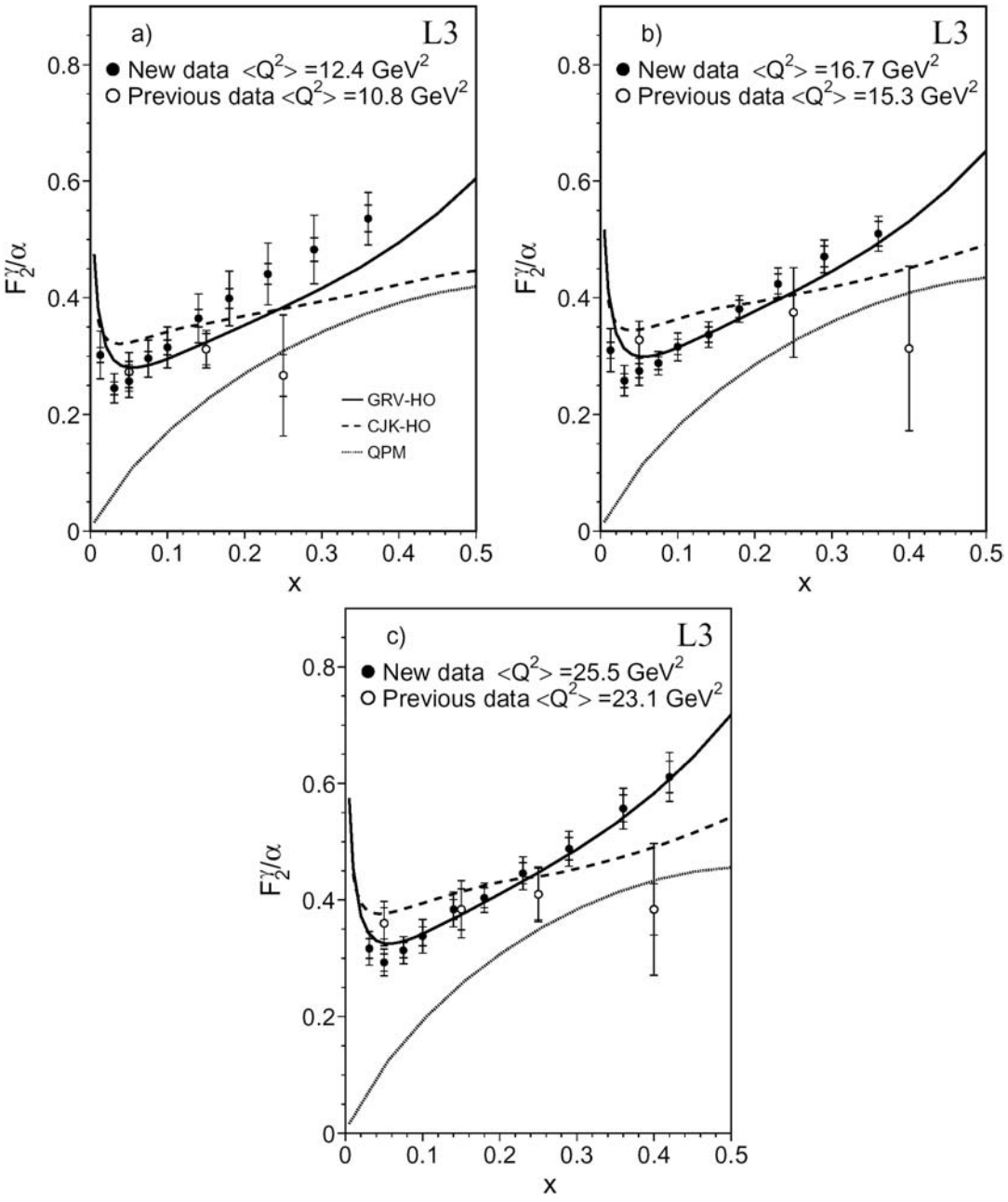

Figure 7.3 The photon structure function F_2^γ/α as a function of x for the three Q^2 intervals.

In addition to the systematic uncertainty on the cross section, presented in Table 7.3, two systematic uncertainties are further considered in the extraction of F_2^γ : a 2% uncertainty on the GALUGA calculation and a 2% uncertainty on the estimation of the radiative corrections. The latter is estimated by varying the cone angle of the calorimeter for which final state radiation is detected together with the scattered electron.

A comparison of the data with the existing parametrizations (Section 4.4.3) as obtained with the PDFLIB library [71] shows that our data are not well described by the leading-order parton density functions. In Figure 7.3 the data are compared with the predictions of the high-order parton density functions GRV-set1 [72], [73], which shows the best agreement with the data, and the more recent CJK set [18] whose agreement is poorer. In both cases four quarks, u, d, s and c are used. The pure QPM prediction for $\gamma\gamma \to q\bar{q}$ is also indicated. It is calculated by using GALUGA with a mass of 0.32 GeV for the u and d quarks, 0.5 GeV for the s quark, and 1.4 GeV for the c quark. It is clearly insufficient to describe the data.

F_2^γ has been calculated for the Q^2 range $11\,\mathrm{GeV}^2 \le Q^2 \le 34\,\mathrm{GeV}^2$ with the average value $\langle Q^2 \rangle = 18.4\ \mathrm{GeV}^2$ taking the weighted average for F_2^γ in the three Q^2 intervals (Figure 7.4). Figure 7.4 shows the comparison to GRV-set1 prediction for u, d, s and u, d, s, c quarks separately. For low x values, below $x \sim 0.05$, L3 data is best described by GRV-set1 with contributions only from the u, d, s light quarks. For higher values of x, above $x \sim 0.05$, the good fit with GRV-set1 calculated for u,

d, s, and c quarks shows that the charm quark contribution is getting significant in the given Q^2 range. A recent review on the charm contribution to F_2^γ predicted by GRV parametrizations can be found in [74]. Figure 7.4 also compares the new L3 results to measurements from the other LEP experiments: ALEPH [20], DELPHI [75] and, OPAL [76]. The comparison has its limits, because each experiment uses different methods. They compare their data to the expectations of a Monte Carlo generated with a well defined parton density function, while in the present analysis L3 deconvolutes the target photon flux and the kinematic factors of Equation (4.18) by using the analytical program GALUGA. It has to be also noted, that from the four LEP experiments only OPAL and L3 include radiative corrections in their calculations.

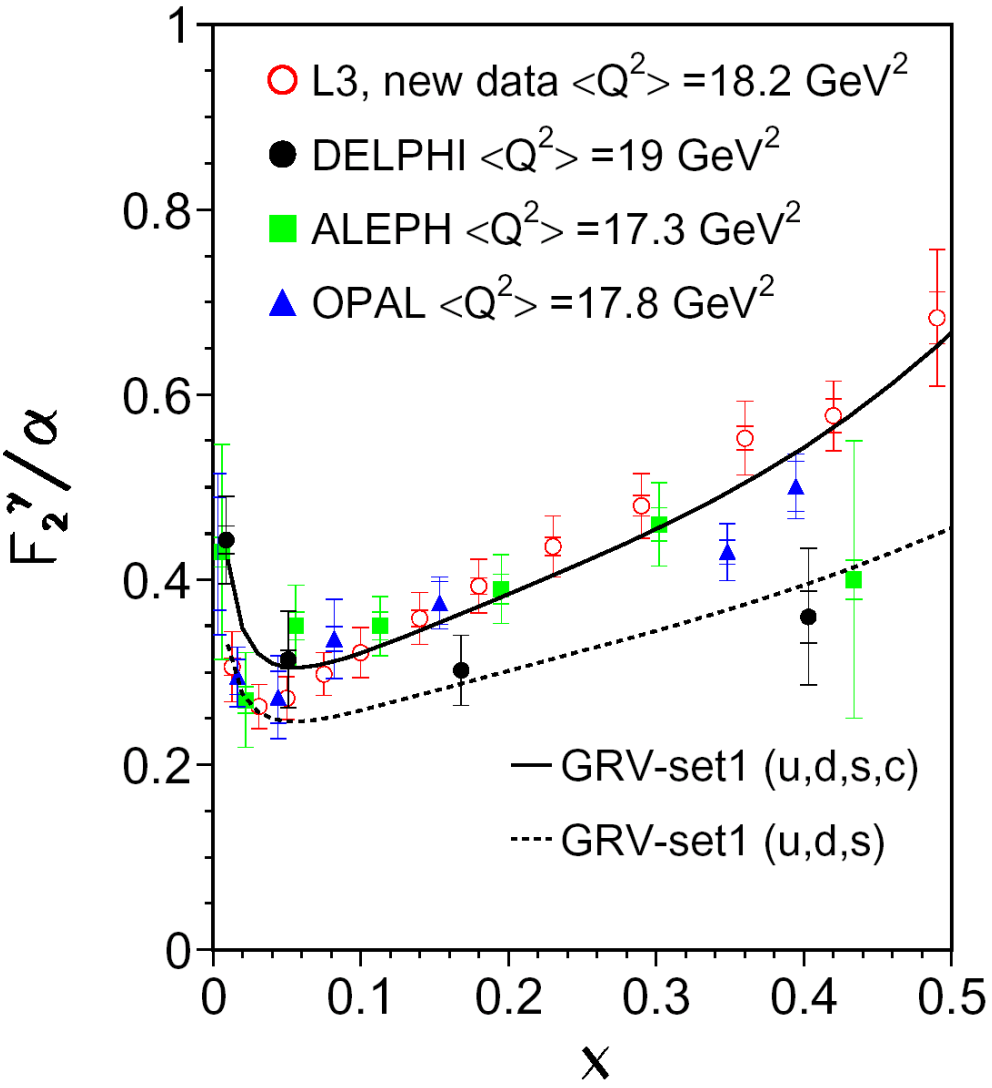

Figure 7.4 The photon structure function F_2^γ/α as a function of x for $< Q^2 >= 18.4\,\mathrm{GeV}^2$ compared to predictions from GRV-set1 and measurements from other LEP experiments.

Q^2-evolution of the photon structure function

The Q^2-evolution of F_2^γ, is studied in four x bins, $0.01 \le x \le 0.1$, $0.1 \le x \le 0.2$, $0.2 \le x \le 0.3$, $0.3 \le x \le 0.5$ and the results are given in Table 7.5. In Figure 7.5 the F_2^γ/α values are presented for the lowest x bin and for a combined bin $0.1 \le x \le 0.5$, together with previous L3 results [21], [22], and [23]. Corrections for radiative effects are applied. The new measurements at $11\,\mathrm{GeV}^2 \le Q^2 \le 14\,\mathrm{GeV}^2$, $14\,\mathrm{GeV}^2 \le Q^2 \le 20\,\mathrm{GeV}^2$, and $20\,\mathrm{GeV}^2 \le Q^2 \le 34\,\mathrm{GeV}^2$ are in good agreement with our previous L3 results. The expected linear growth with $\ln Q^2$ is observed in both x intervals. The function $a + b \cdot \ln Q^2\,(\mathrm{GeV}^2)$ is fitted to the data, taking into account the total uncertainty calculated from the quadratic sum of statistical and systematic uncertainties. The fit results are: a = 0.141 ± 0.007 and b = 0.060 ± 0.005 for $0.01 \le x \le 0.1$ with a confidence level of 44% and a = 0.05 ± 0.11 and b = 0.13 ± 0.04 for $0.1 \le x \le 0.5$ with a confidence level of 71%. The predictions of the high-order parton density functions GRV-set1 and CJK [18] are also indicated in Figure 7.5. The evolution is different for the two models; the data are better described by the GRV-set1 model.

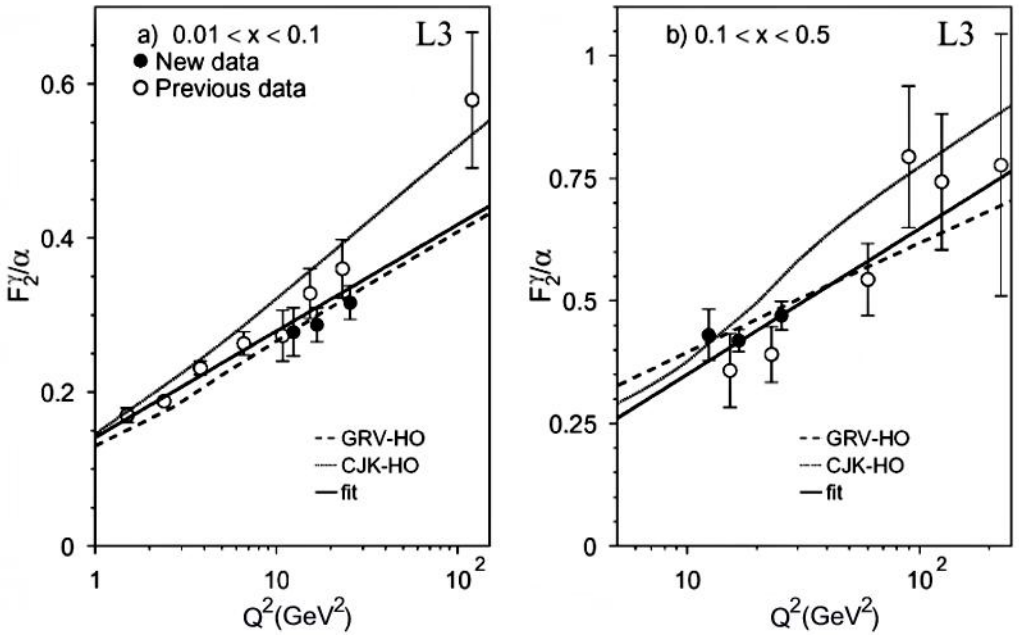

Figure 7.5 Evolution of the photon structure function F_2^γ/α as a function of Q^2 for two x intervals.

Chapter 8

8. SUMMARY AND CONCLUSIONS

The photon can have two different appearances. It can behave as a point-like particle or it can fluctuate into a fermion anti-fermion pair. This quantum mechanical behavior can be studied at advanced particle accelerators. With the LEP accelerator we were able to reach energies and luminosities high enough to be able to study the deep inelastic $e^+e^- \rightarrow \gamma^*\gamma^{(*)} \rightarrow e^+e^-$ hadrons reaction in order to measure the structure of the photon with an increased precision.

Results have been obtained by studying the collision between a virtual and a real photon. The event could be reconstructed based on the information from one scattered electron detected in the low polar angle luminosity monitor of the L3 detector, and the final state hadrons. Due to the boost of the gamma-gamma system these particles were preferentially produced in the forward and backward regions where the detectors could only partially cover the space around the beam pipe, leaving acceptance holes. Since we had only partial information to reconstruct the described event, the observed x_{vis} distribution is distorted compared to the true x (x_{true}) distribution. In order to obtain x_{true} from the measured x_{vis} distribution, an unfolding procedure was used, based on Bayes' Theorem. The measured cross

section was calculated using the unfolded distributions and taking into account efficiencies of the trigger, detection, and selection. To obtain the photon structure function F_2^γ/α, the measured cross section $\Delta\sigma_{meas}$ was divided by an analytically calculated cross section using the program GALUGA. Finally, results were compared with theoretical predictions, previous L3 results, and results from the other LEP experiments.

The photon structure function F_2^γ was measured at LEP with the L3 detector at center-of-mass energies $189 \le \sqrt{s} \le 209$ GeV in the Q^2 range $11\,\mathrm{GeV}^2 \le Q^2 \le 34\,\mathrm{GeV}^2$ and the x range $0.006 \le x \le 0.556$. The data were better described by the high-order parton density function of GRV-set1 than by other parton distribution functions determined from the low energy data. For the present Q^2 range GRV-set1 takes into account the presence of the 3 light quarks u, d, s and the heavy charm quark in the quasi-real target photon.

Together with previous measurements, the L3 collaboration has studied the Q^2 evolution from 1.5 GeV^2 to 120 GeV^2 in the low-x region, $0.01 \le x \le 0.1$, and from 12.4 GeV^2 to 225 GeV^2 in the higher-x region, $0.1 \le x \le 0.5$. The measurements at different center-of-mass energies were consistent and the $\ln Q^2$ evolution of F_2^γ was clearly confirmed.

What makes these measurements unique and significant?

L3 has excellent resolution for photons and charged hadrons. Therefore, it is an excellent detector for two photon physics studies.

L3 measurements of the hadronic photon structure function F_2^γ in the Q^2 ranges $1.2\,\mathrm{GeV}^2 \le Q^2 \le 30\,\mathrm{GeV}^2$ and $9\,\mathrm{GeV}^2 \le Q^2 \le 30\,\mathrm{GeV}^2$, at centre-of-mass energies 91 GeV(LEP1) and 183 GeV(LEP2) with integrated luminosities of 140 pb^{-1} and 51.9 pb^{-1}, respectively, have been previously performed [21], [22].

However, these investigations were deficient mainly in the lower x regions due to the limited statistics at the energies descried above. In this measurement an integrated luminosity of 608 pb^{-1} was achieved for LEP2 center-of-mass energies between $189\,\mathrm{GeV} < \sqrt{s} < 209\,\mathrm{GeV}$. A rich sample of two-photon events has been obtained and used for this work to measure the cross section and hadronic structure function F_2^γ in the kinematical range defined by the LUMI tagging detector of L3. The physics advantage of the high energy reached at LEP2 comes from the increased center-of-mass energy between the virtual photon probe and the real photon target. Because of this we were able to measure the hadronic photon structure function at lower x values than was done before. Consequently, the results from this dissertation represent a higher precision measurement of the structure function F_2^γ in the x and Q^2 ranges between 0.006-0.556 and

$11\,\mathrm{GeV}^2 \le Q^2 \le 34\,\mathrm{GeV}^2$ respectively. Figure 7.4 shows the improvement due to our new measurement compared to previous data from ALEPH, DELPHI and OPAL. The data are best described by the higher-order parton density function of GRV-set1 (GRV-HO). Due to the high energy obtained with the LEP accelerator, it was possible to measure the effect of the heavier charm quark in addition to the 3 light quarks.

Future work

The results obtained in this dissertation bring up interesting and important questions that should be the subject of future studies:

a) Results from Section (7.4), Figure 7.4 suggest the existence of a charm threshold at low x values in the given Q^2 domain. The charm contribution can be studied through the measurement of the charm structure function [74]. It would be interesting to investigate the charm contribution to F_2^γ using the currently analyzed L3 data set.

b) The GRV [39] parametrization already suggests a value for the strong coupling constant $\alpha_s \cong 0.2$ for the present data. For a precise measurement of α_s one should perform a 5 parameter fit to the data as described in [78].

c) The kinematical range $11\,\mathrm{GeV}^2 \le Q^2 \le 34\,\mathrm{GeV}^2$ from the present analysis might be extended using other L3 tagging subdetectors into the range

$0.4\,\mathrm{GeV}^2 \le Q^2 \le 1.22\,\mathrm{GeV}^2$ (Very Small Angle Tagger - VSAT),

$30\,\mathrm{GeV}^2 \le Q^2 \le 115\,\mathrm{GeV}^2$ (Active Lead Ring -ALR) respectively

$3070\,\mathrm{GeV}^2 \le Q^2 \le 3850\,\mathrm{GeV}^2$ (BGO endcap).

References

[1] F. Halzen, and A. D. Martin, Quarks and Leptons "An Introductory Course in Modern Particle Physics," John Wiley & Sons, Inc., 1984.

[2] P. Achard et al. (L3 Collaboration), Determination of α_s from Hadronic Event Shapes in e^+e^- Annihilation at $192 \leq \sqrt{s} \leq 208$ GeV, Phys. Lett. B 536 (2002) 217.

[3] R.W. Asmann, LEP Operation and Performance with Electron-Positron Collisions at 209 GeV, Internet, http://www.capp.iit.edu/workshops/epem/References/lep2001f.pdf (2001).

[4] P.G. Abia, Search for Higgs Bosons and New Physics at LEP, Internet, http://l3.web.cern.ch/l3/conferences/ps/Garcia_LaThuile2003.pdf (2003).

[5] B. Adeva et al. (L3 Collaboration), The Construction of the L3 Experiment, Nucl. Instrum. Meth. A 289 (1990) 35.

[6] M. Acciarri et al. (L3 SMD Collaboration), The L3 Silicon Microvertex Detector, Nucl. Instrum. Meth. A 351 (1994) 300.

[7] M. Chemarin et al., Test Beam Results for an Upgraded Forward Tagger of the L3 experiment at LEP2, Nucl. Instrum. Meth. A 349 (1994) 345.

[8] A. Adam et al. (L3 F/B Muon Group), The Forward Muon Detector of the L3, Nucl. Instrum. Meth. A 383 (1996) 342.

[9] I.C. Brock et al., Luminosity Measurement in the L3 detector at LEP, Nucl. Instrum. Meth. A 381 (1996) 236.

[10] C. Dionisi et al., The Third Trigger System of the L3 Experiment at LEP, Nucl. Instrum. Meth. A 336 (1993) 78.

[11] C. Berger et al. (Pluto Collaboration), Measurement of the Total Photon-Photon Cross Section for the Production of Hadrons at small Q^2, Phys. Lett. B 149 (1984) 421.

[12] R. Nisius, The Photon Structure Function From Deep Inelastic Scattering, Phys. Rept. 332 (2000) 165.

[13] V.M. Budnev et al., The Two Photon Particle Production Mechanism. Physical Problems. Applications. Equivalent Photon Approximation., Phys. Rept. 15 (1974) 181.

[14] C. Berger and W. Wagner, Photon Photon reactions, Phys. Rept. 146 (1987) 1.

[15] P. Kessler, Sur Une Methode Simplifiee de Calcul Pour les Processus Relativists en Electrodynamique Quantique, Il Nuovo Cimento 17 (1960) 809.

[16] M. Krawczyk, A. Zembrzuski and M. Staszel, Survey of Present Data on Photon Structure Functions and Resolved Photon Processes, Phys. Rept. 345 (2001) 265.

[17] M. Klasen, Theory of Hard Photoproduction, Rev. Mod. Phys., 74 (2002) 1221.

[18] F. Cornet et al., A New Five Flavor LO Analysis and Parametrization of Parton Distributions in the Real Photon, Phys. Rev. D 68 (2003) 014010.

[19] R. Barate et al. (ALEPH Collaboration), Measurement of the Hadronic Photon Structure Function at LEP1 for Q^2 values between 9.9 GeV^2 and 284 GeV^2, Phys. Lett. B 458 (1999) 152.

[20] A. Heister et al. (ALEPH Collaboration), Measurement of the hadronic Photon Structure Function $F_2^{\gamma}(x,Q^2)$ in Two-Photon Collisions at LEP, Eur. Phys. J. C 30 (2003) 145.

[21] M. Acciarri et al. (L3 Collaboration), Study of the Hadronic Photon Structure Function F_2^{γ} at LEP, Phys. Lett. B 436 (1998) 403.

[22] M. Acciarri et al. (L3 Collaboration), The Q^2 Evolution of the Hadronic Photon Structure Function F_2^γ at LEP, Phys. Lett. B 447 (1999) 147.

[23] M. Acciarri et al. (L3 Collaboration), Measurement of the Photon Structure Function at High Q^2 at LEP, Phys. Lett. B 483 (2000) 373.

[24] G. Abbiendi et al. (OPAL Collaboration), Measurement of the Low x Behavior of the Photon Structure Function F_2^γ, Eur. Phys. J. C 18 (2000) 15.

[25] G. Abbiendi et al. (OPAL Collaboration), Measurement of the Hadronic Photon Structure Function F_2^γ at LEP2, Phys. Lett. B 533 (2002) 207.

[26] H. Kolanoski and P. Zerwas, Two-Photon Physics, DESY-87-175 (1987) 90. Published in: High Energy Electron-Positron Physics, World Scientific, 1988.

[27] T.F. Walsh and P. Zerwas, Two Photon Processes in the Parton Model, Phys. Lett. B 44 (1973) 195.

[28] R.L. Kingsley, Anomalies in Photon-Photon Scattering Reactions, Nucl. Phys. B 60 (1973) 45.

[29] T.H. Bauer, R.D. Spital, D.R. Yennie and F.M. Pipkin, The Hadronic Properties of the Photon in High Energy Interactions, Rev. Mod. Phys. 50 (1978) 261.

[30] J. Sakurai and D. Schildknecht, Generalized Vector Dominance and Inelastic Electron Proton Scattering, Phys. Lett. B 40 (1972) 121.

[31] H. Kolanoski, *Two-Photon Physics at e^+e^- Storage Rings,* Springer-Verlag Berlin Heidelberg, 1984.

[32] J. L. Rosner, Brookhaven Report CRISP 71 (1971) 26.

[33] M. Drees and K. Grassie, Parametrizations of the Photon Structure and Applications to Supersymmetric Particle Production at HERA, Z. Phys. C 28 (1985) 451.

[34] V.N. Gribov and L.N. Lipatov, e^+e^- Pair Annihilation and Deep Inelastic ep Scattering in Perturbation Theory, Nucl. Phys. 15, (1972) 675, and Yad. Fiz. 15, (1972) 1218.

[35] G. Altarelli and G. Parisi, Asymptotic Freedom in Parton Language, Nucl. Phys. B126, (1977) 298.

[36] Y.L. Dokshitzer, Calculation of the Structure Functions for Deep Inelastic Scattering and e^+e^- Annihilation by Perturbation Theory in Quatum Chromodynamics (in Russian) Sov. Phys. JETP 46, (1977) 641.

[37] H. Abramowicz, K. Charchula, and A. Levy, Parametrization of Parton Distributions in the Photon, Phys. Lett. B 269 (1991) 458.

[38] K. Hagiwara, M. Tanaka, and I. Watanabe, Gluon and Charm Distributions in the Photon, Phys. Rev. D 51 (1995) 3197.

[39] M. Glück, E. Reya, and A. Vogt, Photonic Parton Distributions, Phys. Rev. D 46, (1992) 1973.

[40] P. Aurenche, J.-P. Guillet, and M. Fontannaz, Parton Distributions in the Photon, Z. Phys. C 64 (1994) 621.

[41] L.E. Gordon and J.K. Storrow, New Parton Distribution Functions for the Photon, Nucl. Phys. B 489 (1997) 405.

[42] M. Glück, E. Reya, and I. Schienbein, Radiatively Generated Parton Distributions for Real and Virtual photons, Phys. Rev. D 60, (1999) 054019.

[43] G.A. Schuler and T. Sjostrand, Low- and High-Mass Components of the Photon Distribution Function, Z. Phys. C 68 (1995) 607.

[44] M. Glück, E. Reya, and A. Vogt, Pionic Parton Distributions, Z. Phys. C 53 (1992) 651.

[45] T. Sasaki et al., A Measurement of the Photon Structure Function F_2^γ, Phys. Lett. B 252 (1990) 491.

[46] W. Bartel et al., Experimental Study of the Photon Structure Function F_2^γ at Q^2 from 10 GeV^2 to 220 GeV^2, Z Phys C 24 (1984) 231.

[47] C. Berger et al. (PLUTO Collaboration), A measurement of the Q^2 and W dependence of the $\gamma\gamma$ total cross section for hadron production, Z. Phys. C 26, (1984) 353.

[48] C. Berger et al. (PLUTO Collaboration), Measurement of the photon structure function $F_2^\gamma(x, Q^2)$, Phys. Lett. B 142 (1984) 111.

[49] C. Berger et al. (PLUTO Collaboration), Measurement and QCD analysis of the photon structure function $F_2^\gamma(x, Q^2)$, Nucl. Phys. B 281 (1987) 365.

[50] M. Althoff et al. (TASSO Collaboration), Measurement of the photon structure function F_2^γ at Q^2 from 7 to 70 $(GeV/c)^2$, Z. Phys. C 31 (1986) 527.

[51] H. Aihara et al. (TPC/2γ Collaboration), Measurement of the photon structure function $F_2^{\gamma}(x, Q^2)$ in the region $0.2 < Q^2 < 7\,\mathrm{GeV}^2$, Z. Phys. C 34, (1987) 1.

[52] D. Bintinger et al. (TPC/2γ Collaboration), Measurement of the total hadronic cross section in virtual photon-photon interactions, Phys. Rev. Lett. 54 (1985) 763.

[53] H. Aihara et al. (TPC/2γ Collaboration), Observation of scaling of the photon structure function F_2^{γ} at low Q^2, Phys. Rev. Lett. 58 (1987) 97.

[54] ALEPH, L3 and OPAL Coll., Comparison of Deep Inelastic Electron Photon Scattering Data with the Herwig and Phojet Monte Carlo Models, Eur. Phys. J. 23 (2002) 201.

[55] PHOJET version 1.05c is used: R. Engel, Photoproduction within the Two Component Dual Parton Model Z. Phys. C 66 (1995) 203.

[56] R. Engel and J. Ranft, Comparative Study of the Hadronic Production of B(C) Mesons, Phys. Rev. D 54 (1996) 4344.

[57] PYTHIA version 6.203 is used: T. Sjostrand et al., High Energy Physics Event Generation with Pythia 6.1., Comp. Phys. Comm. 135 (2001) 238.

[58] TWOGAM version 1.71 is used: S. Nova, A. Olshevski, T. Todorov, DELPHI Note 90-35 (1990).

[59] DIAG36 Monte Carlo is used: F.A. Berends, P.H. Daverveldt and R. Kleiss, Complete lowest Order Calculations for Four Lepton Final States in Electron-Positron Collisions, Nucl. Phys. B 253 (1985) 441.

[60] F.A. Berends, P.H. Daverveldt and R. Kleiss, Monte Carlo Simulation of Two Photon Processes, "II: Complete lowest order calculations for four-lepton production processes in electron-positron collisions," Comp. Phys. Comm. 40 (1986) 285.

[61] GEANT version 3.15 is used: R. Brun et al., GEANT3, preprint CERN-DD/EE/84-1 (1984), revised 1987.

[62] H. Fesefeldt, GHEISHA, RWTH Aachen report PITHA 85/2 (1985).

[63] A. Capella et al., Dual Parton Model, Phys. Rept. 236 (1994) 225.

[64] JETSET version 7.4 is used: T. Sjostrand, High Energy Physics Event Generation with Pythia 5.7 and Jetset 7.4, Comp. Phys. Comm. 82 (1994) 74.

[65] G. D'Agostini, A Multidimensional Method Based on Bayes' Theorem, Nucl. Instr. Meth. A 362 (1995) 487.

[66] A. Höcker and V. Karvelishvili, SVD Approach to Data Unfolding, Nucl. Instr. Meth. A 372 (1996) 469.

[67] L. L. Van Rossum, Hadron Production in Two-Photon Collisions at LEP, Dissertation Thesis, University Utrecht, (1998).

[68] GALUGA version 2.0 is used: G.A. Schuler, Two Photon Physics with GALUGA 2.0, Comp. Phys. Comm. 108 (1998) 279.

[69] RADCOR Monte Carlo is used: F.A. Berends, P.H. Daverveldt and R. Kleiss, Radiative Corrections to the process $e^+e^- \to e^+e^-\mu^+\mu^-$, Nucl. Phys. B 253 (1985) 421.

[70] F.A. Berends, P.H. Daverveldt, and R. Kleiss, Monte Carlo Silulation of the Two-Photon Processes. "1. Radiative Corrections to Mutipherial $e^+e^- \to e^+e^-\mu^+\mu^-$ production.," Comp. Phys. Comm. 40 (1986) 271.

[71] H. Plothow-Besch, PDFLIB: A Library of all Available Parton density Functions of the Nucleon, the Pion and the Photon and the Corresponding α_s calculations, Comp. Phys. Comm. 75 (1993) 396.

[72] M. Glück, E. Reya, and A. Vogt, Parton Structure of the Photon Beyond Parton Structure of the Photon Beyond the Leading Order, Phys. Rev. D 45 (1992) 3986.

[73] M. Glück, E. Reya and A. Vogt, Photonic Parton Distributions, Phys. Rev. D 46 (1992) 1973. The values given in appendix A2 (pg. 1977) are used.

[74] R. Nisius, (OPAL Collaboration), First Measurement of the Photon Structure Function $F_{2,c}^{\gamma}$, Invited talk given at the PHOTON 2000 Conference, Ambleside, UK, August 26-31, 2000; hep-ex 0010020.

[75] DELPHI Collaboration, Study of Hadronic Photon Structure Function at LEP2, 2003-025 CONF 645 (2003).

[76] G. Abbiendi et al. (OPAL Collaboration), Measurement of the Low-x Behavior of the Photon Structure Function F_2^{γ} Eur. Phys. J. C 18 (2000) 15.

Works Consulted

[77] I.J. Aitchison and A.J. Hey, *Gauge Theories in Particle Physics*, IOP Publishing Ltd, 1989.

[78] S. Albino, Michael Klasen, and S. Rembold, Strong Coupling Constant from the Photon Structure Function, DESY 02-052, FERMILAB-Pub-02/-71-E (2002); hep-ph/0205069.

[79] R.K. Bock et al., *Data Analysis Techniques for High Energy Physics,* Cambridge University Press, 2000.

[80] V.M. Budnev et al., The Two-Photon Particle Production Mechanism. Physical Problems. Applications. Equivalent Photon Approximation., Phys. Rept. 15 (1975) 181.

[81] Susan Cartwright et al., Two photon physics at LEP2, RAL-97-042, (1997); hep-ph/9708478.

[82] H. Frauenfelder and E.M. Henley, *Subatomic Physics,* Prentice-Hall, Inc.

[83] G. Kane, Modern Elementary Particle Physics "The Fundamental Particles and Forces," Addison-Wesley Publishing Company, 1993.

[84] H. Kolanoski, *Two-Photon Physics at e^+e^- Storage Rings,* Springer-Verlag Berlin Heidelberg, 1984.

[85] The L3 Adminstration and Communication Group, The L3 experiment "Progress in Physics, Technology and International Collaboration", 1998.

[86] D. Griffiths, *Introduction to Elementary Particles*, John Wiley & Sons, Inc., 1987.

[87] Photon 99, Proceedings of the International Conference on the Structure and Interactions of the Photon, including the 12th International Workshop on Photon-Photon Collisions, editor S. Rembold, Freiburg, Germany, May 23-27, 1999; Nucl. Phys. B (Proc. Suppl.) 82 (2000).

[88] R. A. Serway, Clement J. Moses, and Curt A. Moyer, *Modern Physics,* Harcourt College Publishers, 1989.

[89] R. A. Serway, *Physics For Scientists and Engineers*, Saunders Golden Sunburst Series, 1996.

Appendix

Units of Measurement

A brief overview of the units used in particle physics, relevant for this dissertation is introduced here. Planck's constant ($\hbar = h/2\pi = 1.055 \times 10^{-34}$ [J sec]) and the velocity of light ($c = 2.998 \times 10^{8}$ [m/sec]) are well known quantities from relativistic quantum mechanics. The velocity of light can be defined as 1 unit of velocity=L/T, and Planck's constant measured in [J sec] is 1 unit of action=ML^2/T. If we choose c and $\hbar$ to be equal to 1 this simplifies the writing of lengthy formulas. We can always introduce these values back into the final result using dimensional analysis. As an example, instead of equation $E^2 = p^2c^2 + m^2c^4$, one can write $E^2 = p^2 + m^2$. Here E is energy, p is momentum, and m is mass. The mass (m), momentum (mc), and energy are expressed in terms of GeV, while the length ($\hbar/mc$) and time($\hbar/mc^2$) are in units of GeV^{-1}. The unit for the cross section σ is usually expressed in mb (millibarns), nb (nanobarns) or pb (picobarns). The luminosity has the general expression R/σ [$cm^{-2}\, s^{-1}$], where R is the reaction rate. Its unit is usually expressed in pb^{-1}.